POLITECNICO DI TORINO

MASTER's degree in ENERGY AND NUCLEAR ENGINEERING

Renewable energy systems

Politecnico di Torino

Master's Degree Thesis

Experimental study of a chemical looping process using SFNM-04 perovskite to dissociate carbon dioxide

SUPERVISORS

Prof. MASSIMO SANTARELLI

Dr. DOMENICO FERRERO

Dr. SALVATORE CANNONE

Dr. FRANCESCO ORSINI

CANDIDATE

MATTEO FRANCESCHI

March 2022

Abstract

Earth's global average temperature has been rising since the industrial period, and the anthropogenic emissions of greenhouse gases, carbon dioxide especially, have been widely recognized as the main cause. The energy sector is a major contributor of emissions, as fossil fuels are still the most utilized primary energy source. As the energy demand is expected to grow in the near future, new pathways to produce energy are needed. Direct use of renewable energy sources, like solar and wind power, is a possibility. However, their intermittence and difficulty of storage make a rapid substitution of fossil fuels arduous. A hybrid path to fulfill a fraction of the energy demand using renewable energy as the primary source, but without removing fuels and devices that require them, is the use of solar fuels. A solar fuel is like fossil fuels in terms of properties, but it is produced from solar energy and zero-energy molecules such as carbon dioxide and water, instead of being extracted from underground deposits. Thus, carbon dioxide is valorized instead of being emitted into the atmosphere. If carbon capture processes are added to a plant that uses solar fuels, the recovered carbon dioxide can be the raw material to produce new fuel, closing a cycle with little or no emissions.

The intermediate product between carbon dioxide and a fuel is syngas, a mixture of hydrogen and carbon monoxide. Among the several different processes to produce syngas using renewable energy, the two-step chemical looping cycle is one of the most promising. Chemical looping consists in using thermal energy, for example coming from a system of solar concentrators, to split carbon dioxide into carbon monoxide and oxygen, or water into hydrogen and oxygen. If the process is divided into two steps, the oxygen is absorbed by an oxygen carrier material during the first step, and later the carrier is regenerated with thermal energy, making it release the oxygen previously assimilated. The oxygen carrier material thus facilitates the splitting process. In this work, a perovskite metal oxide with formula $Sr_2FeNi_{0.4}Mo_{0.6}O_6$ (SFNM-04 or SFNM for short) is investigated as a new possible high-performance oxygen carrier. The material was synthetized by University of Udine (UNIUD), and it is being currently studied in a collaboration project that involves University of Udine (UNIUD), the Massachusetts Institute of Technology (MIT), and Politecnico di Torino. Several experimental tests were carried out with SFNM-04 in the CO_2 Circle Lab at Environmental Park (Turin). In the experiments,

the material was positioned inside a reactor at temperatures up to 850°C and exposed to a carbon dioxide stream in order to study the production of carbon monoxide. The tests highlighted a carbon monoxide specific yield for SFNM-04 that increases with increasing temperatures, decreasing gas flow rates and decreasing sample masses. In general, the specific yield resulted in thousands or tens of thousands of μmol/g. The material was also tested in two different reactor configurations, one with the SFNM powder laid on an alumina crucible, and the other one with the SFNM dispersed inside a quartz wool matrix placed in a tube-in-tube setup. The tube-in-tube proved to be the better configuration in terms of yield. This thesis also presents a simplified model of the reactor implemented in the Aspen Plus® software, with several assumptions made to model the new material and a specific point of operation. The results of one of the tests in the reactor are used as input parameters for the numerical simulations, in order to estimate the thermal and solar efficiencies of a process using SFNM as oxygen carrier to produce syngas. As the tests carried out with the reactor only studied the production of carbon monoxide, the hydrogen in this preliminary model is supposed to come from a different process driven by renewable sources. Therefore, more tests will be needed in the future, in order to analyze the possibility of producing hydrogen from SFNM together with CO. In this way, a proper solar fuel could be produced, with the aim of finding new ways to decarbonize the energy sector and help mitigating the causes of climate change.

Table of contents

List of figures

List of tables

Acronyms

GHG	Greenhouse Gas
IPCC	Intergovernmental Panel on Climate Change
CCS	Carbon Capture and Storage
PV	Photovoltaic
PEC	Photoelectrochemical cell
CSP	Concentrated Solar Power
WS	Water Splitting
CDS	Carbon Dioxide Splitting
NG	Natural Gas
SNG	Synthetic Natural Gas
DME	Dimethyl ether
FT	Fischer-Tropsch
LNG	Liquified Natural Gas
WGS	Water Gas Shift
LT-FT	Low Temperature Fischer-Tropsch
HT-FT	High Temperature Fischer-Tropsch
bpd	barrels per day
GtL	Gas to Liquid
BtL	Biomass to Liquid
CHP	Combined Heat and Power
OC	Oxygen Carrier
TGA	Thermogravimetric Analysis
RP	Ruddlesden-Popper phase

SEM	Scanning Electron Microscope
PT	Parabolic Trough
LF	Linear Fresnel
CR	Central Receiver
DE	Dish Engine
CPC	Compound Parabolic Concentrator
IIR	Indirectly Irradiated Receiver
DIR	Directly Irradiated Receiver
HTF	Heat Transfer Fluid
TR	Thermal Reduction
CCL	CO_2 Circle Lab
MFC	Mass Flow Controller
IR	Infrared
TCD	Thermal Conductivity Detector
ppm	parts per million
SOEC	Solid Oxide Electrolyte Cell
PEM	Polymer Electrolyte Membrane
HV	Heating Value
LHV	Lower Heating Value
CL	Chemical Looping
EL	Electrolyzer
DNI	Direct Normal Irradiation
TMY	Typical Meteorological Year
TRL	Technological Readiness Level

1. Introduction

1.1 Greenhouse Gases and climate change

Emissions of Greenhouse Gases (GHG) have been growing for the past decades and are widely recognized as the principal cause of global warming and climate change. According to the Climate Change Synthesis Report of 2014 [1] by the Intergovernmental Panel for Climate Change (IPCC), the effects of anthropogenic greenhouse gas emissions, including mainly carbon dioxide CO_2, methane CH_4 and nitrous oxide N_2O, are extremely likely to constitute the dominant factor in causing the observed warming since the mid-20th century. In particular, 2019 was the second warmest year and 2010-2019 was the warmest decade ever recorded [2]. Simultaneously, CO_2 emissions in the atmosphere are also increasing. The main source of these emissions is the energy sector. In 2016, this sector was responsible of 73.2% of the global GHG emissions, which were equal to 49.4 billions of tonnes (49.4 Gt) of CO_2eq. [3]. As such, in order to reduce the effects of climate change it is especially important to act on the energy sector. CO_2 emissions from energy use increased with an average growth of 1.1% per year between 2010 and 2019, with an unusually strong increase of 2.1% in 2018 and a milder increase of 0.5% in 2019 [4]. The value reached in 2019 is equal 33 Gt of CO_2 [5]. If the emissions keep increasing in the coming years, it will not be possible to fulfill the commitment of the Paris Agreement of 2015, whose aim is to limit global warming with respect to pre-industrial levels to well below 2°C, and preferably below 1.5°C.

The energy-related CO_2 emissions are caused by the consumption of fossil fuels, like coal, oil and natural gas, which release CO_2 when they are burned. While coal consumption is slowly decreasing (0.6% decrease in 2019), oil and natural gas consumptions are rising, by 0.9% and 2% in 2019 respectively [4]. Fossil fuels constitute the majority of the primary energy sources used at a global level, making up 84% of the global primary energy consumption in 2019. The remaining

consumption derives from nuclear energy and renewables. Figure 1 shows the world primary energy consumption divided by source, from 1994 to 2019.

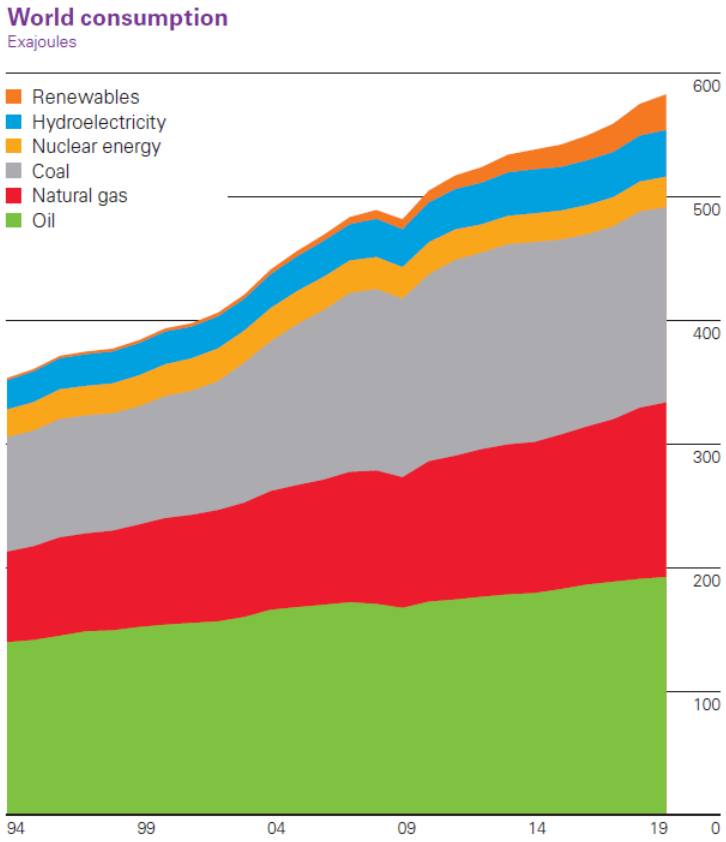

Figure 1: Global primary energy consumption from 1994 to 2019 divided by source [4].

This total energy consumption increased every year except 2009, where it decreased due to the economic crisis. Among the main drivers of energy use there are, in fact, population size and economic activity [1]. As the world population size is expected to grow in coming years, the world energy consumption, and thus the GHG emissions, are expected to rise as well. Actually, the expected increase will come after a slight reduction caused by the Covid-19 pandemic, which resulted in containment measures like lockdowns that in turn generated a reduction in energy demand and economic activity. Global CO_2 emissions were 5% lower in the first quarter of 2020 with respect to the first quarter of 2019 [6]. However, this short-term reduction is not expected to have an impact on the long-term effects of climate change, as CO_2 stays in the atmosphere and oceans for centuries [7]. In addition, emissions in 2020 seem to have already become greater than in 2019 by December,

after being below the 2019 levels for the rest of the year [8]. In conclusion, an important challenge in the years to come will be about meeting an increasing global energy demand without increasing the GHG emissions at the same time.

1.2 Renewable energy and renewable fuels

A first step in reducing carbon emissions is to use energy which is not coming from fossil fuel resources. Renewable energy sources, excluding hydroelectric power, contributed to 5% of the world primary energy consumption in 2019 [4], and their demand is rapidly growing. The global growth in primary energy consumption in 2019 was estimated to be equal to 7.7 EJ, and 41% of this growth (3.2 EJ) was covered by renewables. Renewable power generation also exceeded nuclear power generation for the first time in the same year. Various different types of renewable energy sources exist, like hydroelectric, solar (thermal or photovoltaic), wind, geothermal and biomass. Consumption of hydropower is higher than that of all the other renewables combined (6.4% of the total, with respect to the 5% of the other renewables) but is not growing as fast, as it contributed only to 4% of the global growth, much less than the 41% of the other renewables. As shown in figure 2 below, most of the primary energy consumption coming from renewable sources (excluding hydropower) comes from solar or wind energy.

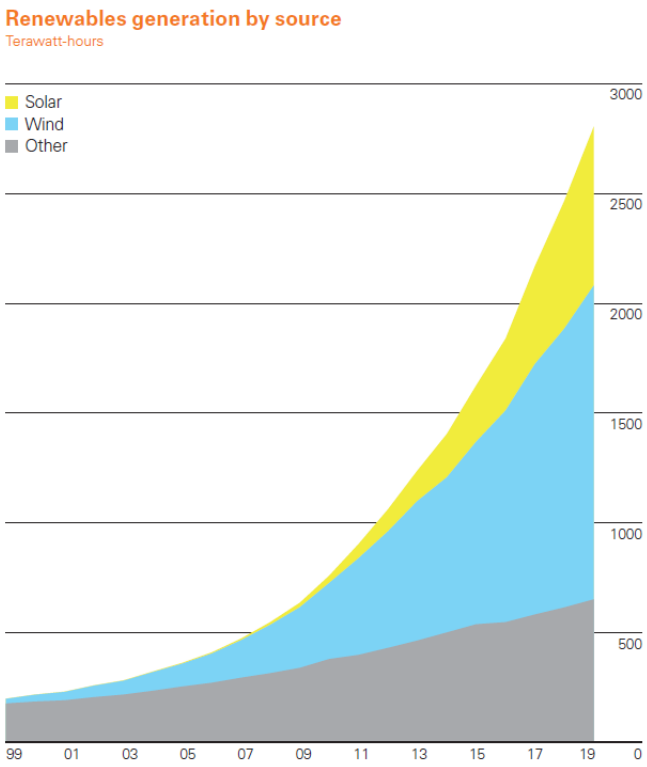

Figure 2: Global renewable energy production from 1999 to 2019, divided by source [4].

In the figure, the rapid growth of wind and solar energy production in the decade 2010-2019 is also displayed. An important issue regarding the substitution of fossil fuels with solar and wind energy is the intermittence of the availability of the last two. While fuels can be easily stored and used when needed, the availability of sun and wind changes during a day and from one day to another, and does not follow the demand. Therefore, methods to store the excesses of available renewable energy are needed. Globally, the excesses of energy can actually be much higher than the global demand. For example, the solar radiation reaching the Earth surface in one year has been estimated to be approximately $3.4 \cdot 10^6$ EJ [9], which is about 6'000 times greater than the global consumption of energy in 2019.

A possible method to store solar energy is the conversion of this energy into storable fuels. In this way, renewable energy can directly replace the fossil fuels in their applications. Moreover, these synthetic fuels are renewable, as they are not extracted from an exhaustible source like fossil fuels. As solar energy is employed in the production of such fuels, they are generally named "solar fuels". Solar fuels can be carbon-free, like solar hydrogen. In this case, their combustion will not

produce CO_2, and will not contribute to GHG emissions. Other fuels will instead be a cause of emissions when used, as they contain carbon atoms. However, if CO_2 is used as starting material to produce the solar fuel, the process will prevent carbon dioxide emissions initially and postpone them. Then, if Carbon Capture and Storage (CCS) systems are employed where the fuel is utilized, the CO_2 can be recovered and used to produce more fuel. From this perspective, carbon dioxide is not treated as a waste, but as a carbon-containing raw material for the production of fuels [10]. The following section focuses on how to use CO_2 to produce synthetic fuels.

2. Literature review

2.1 From carbon dioxide and water to fuels

2.1.1 Electrochemical processes

The techniques to generate fuels starting from solar power can be subdivided into three main pathways: electrochemical, photochemical and thermochemical processes [11]. Electrochemical processes are the most developed of the three pathways, and perform the decomposition of the starting molecules, i.e. CO_2 and H_2O, splitting them in CO and H_2. Oxygen is also released as by-product. The decomposition process is called electrolysis. It takes place in an electrochemical cell, which consists of two electrodes (the anode and the cathode), an external circuit, and an electrolyte. One of the electrodes produces the molecules of fuel and the other one releases oxygen. The external circuit provides the electric power that drives the process, while the electrolyte closes the cycle. A scheme of the electrochemical cell, in the case of water splitting into hydrogen and oxygen, is shown in figure 3.

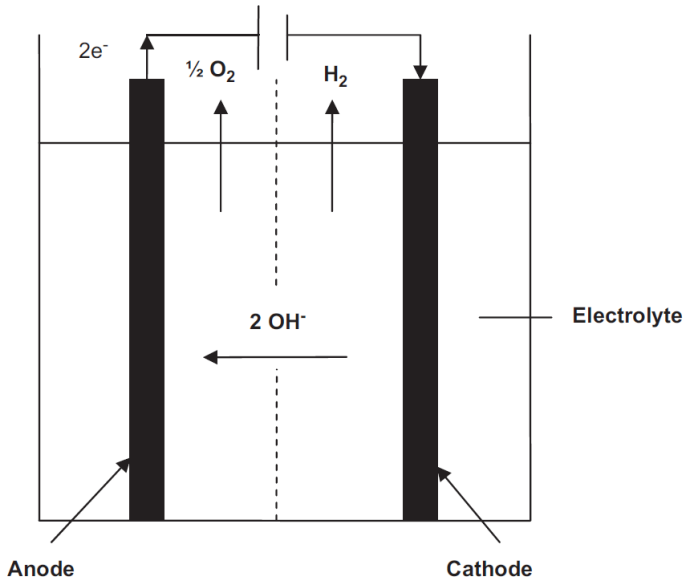

Figure 3: Structure of an electrochemical cell used for water splitting [11].

Electrolysis can be performed both at low and at high temperature, and requires electric power. In principle, this power can be obtained from any source. As the desired primary resource is solar energy, the electrolyzer would be in this case connected to a photovoltaic (PV) system. Therefore, the main drawback of this process is its dependence on the cost of PV electricity. Various solar hydrogen projects have been developed, like for example those in Italy [12] and in Germany [13, 14]. The PHOEBUS project [14], in particular, employed a 43 kW_p photovoltaic generator to produce hydrogen, and the hydrogen was later used to power a fuel cell and supply electricity to several offices.

2.1.2 Photochemical processes

Photochemical processes are based on the use of solar light to split CO_2 and H_2O. In particular, the photochemical process can be photobiological or photoelectrochemical. In the first case, small organisms like algae or bacteria are used to catalyze the required reaction at ambient temperature through their enzymes. The main drawback of this approach is the low fuel yield. In the second case, a photoelectrochemical cell (PEC) is used. Unlike the electrochemical cell described above, where the redox reactions of the electrodes are driven by an external power source, in the PEC the solar radiation is the driver, due to the semiconducting nature of the electrodes. The semiconductor, when illuminated by sunlight, produces an electric current, like a photovoltaic cell. This current is immediately used to drive the splitting reactions. The system, again in the case of a cell used for water splitting, is outlined in figure 4 below.

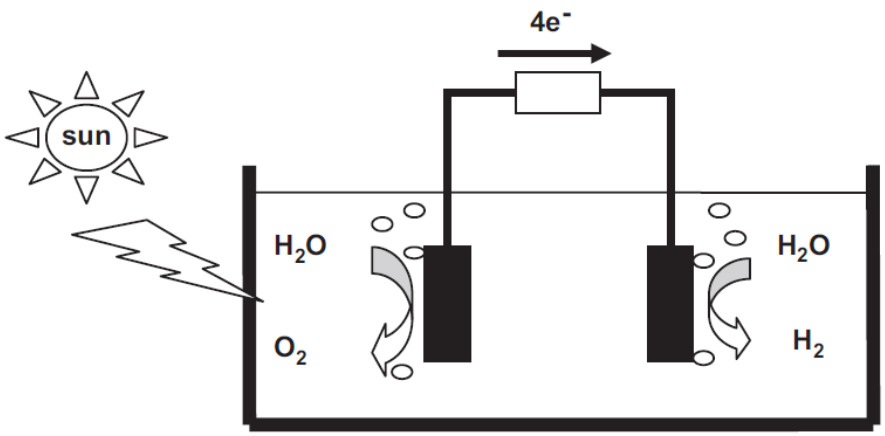

Figure 4: Structure of a photoelectrochemical cell used for water splitting [11].

While electrochemical cells are already developed at commercial level, photoelectrochemical processes are still under the stage of investigation, and their implementation in real plants is expected only in the long term.

2.1.3 Thermochemical processes

The third type of pathway to produce fuels from platform molecules and solar energy is the thermochemical one. In this case, the energy needed to split H_2O and CO_2 is provided in the form of heat. A concentrated solar power (CSP) system is used to concentrate solar radiation in a small area and thus maintain high temperatures in a reactor where the splitting reaction occurs. If the dissociation is realized in a single step, the process is called thermolysis. This process has two main issues, however. Firstly, very high temperatures are needed for thermolysis to occur, such as above 2500 K for water [10]. Additionally, the products of the splitting reaction are released as gases at the same time, with the possibility of creating an explosive mixture, like a mixture of H_2 and O_2. So, the process requires an effective separation of the gaseous products, which is challenging to realize. These problems are solved by employing a thermochemical cycle, which is a procedure that consists in at least two steps. The additional steps allow to separate the production of fuel and the production of oxygen, making them take place in different locations. Moreover, the maximum temperature step requires a temperature lower than that of the single step direct thermolysis. The simplest thermochemical cycles are the two-step cycles, which can be based on three types of materials: oxides, hydrides and hydroxides [15]. The reactions involved in the three cases are shown in the equations below, where XO, XH_2 and XOH are a generic oxide, hydride and hydroxide respectively.

$$Oxide\ reaction\ 1\ (oxygen\ production): XO \rightarrow X + \frac{1}{2}\ O_2 \quad (2.1)$$

$$Oxide\ reaction\ 2\ (hydrogen\ production): X + H_2O \rightarrow XO + H_2 \quad (2.2)$$

$$Hydride\ reaction\ 1\ (hydrogen\ production): XH_2 \rightarrow X + H_2 \quad (2.3)$$

$$Hydride\ reaction\ 2\ (oxygen\ production): X + H_2O \rightarrow XH_2 + \frac{1}{2}\ O_2 \quad (2.4)$$

$$Hydroxide\ reaction\ 1\ (oxygen\ production)\colon 2\ XOH \rightarrow 2\ X + H_2O + \frac{1}{2}\ O_2 \quad (2.5)$$

$$Hydroxide\ reaction\ 2\ (hydrogen\ production)\colon 2\ X + 2\ H_2O \rightarrow 2\ XOH + \ H_2 \quad (2.6)$$

For all the three materials, the cycle has an oxygen production step and a hydrogen production step, ensuring their separation. While hydrides and hydroxides can only be used for water splitting (WS), the oxide reactions can also work for the carbon dioxide splitting (CDS).

$$Oxide\ reaction\ 1\ (oxygen\ production)\colon XO \rightarrow X + \frac{1}{2}\ O_2 \quad (2.7)$$

$$Oxide\ reaction\ 2\ (carbon\ monoxide\ production)\colon X + CO_2 \rightarrow XO + CO \quad (2.8)$$

With an oxide material, the WS and the CDS reactions can be combined to produce H_2 and CO together, leading to the production of syngas.

2.2 Syngas applications

2.2.1 Methane production

Syngas is a gas mixture that includes both hydrogen H_2 and carbon monoxide CO. It is a versatile product which can be used as fuel directly, or to produce other fuels and chemicals. For example, syngas can produce methane CH_4 through the methanation reaction.

$$CO + 3\ H_2 \rightarrow CH_4 + H_2O \quad (2.9)$$

As shown by the chemical equation, the optimal H_2/CO ratio for the production of methane is equal to 3. The product methane is also known as Synthetic Natural Gas (SNG), in order to make a distinction between this artificial gas and the fossil one. An example of methanation process is the TREMP™ (Topsøe Recycle Energy-efficient Methanation Process), introduced by a collaboration of German and Danish scientists [16]. It uses three adiabatic reactors (R1, R2 and R3) like those

shown in figure 5 below. The plant receives a feed which can contain H_2, CO and CO_2. CO_2 can also react with H_2 to produce CH_4.

$$CO_2 + 4\,H_2 \rightarrow CH_4 + 2\,H_2O \qquad (2.10)$$

The methanation reactions are both highly exothermic. The enthalpies of reaction are -206 kJ/mol for the one with CO as reactant and -165 kJ/mol for the one with CO_2 [17]. In order to avoid an excessive increase of temperature, which would also penalize the exothermic reaction, the process is split into the three reactors, with a cooler added between the first two.

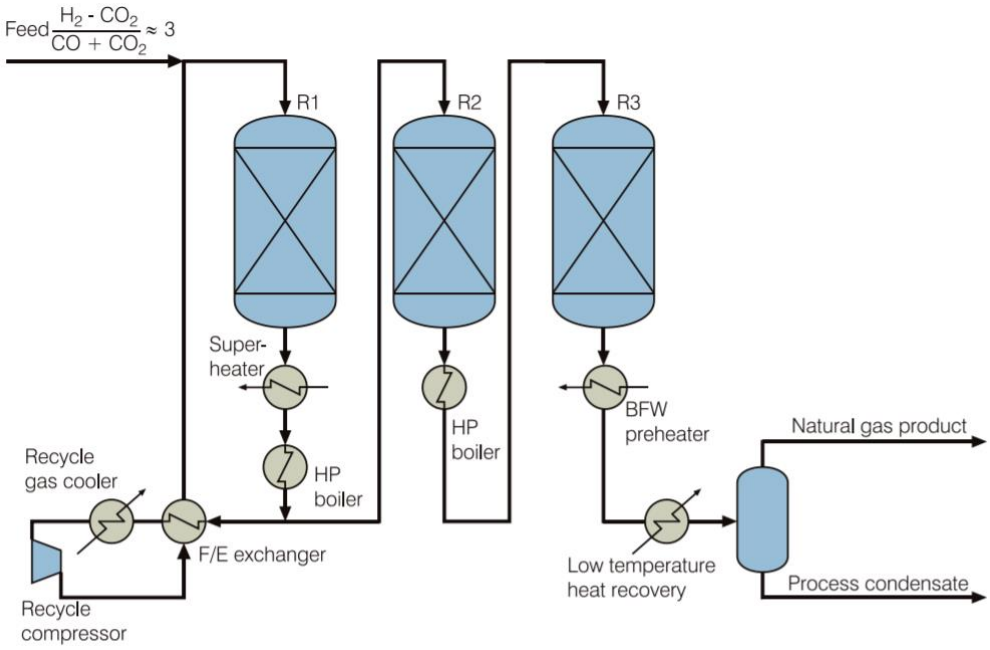

Figure 5: Structure of the TREMP^{TM} methanation plant [16].

The product of the reactors is a mixture of methane and steam. By condensing the steam, high-purity CH_4 (94-98%) is obtained.

2.2.2 Methanol production

Syngas can also be used as a precursor to synthetic liquid fuels that serve as substitutes for diesel fuel or gasoline. Liquid fuels are especially useful in sectors where a high energy density is needed, like aviation or shipping. Figure 6 shows the energy density of Li-ion batteries and various types of fuels. The liquid fuels which can be produced starting from syngas are in bold. Energy density can be

expressed as energy per unit of mass (gravimetric energy density, in kWh/kg in the diagram) or as energy per unit of volume (volumetric energy density, in kWh/l in the diagram). With respect to batteries, liquid fuels have a higher density, in both gravimetric and volumetric terms. Natural gas (NG) and hydrogen can be better in gravimetric terms, but occupy much larger volumes.

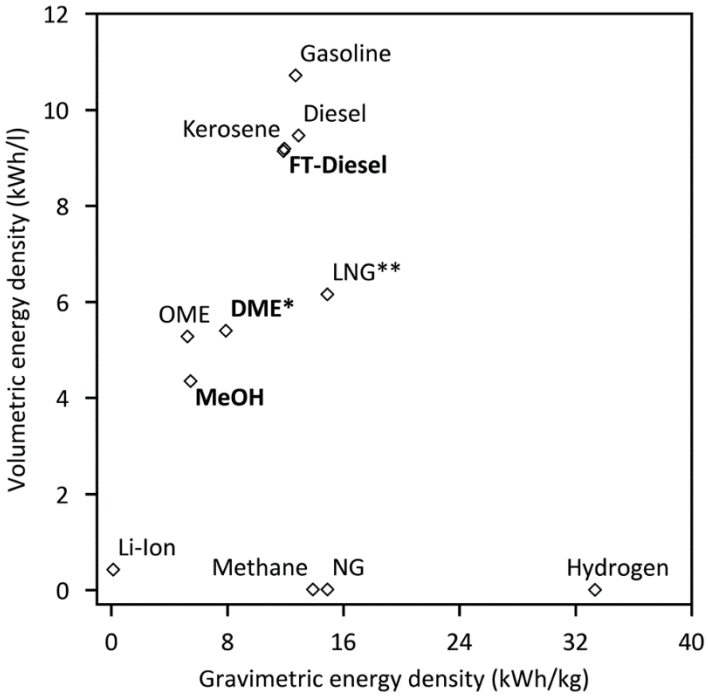

Figure 6: Energy density of fuels and Li-ion batteries [18].

The liquid fuels which can be obtained starting from syngas shown in the diagram are methanol CH_3OH (MeOH), dimethyl ether CH_3OCH_3 (DME) and Fischer-Tropsch diesel fuel (FT-Diesel). DME is actually gaseous at ambient conditions, but it can be liquified with moderate pressures (5 bar). In figure 1, the values of specific energy of DME are expressed at 10 bar. Similarly, the energy density of LNG (Liquified Natural Gas) is expressed at the temperature of -160°C.

A simplified scheme of a plant that produces a liquid fuel from syngas is shown in figure 7. As the reactions involved are exothermic, a cooling system is required. A recycle of unconverted syngas can also be used to limit the temperature rise in the reactor and keep the optimal syngas composition at the reactor's inlet.

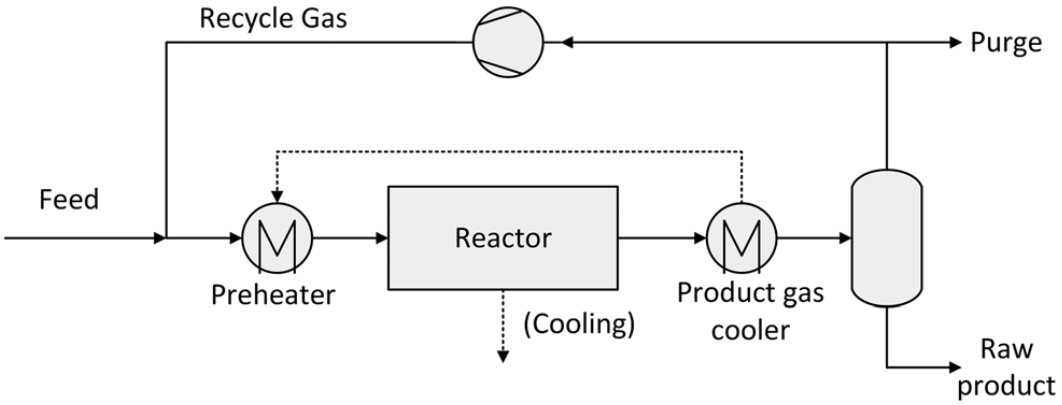

Figure 7: Simplified scheme of a syngas to liquid fuel plant [18].

Methanol can work in both diesel and Otto (gasoline) engines as fuel. It is also miscible with gasoline, and methanol-gasoline mixtures have been used in Otto engines with little modifications in Brazil and in Sweden [18]. However, MeOH has a low energy density, about half than gasoline and diesel in both gravimetric and volumetric terms. The H_2 and CO conversion into methanol is expressed as:

$$CO + 2\,H_2 \rightarrow CH_3OH \qquad (2.11)$$

Differently from the CH_4 production, where the optimal H_2/CO ratio is 3, for the methanol production the optimal value is 2. So, different types of syngas, in terms of hydrogen and carbon monoxide content, are suitable to produce different fuels. CH_3OH production is also exothermic, but less than CH_4 production, with an enthalpy of reaction equal to -90.6 kJ/mol compared to the -206 kJ/mol of methane. Methanol production plants are already present both at small (10-200 tons per day of production rate) and large scale (up to 10'000 tons per day). Large scale plants mainly obtain the starting syngas from methane (natural gas reforming) or from coal gasification, while syngas from renewable energy and captured CO_2 is for now limited to small scale plants [19].

2.2.3 Dimethyl ether production

DME can be used in diesel engines and while it is characterized by a lower energy density with respect to diesel fuel, it has the advantage of avoiding particle emissions, as it lacks bonds between carbon atoms (C-C bindings). In addition, DME does not contain sulfur. In order to use DME in a diesel engine, some

modifications are needed as the fuel has to be constantly kept liquid through pressure. DME can be produced by dehydration of methanol through the following reaction:

$$2CH_3OH \rightarrow CH_3OCH_3 + H_2O \qquad (2.12)$$

However, CH_3OCH_3 can also be obtained directly from syngas, through two possible pathways. The first one produces DME and CO_2, and has an optimal H_2/CO ratio of 1:

$$3\,CO + 3\,H_2 \rightarrow CH_3OCH_3 + CO_2 \quad \Delta H = -246.0\,kJ/mol \qquad (2.13)$$

The second pathway produces DME and H_2O, and is instead characterized by an optimal H_2/CO ratio of 2.

$$2\,CO + 4\,H_2 \rightarrow CH_3OCH_3 + H_2O \quad \Delta H = -205.0\,kJ/mol \qquad (2.14)$$

Both pathways are exothermic and reduce the number of moles from reactants to products. Hence, they are favored by low temperatures and high pressures. Real direct DME synthesis plants work at 200-300°C and 30-70 bar. Figure 8 shows the conversion of the starting syngas into methanol and DME as a function of the H_2/CO ratio. The curves on the diagram were obtained through simulations at the conditions of 260°C of temperature and 50 bar of pressure [18]. The conversion values are consistent with the optimal ratios that can be obtained from the chemical equations: methanol production and DME+H_2O production have their maximum conversion for $H_2/CO = 2$, while the DME+CO_2 production peaks for $H_2/CO = 1$.

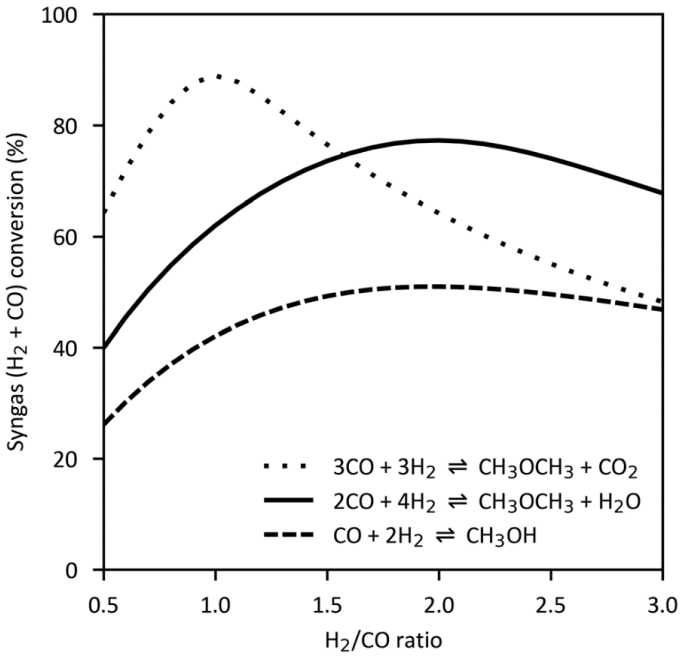

Figure 8: Syngas conversion into methanol or DME as a function of the H2/CO ratio [18].

Currently, all DME production plants at a large scale are based on a two-step process. Syngas is firstly used to produce methanol, and then the methanol is dehydrated to obtain DME, if needed. In this way, CH_3OH and CH_3OCH_3 can be produced at the same time and their production ratio can be varied following the market demand [18]. Direct DME synthesis from syngas has for now been developed, only at pilot plant scale, by different companies. Some of them (JFE, KOGAS, Air Products and Chemical) perform the reaction through the first pathway, obtaining CO_2 as a by-product. Haldor Topsøe, instead, follows the second pathway, which produces H_2O and not carbon dioxide.

2.2.4 Fischer-Tropsch fuels

Finally, syngas is the starting material for the Fischer-Tropsch (FT) process, which converts H_2 and CO into liquid hydrocarbons. The process has been developed in the early 20th century, with the objective of producing liquid fuels starting from coal. Fischer and Tropsch published their findings in 1923 and the first pilot plant was built in 1930 [18]. The three reactions taking place in a FT reactor are shown below. In the equations, n is the length of the resulting carbon chain, and usually varies between 10 and 20.

$$n\,CO + (2n+1)\,H_2 \rightarrow C_nH_{2n+2} + n\,H_2O \qquad (2.15)$$

$$n\,CO + (2n)\,H_2 \rightarrow C_nH_{2n} + n\,H_2O \qquad (2.16)$$

$$n\,CO + (2n)\,H_2 \rightarrow C_nH_{2n+1}OH + (n-1)\,H_2O \qquad (2.17)$$

The product hydrocarbons are alkanes C_nH_{2n+2}, alkenes C_nH_{2n} and alcohols $C_nH_{2n+1}OH$. Water is a by-product and can be converted to additional hydrogen using CO through the following water-gas shift (WGS) reaction.

$$CO + H_2O \rightarrow H_2 + CO_2 \qquad (2.18)$$

The optimal H_2/CO ratio for the FT synthesis is around 2. By varying the syngas composition, the catalyst type (which can be Fe or Co), and the conditions of temperature and pressure, the composition of the resulting mixture of hydrocarbons changes. High temperatures lead to shorter chains, while high pressures favor long-chain products. In general, FT processes work at temperatures in the range 150-300

°C. Above 300°C, the chains of the hydrocarbons produced are too short, closer to gaseous methane than to liquid fuels. In addition, above 350°C solid carbon deposits in the reactor can occur. The liquid fuels obtained can substitute diesel fuel (longer chains, lower temperatures required) or gasoline (shorter chains, higher temperatures required). Low-Temperature Fischer-Tropsch (LT-FT) reactors produce mainly waxes, which are closer to diesel fuels, while High-Temperature Fischer-Tropsch (HT-FT) reactors produce alkanes and gasoline. The weight fraction of a certain alkane obtained is generally expressed by the Anderson-Schulz-Flory distribution, whose equation is shown below [18].

$$W_n = n(1-\alpha)^2\alpha^{n-1} \qquad (2.19)$$

In the formula, n is the carbon chain length in terms of number of carbon atoms, while α is called chain growth probability. The higher the value of α, the higher the probability of obtaining longer chains from the FT reaction. Chain growth probability depends on pressure, temperature, syngas composition and catalyst type. Figure 9 shows the cumulative weight fraction in % as a function of α. For low values of growth probability (α = 0.75), shorter chain hydrocarbons like gasoline are the main product, while for α close to 1 waxes and diesel fuel are more probable.

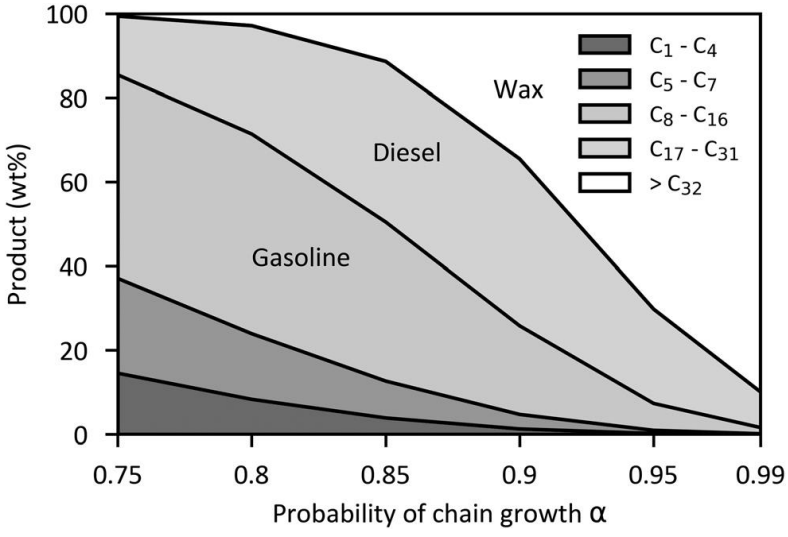

Figure 9: Cumulative weight fraction of FT synthesis products as a function of growth probability α [18].

The first FT large scale plant, SASOL 1, started in 1955 in South Africa, and combined both LT-FT (230°C) and HT-FT (340 °C) processes, allowing the

production of different synthetic fuels [20]. Many large-scale plants, producing about 100'000 bpd (barrels per day) of fuel, exist, but only with syngas obtained from fossil fuels, like coal or methane. The largest GtL (gas-to-liquid) plant, using methane to produce fuels, is Pearl GtL, in Qatar, with 140'000 bpd of production. In order to substitute fossil fuels, projects that implement the FT process with syngas from renewable sources have been developed, but in this case the scale is much smaller. For example, in Güssing, Austria, the Technical University of Vienna built a BtL (biomass-to-liquid) demonstration plant. The plant produces syngas from biomass. Then, the syngas can be used in three different ways: directly in a CHP (Combined Heat and Power) gas engine that produces both heat and electricity, in a demonstration plant that produces methane (also called BioSNG), or in a laboratory FT plant. A flowsheet of the Fischer-Tropsch plant is shown in the figure below.

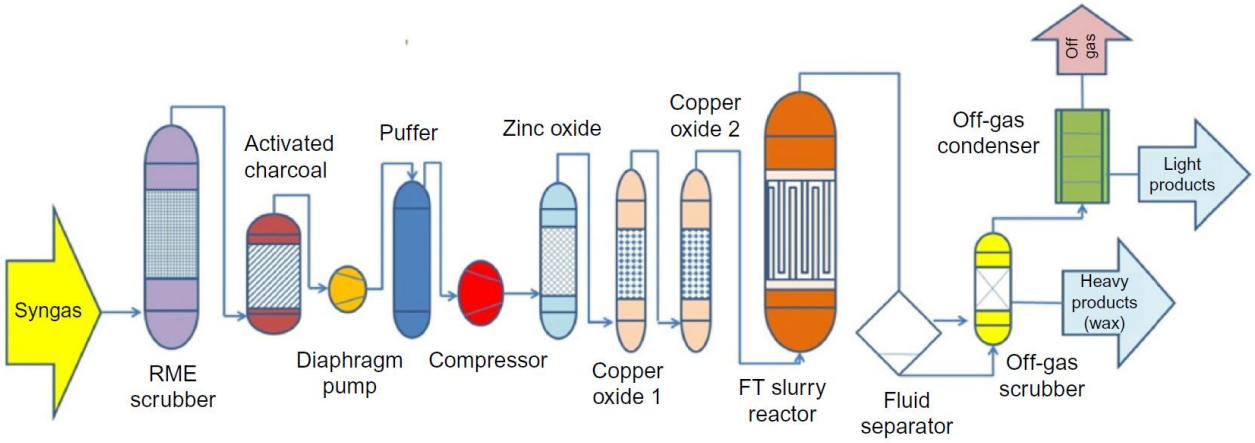

Figure 10: Scheme of the syngas to fuel FT plant in Güssing, Austria [20].

The starting components of the plant are needed to clean the syngas. As it originates from biomass, the syngas contains gases different from H_2 and CO, like sulfur compounds and organic compounds, which have to be removed before the FT reaction. A syngas obtained from CO_2 and H_2O via electrochemical or thermochemical cycles would be already free of those contaminants.

In conclusion, syngas is a versatile gas already used at large-scale, commercial level to produce synthetic fuels. However, most plants currently use as feedstock a syngas coming from fossil fuels. As syngas can also be obtained from renewable sources through various processes, the challenge is to develop these processes. The following sections describe more in detail the thermochemical type of process.

2.3 Thermochemical processes

2.3.1 Chemical looping in general

A chemical looping process consists in subjecting a material to a cycle of chemical reactions. In this case, a solid material called Oxygen Carrier (OC) is used. The chemical reactions need external heat, supposed to come from the sun, so that the process is driven by renewable energy. In the chemical loop the oxygen carrier undergoes a series of redox (reduction and oxidation) reactions.

Firstly, the oxygen carrier is reduced using the high temperature coming from the solar concentrators, thereby releasing oxygen. Then, the reduced oxygen carrier reacts at a lower temperature with CO_2 and/or H_2O, extracting oxygen from them. The reaction with CO_2 produces CO, while the reaction with H_2O produces H_2, so that a syngas is obtained. The scheme of a chemical looping process using an oxygen carrier to produce syngas is shown below.

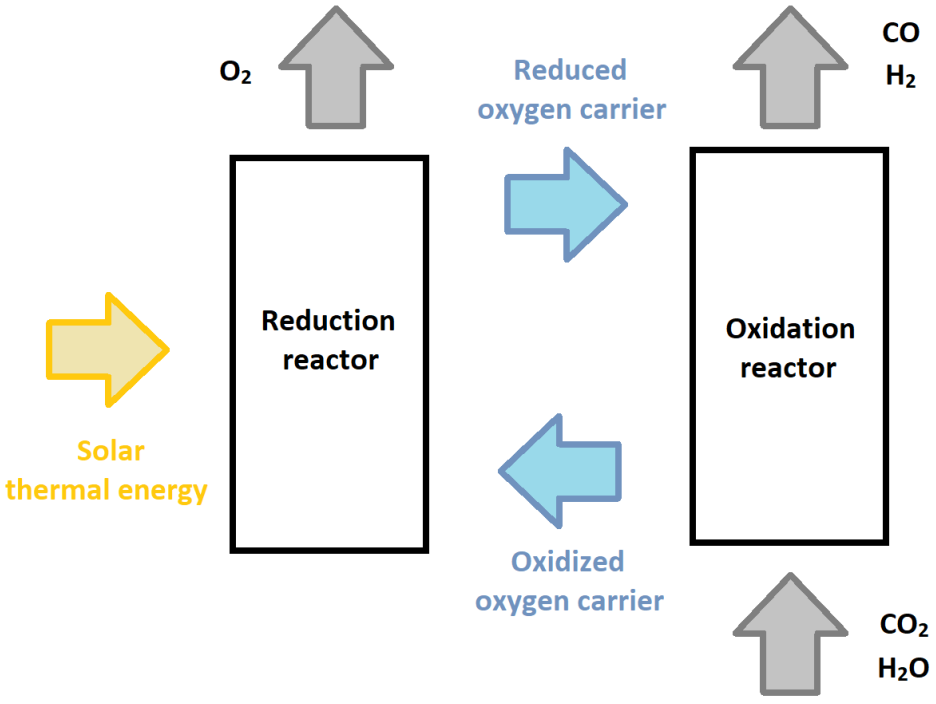

Figure 11: Scheme of a chemical looping process to produce syngas.

If the process uses carbon dioxide coming from the use of fossil fuels as reactant to produce CO, it prevents the release of CO_2 in the atmosphere. Carbon dioxide is recycled back and becomes a resource.

The efficiency of the chemical looping process highly depends on the material used as oxygen carrier. The numerous types of oxygen carriers can be divided according to volatility and stoichiometry.

2.3.2 Volatile oxygen carriers

Volatile materials like zinc oxide (ZnO) sublimate during the reduction reaction, transforming from a solid state into a vapor. The solid zinc oxide, at very high temperatures (2000 °C), splits into metallic zinc (in form of vapor) and oxygen. In the second part of the loop, Zn reacts with CO_2 and H_2O. The reactions of the loop are as follows:

$$Thermal\ reduction\ at\ 2000°C:\ \ ZnO \rightarrow Zn + 1/2\ O_2 \tag{2.20}$$

$$Oxidation\ with\ CO_2:\ \ Zn + CO_2 \rightarrow ZnO + CO \tag{2.21}$$

$$Oxidation\ with\ H_2O:\ \ Zn + H_2O \rightarrow ZnO + H_2 \tag{2.22}$$

A stoichiometric process ensures a higher productivity of CO and H_2, with respect to a non-stoichiometric one. The downside, however, is that the reaction requires a temperature of 2000°C, not easily obtainable with solar thermal power. In addition, higher temperatures mean higher costs of components.

A study by Steinfeld [21] calculated the efficiency of the ZnO/Zn cycle for solar hydrogen production and investigated its economic feasibility. In the study, the plant consists of a solar concentrator containing the reduction reactor, a quench that is used to separate Zn and O_2 to avoid their recombination, a hydrolyser where the oxidation reaction occurs and the hydrogen is obtained, and a fuel cell that uses the H_2 and O_2 produced in the reaction to generate electricity and heat. The flow diagram of the plant is shown in figure 12.

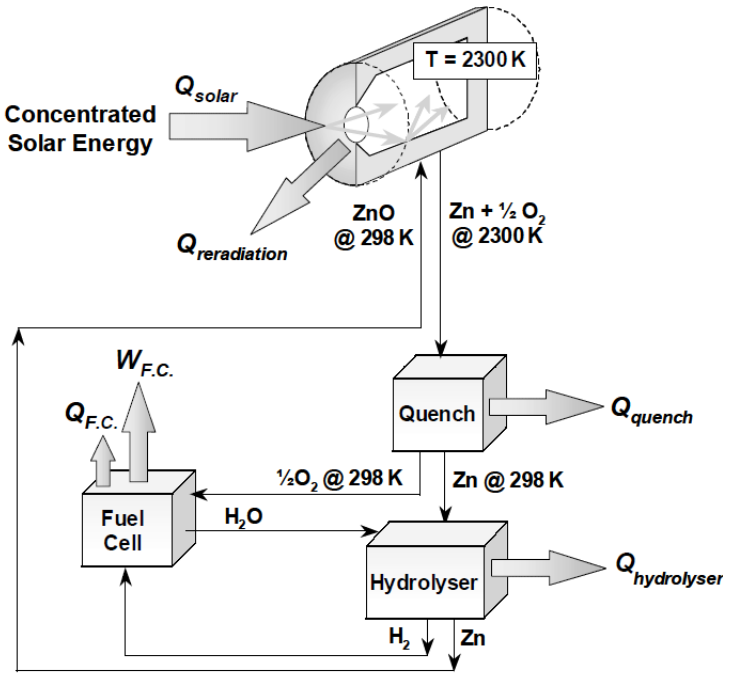

Figure 12: Flow diagram of a solar hydrogen thermochemical cycle based on ZnO [21].

The diagram highlights the flows of energy, like the heat and electricity produced by the fuel cell and the losses due to reradiation of the solar concentrator and the quench of Zn and O_2. The solar to chemical efficiency, that is the efficiency of the hydrogen production, not considering the fuel cell, is 29%. The economic analysis indicated a cost of hydrogen of 0.13-0.15 $/kWh, which is competitive with the cost of solar hydrogen obtained through electrolysis of water, but still higher than the cost of non-renewable hydrogen, obtained from fossil fuels. A different study, by Galvez et al. [22], analyzed a thermochemical cycle based on zinc oxide for the production of CO from CO_2, with thermal reduction at 2000 K, and obtained a solar to chemical efficiency of 39%.

Other volatile cycles with different oxygen carriers that have been studied include cycles based on CdO/Cd [23], SnO_2/SnO [24] and GeO_2/GeO [25]. All of them require a temperature of at least 1400 K.

2.3.3 Ceria as oxygen carrier

In order to reduce the required temperatures, a non-stoichiometric material like ceria (CeO_2) can be used as oxygen carrier. Non-stoichiometric ceria was first suggested as a material for hydrogen production by Japanese researchers in 1983 [26]. They proposed a temperature range of 773-973 K (500-700°C) for the reduction. With a non-stoichiometric material, the reduction produces an oxide with a lower concentration of oxygen: $CeO_{2-\delta}$. The value δ is called non-stoichiometry, and depends on the conditions of the reaction, such as temperature (T) and oxygen partial pressure (pO_2). In particular, δ increases for high T and low pO_2, as these conditions move the reaction equilibrium of the reduction towards the products [27]. The reactions are shown below.

$$Thermal\ reduction:\ \ CeO_2 \rightarrow CeO_{2-\delta} + 1/2\ \delta\ O_2 \quad (2.23)$$

$$Oxidation\ with\ CO_2:\ \ CeO_{2-\delta} + \delta CO_2 \rightarrow CeO_2 + \delta CO \quad (2.24)$$

$$Oxidation\ with\ H_2O:\ CeO_{2-\delta} + \delta H_2O \rightarrow CeO_2 + \delta H_2 \quad (2.25)$$

The reactions become more efficient for temperatures higher than 1200 K, much lower than the 2000°C required by ZnO. Ceria has been extensively studied for thermochemical cycles, due to the stability of its structure over different working conditions and non-stoichiometry values [27]. Its main drawback is the low reduction extent, which means that it does not release big amounts of oxygen during the reduction step of the thermochemical cycle. The low reduction extent reduces the fuel production yield. Haeussler et al. [27] used a thermogravimetric analysis (TGA) of 100 mg of material to estimate the amount of carbon monoxide that can be produced. The TGA was performed in the following conditions. The thermal reduction was carried out at 1400 °C for 45 minutes. Then, temperature was reduced at 1050°C for the oxidation step, which lasted 60 min. During this step, ceria reacted with a mixture containing 50% of CO_2, producing CO, and 50% of Ar, which is inert. This redox cycle was repeated twice. The amount of carbon monoxide produced is expressed in μmol of CO per g of CeO_2, and the value obtained is 95 μmol/g. In order to enhance the reduction extent, ceria can be doped with different materials, like aluminum (Al) and zirconium (Zr). The increase of reduction extent, however, comes at a cost, as the re-oxidation extent of doped ceria, due to a slower reaction kinetics, is lower than that of pure ceria. A lower re-oxidation extent means

that during the oxidation step with CO_2, the material does not fill all the oxygen vacancies previously created during the reduction step. The trade-off between a higher reduction extent and a lower re-oxidation extent results in yields for doped ceria that can be higher than, similar to, or even lower than pure CeO_2. Among the compositions studied by Haeussler et al., only $Ce_{0.85}Zr_{0.15}O_2$, referred to as CeZr15, has a yield higher than CeO_2, with a CO production of 144 µmol/g. The figure below shows the results of the TGA experiment for CeO_2, $Ce_{0.85}Zr_{0.15}O_2$ (CeZr15), $Ce_{0.63}Zr_{0.37}O_2$, (CeZr37) and $Ce_{0.63}Zr_{0.27}Al_{0.1}O_2$ (CeZr27Al10). The reduction of mass at the temperature of 1400°C is the reduction extent, as it corresponds to the release of oxygen. Conversely, the increase of mass at 1050°C is the re-oxidation extent, and it corresponds to the material absorbing oxygen from CO_2.

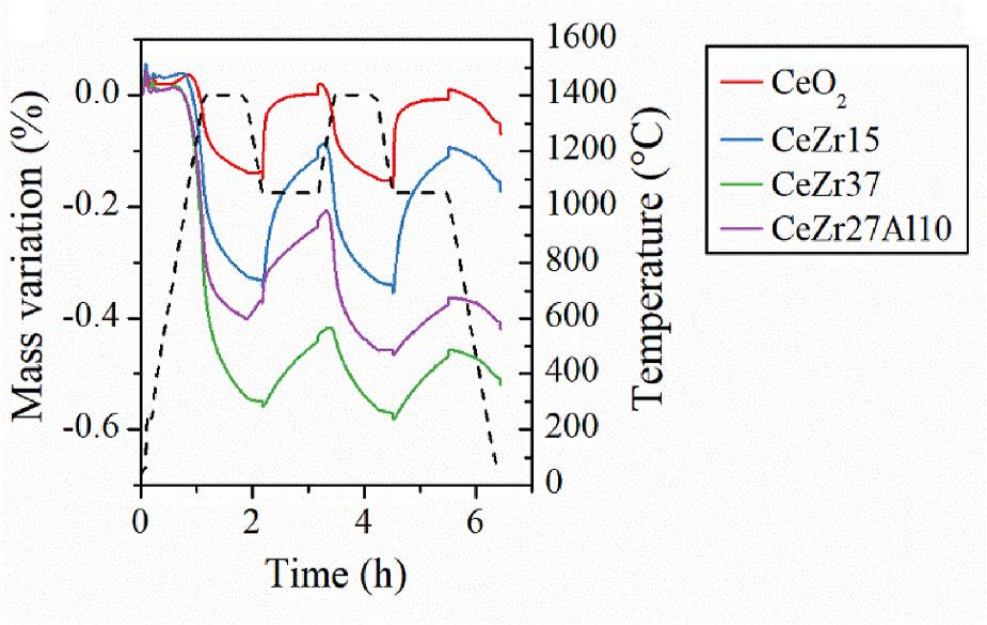

Figure 13: Temperature and mass variation during the TGA test of ceria and three different types of doped ceria [27].

As shown in the plot, the mass reduction for the pure ceria (red line) is much lower with respect to the other three. However, while the pure ceria almost returns to the starting value of mass during the re-oxidation, for the other compositions the value of mass at the end of the oxidation step is still considerably lower. The difference in mass between the end and the start of the oxidation is similar for the red, green and purple lines, indicating a similar CO yield. The blue line, corresponding to CeZr15, has instead a much higher mass variation, and this results in the higher CO yield. The fact that the slower reaction kinetics for doped ceria is the cause of the

lower re-oxidation extent can also be noticed from the plot. During the oxidation step, the red line quickly jumps from the lowest value of mass to the highest one, and the mass is stabilized well before the end of the oxidation. Meanwhile, for the other three lines the value of mass has not yet stabilized and is still increasing when the 60 min of the oxidation step are over, and CO_2 is not sent anymore to the crucible containing the material. It would be possible to obtain higher yields of CO from doped ceria by increasing the duration of this oxidation step.

2.3.4 Iron oxides as oxygen carrier materials

A different type of non-volatile oxygen carrier is based on Fe oxides. Iron has a low cost compared to other catalysts. Another peculiarity of iron is that three different levels of oxidation can be exploited in a chemical loop. Each of these oxidation states is associated to a mineral, as follows:

- Wüstite FeO, with oxidation state Fe^{2+}
- Magnetite Fe_3O_4, with oxidation state $Fe^{2.6+}$, which is a mixture of Fe^{2+} and Fe^{3+}
- Hematite Fe_2O_3, with oxidation state Fe^{3+}

A chemical looping process in three stages that uses these three oxidation states of Fe is presented by Ohio State University (OSU) in [28]. In this case, the energy to reduce the oxygen carrier does not come from a thermal source, but from a carbonized fuel, that contains for example methane CH_4 and carbon monoxide CO. If this fuel is utilized in ordinary applications, the CO_2 produced is usually difficult to capture. The aim of the process is to convert the carbonized fuel in a decarbonized one, specifically hydrogen H_2, and capture the CO_2 generated in the loop. The loop consists of the following three phases. Firstly, the magnetite Fe_3O_4, which corresponds to the intermediate oxidation state of iron, is sent to a component called combustor, where it is oxidized to the highest state, corresponding to hematite Fe_2O_3, using oxygen coming from air. As the reaction is exothermic, heat is also produced.

$$Combustor\colon\ 4\,Fe_3O_4 + O_2 \rightarrow 6\,Fe_2O_3 + Heat \tag{2.26}$$

Then, in the reducer, the hematite Fe_2O_3 reacts with the carbonized fuel. The products of this reaction are wüstite FeO, which is the lowest oxidation state of an iron oxide, and a stream of CO_2 and H_2O in steam form. The reactions of Fe_2O_3 with CH_4 and CO, two possible components of a carbonaceous fuel, are shown below.

$$Reducer:\ 4\,Fe_2O_3 + CH_4 \rightarrow 8\,FeO + CO_2 + 2\,H_2O \quad (2.27)$$

$$Reducer:\ Fe_2O_3 + CO \rightarrow 2\,FeO + CO_2 \quad (2.28)$$

CO_2 can later be captured by separating it from the steam. For example, the stream could be cooled down, making the steam condensate. The last part of the loop, the steam-iron reaction, takes place in an oxidizer, where the wüstite (FeO) reacts with H_2O. The products of this reaction are magnetite Fe_3O_4, which is sent to the combustor, and highly concentrated hydrogen H_2.

$$Oxidizer:\ 3\,FeO + H_2O \rightarrow Fe_3O_4 + H_2 \quad (2.29)$$

The figure below shows the three-stage chemical looping process.

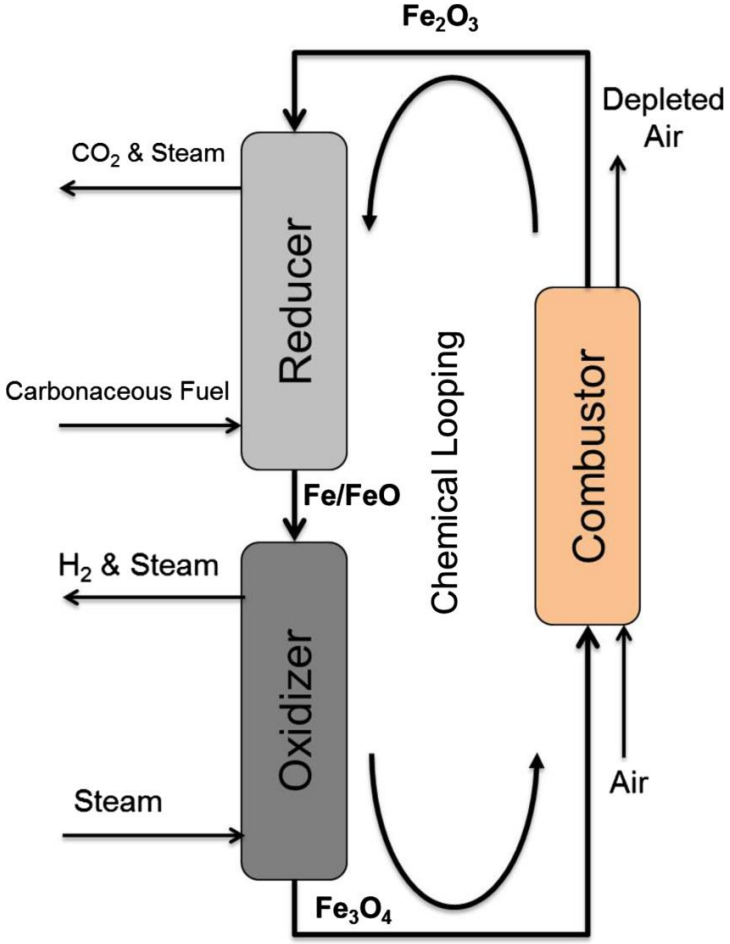

Figure 14: Three-stage chemical looping process that uses iron oxide as oxygen carrier [28].

Galvez et al. [22] studied the thermodynamics of a volatile two-step cycle using iron oxides to produce CO. Compared to the diagram in figure 14, in this case there is no combustor. The reactions involve only magnetite Fe_3O_4 and wüstite FeO. So, the maximum state of oxidation, corresponding to hematite Fe_2O_3, is not reached during the cycle.

$$Reduction: \quad Fe_3O_4 \rightarrow 3\,FeO + \frac{1}{2}O_2 \qquad (2.30)$$

$$Oxidation: \quad 3\,FeO + CO_2 \rightarrow Fe_3O_4 + CO \qquad (2.31)$$

The energy for the reduction phase is provided by a solar concentration system, which keeps the temperature in the reducer at 2000 K. The solar to fuel efficiency obtained is 29%, which is lower than the efficiency of 39% calculated for the Zn/ZnO cycle in the same conditions. The lower efficiency of the iron oxides was attributed to two causes. Firstly, the ZnO dissociation is characterized by a lower enthalpy change with respect to Fe_3O_4, and this lower value of enthalpy results in a 25% lower amount of solar heat needed to produce the same moles of O_2 during the thermal reduction. Then, Zn and ZnO have lower molar heat capacities with respect to FeO and Fe_3O_4, resulting in a reduced heat loss due to the quench phase, where the gaseous products of the reduction, O_2 and reduced oxygen carrier, are cooled down and separated. The quench losses for the iron oxides cycle are more than double than the losses for the zinc cycle.

2.3.5 Perovskite materials as oxygen carriers

Another class of materials that is being studied for non-stoichiometric thermochemical cycles are perovskite. A perovskite is characterized by a formula of the type ABO_3, where A and B are two different cations. Using the atomic radii r_A, r_B, and r_O, belonging to cation A, cation B and the oxygen anion O^{2-} respectively, the Goldschmidt tolerance factor t can be calculated through the following formula [29].

$$t = \frac{r_A + r_O}{\sqrt{2}(r_B + r_O)} \qquad (2.32)$$

The value of the Goldschmidt tolerance factor indicates if two cations A and B can form a perovskite structure, also depending on the geometry. For an ideal perovskite, t is equal to 1. For real perovskites, t has to be close to the ideal value of 1. In addition, r_A has to be between 1.10 and 1.80 Å, and r_B has to be between 0.62 and 1.00 Å. The ideal structure of a perovskite material, with the positions of cations A and B and anion O^{2-}, is shown in the following figure.

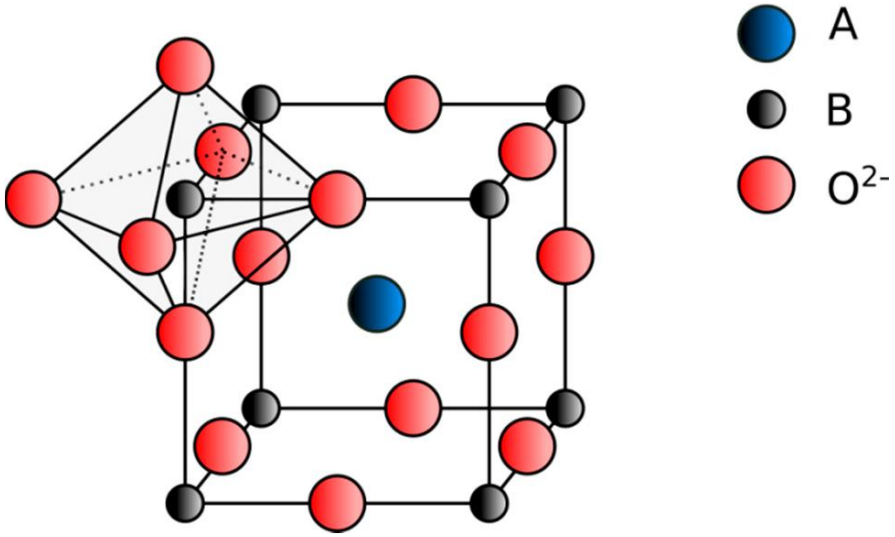

Figure 15: Ideal structure of a perovskite material [29].

The main property than makes perovskite materials good for thermochemical cycles is the high non-stoichiometry that they can achieve. Perovskite oxides are also promising due to their reliability at high temperatures and stability over a large range of different operating conditions. For a generic ABO_3 perovskite material, the redox reactions that can be realized in a chemical looping process are shown below.

$$Thermal\ reduction:\ \ ABO_3 \rightarrow ABO_{3-\delta} + 1/2\ \delta\ O_2 \qquad (2.33)$$

$$Oxidation\ with\ CO_2:\ \ ABO_{3-\delta} + \delta CO_2 \rightarrow ABO_3 + \delta CO \qquad (2.34)$$

$$Oxidation\ with\ H_2O:\ \ ABO_{3-\delta} + \delta H_2O \rightarrow ABO_3 + \delta H_2 \qquad (2.35)$$

An example of perovskite material that has been widely studied is the lanthanum-manganite perovskite, with formula $LaMnO_3$. Lanthanum La is the A-site material, while manganese Mn is the B-site material. $LaMnO_3$ has already been studied for different applications, like electrodes in solid oxide fuel cells, high performance catalyst materials or metal-air batteries [27]. As $LaMnO_3$ presents low reduction extent [29], other elements, like strontium Sr, are used to partially substitute the

lanthanum. The B-site element can also be partially substituted in order to obtain better properties. For example, magnesium Mg, while not participating in the redox reactions, improves the resistance to sintering and the thermal stability. Sintering is not beneficial for reactions, as it makes powders merge into bigger solid masses. Thus, this phenomenon reduces the surface area, slowing down the reactions.

Among the various lanthanum-manganite perovskites studied by Haeussler et al. [27], the most promising one is LSMMg (lanthanum, strontium, manganese, magnesium, with formula $La_{0.5}Sr_{0.5}Mn_{0.9}Mg_{0.1}O_3$). The performance was assessed through a thermogravimetric analysis (TGA) identical to the one used to test ceria, with the following characteristics: 100 mg of perovskites, thermal reduction at 1400 °C for 45 minutes, oxidation at 1050°C for 60 min in a mixture of 50% CO_2 and 50% Ar. The carbon monoxide yield obtained is 215-217 μmol/g, more than double the amount obtained with ceria in the same conditions. Another positive aspect that was observed is the high re-oxidation yield, equal to 97%. A second experiment performed using H_2O instead of CO_2 during the oxidation step was used to estimate the H_2 yield of LSMMg. In this case, 0.8 g of perovskite material were placed in an electric tubular furnace, instead of a TGA system. The production rate of O_2 during the reduction step, and of H_2 during the oxidation step, were measured in ml per minute per g of LSMMg. Then, the total production of H_2 in μmol/g was calculated. Again, the redox cycle was performed twice, with thermal reduction at 1400°C and the oxidation step at 1050°C, with a gas mixture containing 50% of H_2O. The plot of temperature, O_2 production rate and H_2 production rate during the test is shown in figure 16 below.

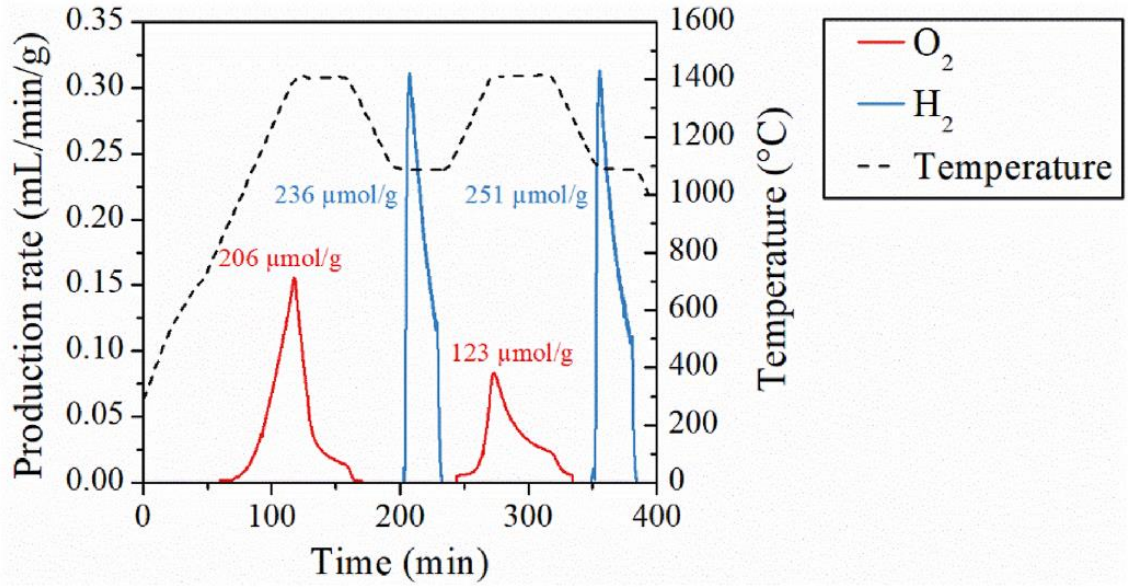

Figure 16: Temperature, O_2 and H_2 production rates of LSMMg obtained in an electric tubular furnace [29].

The total yield of hydrogen can be calculated as it is directly proportional to the integral area below the production rate curve, which is the blue curve in the figure above. This yield was similar to the total yield of carbon monoxide of the previous experiment, being 236 µmol/g in the first cycle and 251 µmol/g in the second cycle. As the two values are also similar to each other, LSMMg shows a good cycling stability during hydrogen production. In conclusion, LSMMg shows promising performances both when it is used to split CO_2 and when it is used to split H_2O.

A particular family of perovskite materials is that of the double perovskite materials, which feature a structure $A_2BB'O_6$, where A is an alkaline-earth element or a rare earth metal, and B and B' are transition metals. B can be Fe, Cr, Mn, Co or Ni, while B' can be Mo, Re or W [30]. The material discussed in this thesis is a double perovskite material called SFNM, whose formula is $Sr_2FeNi_{0.4}Mo_{0.6}O_6$. This material includes strontium Sr as the A-site element, iron Fe as B-site, molybdenum Mo and nickel Ni as B'-site elements. SFNM is obtained by doping Sr_2FeMoO_6, also known as SFMO, with nickel. SFMO has already been extensively studied for its magnetic properties [30], but similarly to other perovskite materials like LSMMg, it can also absorb and release oxygen in a chemical looping process. When SFNM is thermally or chemically reduced, it transforms from $Sr_2FeNi_{0.4}Mo_{0.6}O_6$ to $Sr_2FeNi_{0.4}Mo_{0.6}O_{6-\delta}$.

The structure of SNMO is shown in the figure below. The octahedrons are formed by FeO_6 and MoO_6, while Sr occupies interstitial spaces in body centered positions.

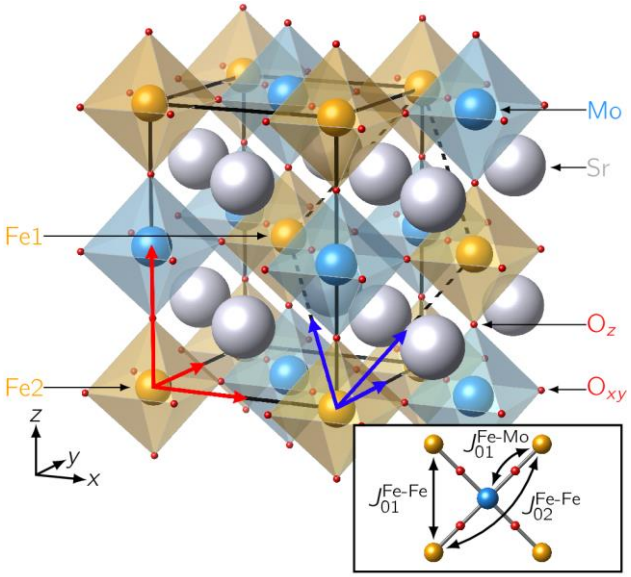

Figure 17: Structure of $SrFeMoO_6$ double perovskite [30].

The Fe and Mo atoms at the center of each octahedron form a tetragonal structure, marked by the solid black lines and the red arrows in the picture.

When nickel partially substitutes molybdenum in the structure, a phenomenon known as exsolution can be observed if the material is reduced at high temperatures [31]. In these conditions, nickel and iron come out of the perovskite structure and an alloy $FeNi_3$ is generated on the surface of the material in form of nanoparticles, according to the following equation.

$$Sr_2FeMo_{0.65}Ni_{0.35}O_{6-\delta} \rightarrow \frac{1}{2}SrFe_{0.7}Mo_{0.3}O_{3-\delta} + \frac{1}{2}Sr_3FeMoO_{7-\delta} + \frac{1}{8}Fe_{1.2}Ni_{2.8} + \frac{1}{2}O_2\ (g) \qquad (2.36)$$

In the equation, $Sr_2FeMo_{0.65}Ni_{0.35}O_{6-\delta}$ is the starting perovskite, SFNM, $SrFe_{0.7}Mo_{0.3}O_{3-\delta}$ is a new different perovskite phase and $Sr_3FeMoO_{7-\delta}$ is a new phase known as Ruddlesden-Popper (RP) phase. This phase consists of ABO_3 layers ($SrFe_{0.5}Mo_{0.5}O_{3-\delta}$) intercalated by SrO salt. The other products are $FeNi_3$, the metallic alloy, and O_2, the oxygen released by the material during the reduction. A scheme of the various solid phases of this reaction is shown in the picture below.

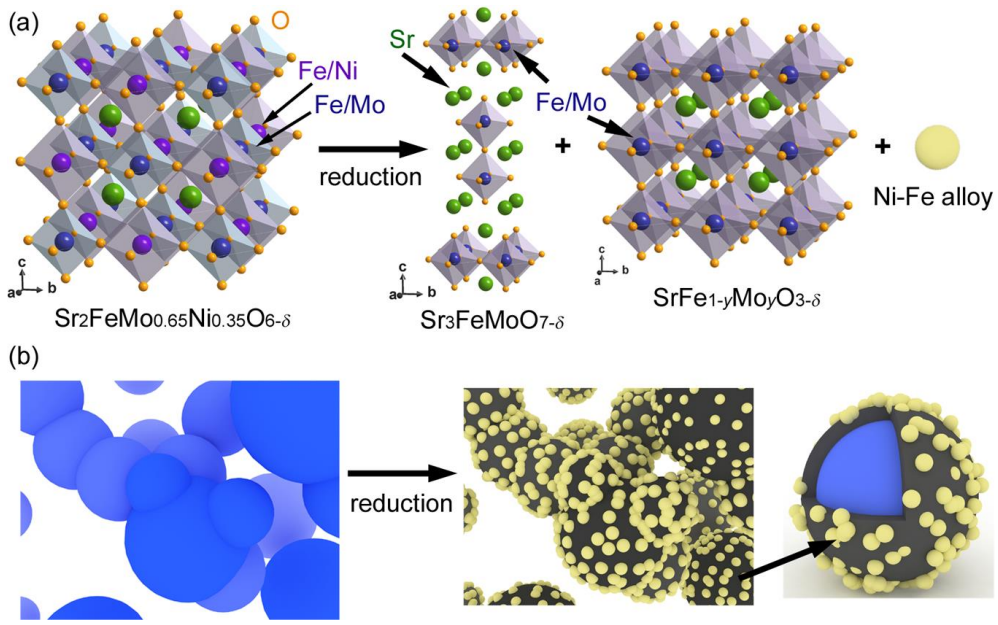

Figure 18: Scheme of the structure (a) and the surface (b) of the phases produced during the exsolution of SFNM [31].

The yellow spheres in the picture are the Fe-Ni alloy nanoparticles exsolved on the surface. As Fe and especially Ni are good catalytic materials, the exsolution phenomenon can be beneficial to the chemical looping process. In fact, during the following oxidation step, the material will not only absorb oxygen and fill the vacancies left in the structure, but also partially catalyze the splitting of H_2O and CO_2 due to the Fe-Ni alloy nanoparticles. Therefore, the resulting fuel yield should be enhanced. The extent of the benefit given by this exsolution process is not clear. Du et al. [31] observed the exsolution phenomenon after reducing SFNM for 2 hours at 850°C and using H_2 as a reducing agent. The nanoparticles of $FeNi_3$ are shown in the picture below.

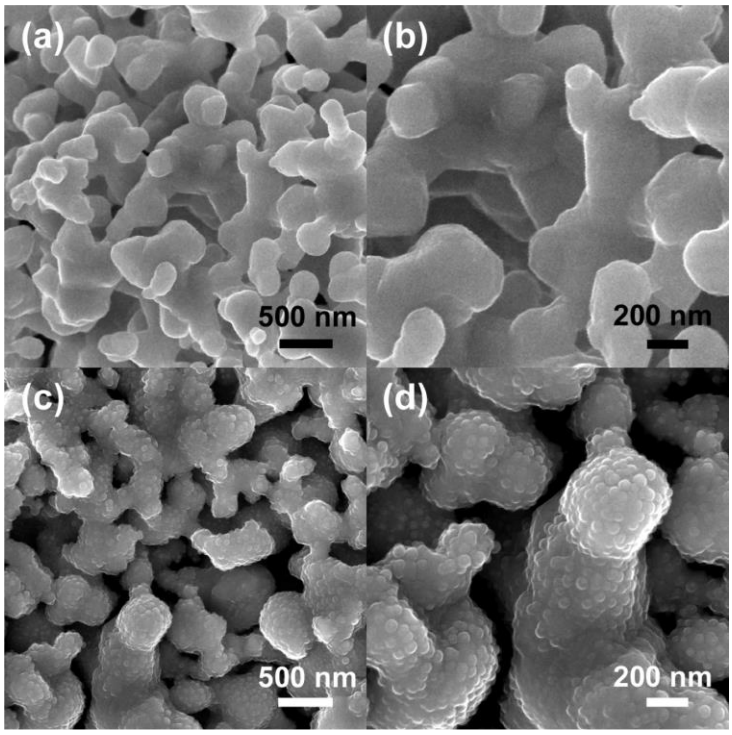

Figure 19: SEM images of Fe-Ni alloy exsolution on SFNM [31].

The pictures above were obtained with a Scanning Electron Microscope (SEM). (a) and (b) show the SFNM material as prepared, while (c) and (d) correspond to the material after the 2 hours long reduction. In (c) and (d), the exsolved nanoparticles are visible on the surface.

In conclusion, various possible oxygen carrier materials have been presented, and perovskites emerged as the most promising in terms of fuel production yield. The next section focuses on the solar concentrator and reactor systems designed to carry out the chemical looping processes.

2.4 Solar concentration systems

2.4.1 Solar concentrator types

If the heat needed for the thermochemical system is provided by the solar radiation, a solar concentration system is necessary as part of the plant. The different kinds of solar concentrators that are available are shown in figure 20 [32]. A solar concentration system is characterized by two elements: a reflector and a receiver. The first captures the solar radiation and reflects this radiation, concentrating it, to the second, whose purpose is to absorb the concentrated energy. The ratio between the energy flux on the receiver and the energy flux on the reflectors is called concentration ratio C.

The main solar concentrator types are parabolic trough (PT) collectors, linear Fresnel (LF) reflectors, central receivers (CR) and dish-engine (DE) systems [10].

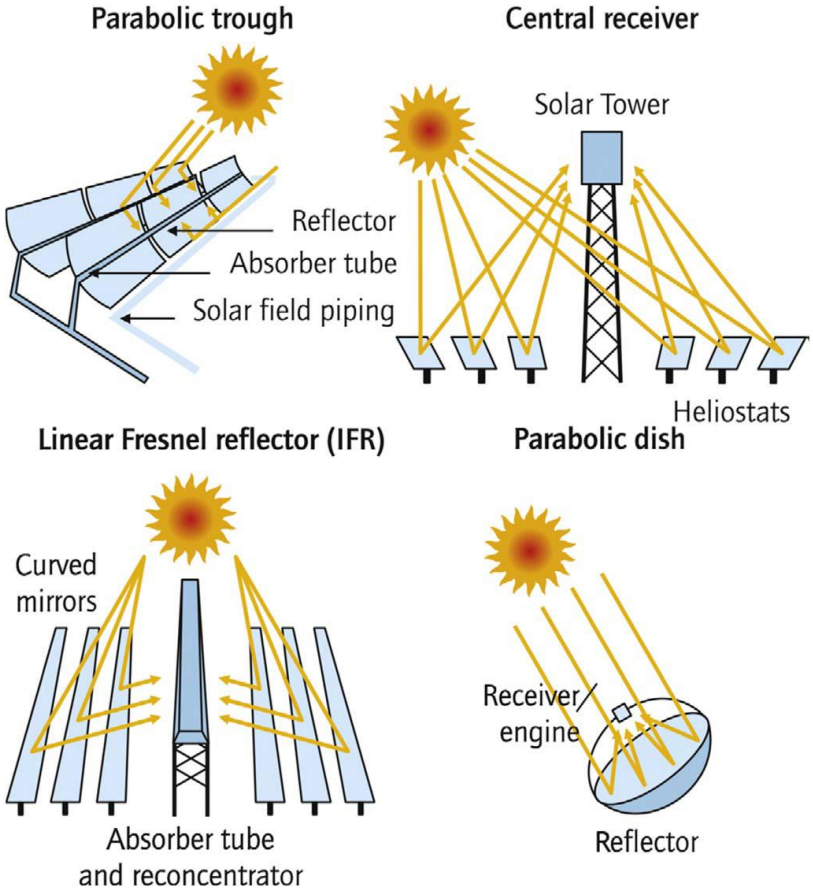

Figure 20: Solar concentration system types [32].

Parabolic trough concentrators are parabolically curved and positioned in long linear arrays. The mirrors reflect the solar radiation to a receiver pipe. As of 2018, 90% of commercial CSP (Concentrated Solar Power) plants, which produce electricity using solar heat as primary source, use parabolic trough arrays [33]. A Linear Fresnel system is similar to the parabolic trough, as it also has linear arrays of reflectors. In this case, however, the reflectors are flat and tilted by various angles. In this way, the reflectors approximate a single parabolic mirror that points at the receiver. Both parabolic trough systems and linear Fresnel systems concentrate the solar radiation along a focal line (linear concentrators). This limits the maximum theoretical concentration ratio to 210 [34]. Real concentration ratios are in the range 10-40 for LF and 15-45 for PT [35].

Unlike parabolic trough and linear Fresnel systems, Central receiver and dish-engine systems are point concentrators, characterized by a maximum concentration ratio of around 40'000. In the CR, the receiver is located on the top of a tower, and the reflectors are sun-tracking heliostats placed in the field around the tower. The dish-engine system consists in a parabolic concentrator that focuses the solar radiation on the focal point, where the receiver is located. The concentrator and the receiver move following a two-axis tracking system. As the engine is joined to the receiver, it also moves with the dish. This poses some strict limits on the size and weight of the engine. Typical solar concentration ratios of real CR and DE systems are 100-1500 and 100-1000, respectively [35].

2.4.2 Beam-down solar concentrator concept

Point concentration systems, due to their high concentration ratios, are the only ones that can be coupled with a thermochemical cycle, which require high temperatures, up to 2300 K. Due to the size limitations of the dish concentrators, central tower systems are the most studied for this application. In particular, the "beam-down" variant looks interesting, as it places the receiver-reactor at ground level, and not at the top of a tower. This approach is shown in figure 21 below. Instead of a receiver, a secondary reflector is placed on top of the tower. This type of system has two main issues. The first one is the low concentration ratio that can be obtained in the receiver region. In the concept by Yogev et al. [36], the issue is

solved by concentrating the radiation even further by using a secondary CPC (Compound Parabolic Concentrator). The CPC is positioned at ground level, directly above the receiver-reactor.

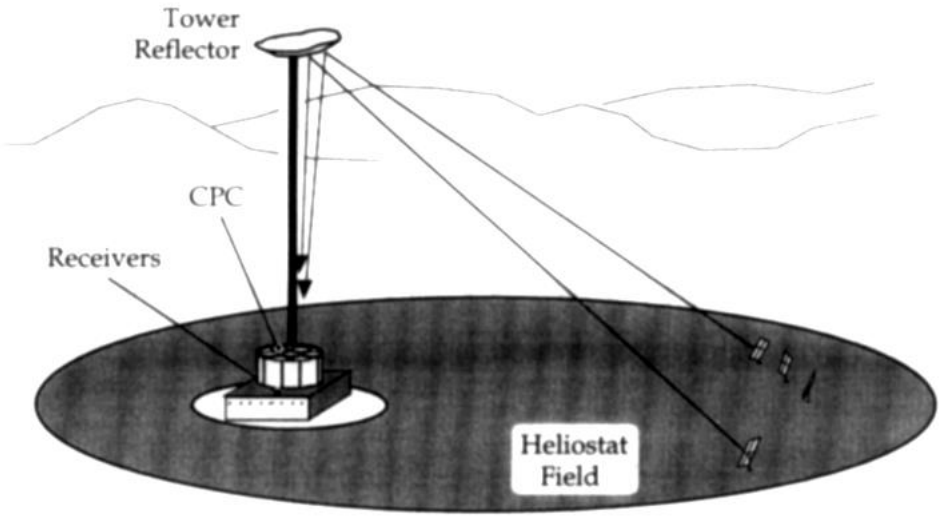

Figure 21: Beam-down solar tower concept [36].

The shape of a CPC is shown in figure 22. By placing the CPC and the receiver at ground level, and leaving just the reflector on the tower, costs are significantly reduced. The tower is light and inexpensive, long piping is not needed, and personnel does not need to frequently access the top of the tower. The second issue of the beam-down configuration is that by having the solar radiation reflected twice, by the heliostats and the tower top reflector, the reflection losses are increased. In order to minimize reflection losses, high-reflectivity coating technologies may be used on the tower reflector. These coatings are more expensive than standard mirrors, but on the other hand have reflectivity values up to 98%. As the tower reflector area is typically around 2% of the heliostat surface area, the increased expense is not significant with respect to the total plant cost.

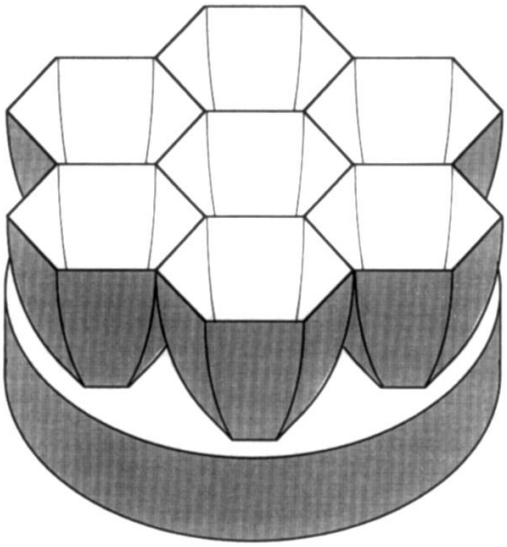

Figure 22: Compound Parabolic Concentrator [36].

2.4.3 Solar Receiver

Another important part of the solar thermal plant is the receiver, which is where the solar radiation is absorbed and converted into thermal energy. In a plant that uses the solar heat to perform a thermochemical cycle, the receiver is also a reactor. Solar receivers are subdivided in two categories: indirectly irradiated receivers (IIR) and directly irradiated receivers (DIR). The main difference between the two, shown in figure 23, is that in the indirect type the working fluid is not exposed to the concentrated solar radiation. At least one opaque layer separates the working fluid from the radiation.

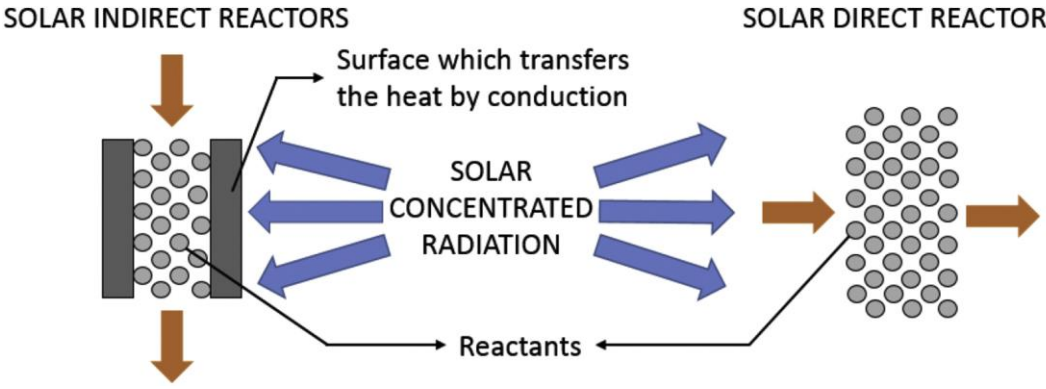

Figure 23: Solar receiver types [37].

The indirect receiver of figure 23 represents one of the possible configurations, where the radiation is absorbed by a metal wall. The wall transfers heat by conduction to the region where the reaction takes place. It is also possible to decouple the receiver and the reactor by using a heat transfer fluid (HTF). Inside the receiver, the radiation is absorbed by the HTF. Then, the fluid is transported via insulated pipes to a heat exchanger, where heat is transferred to the reactants. The concept is shown in figure 24.

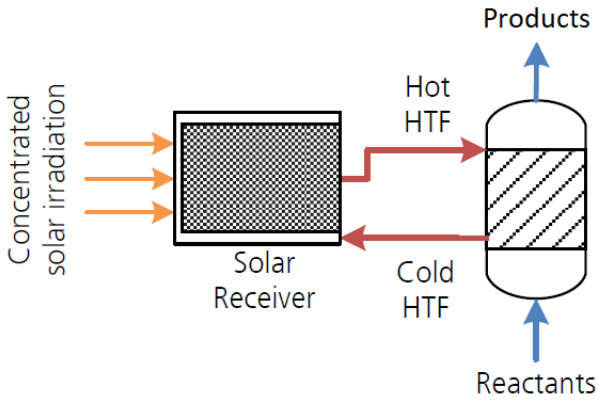

Figure 24: Indirectly irradiated reactor with heat transfer fluid. Adapted from [38].

A particular version of IIR with heat transfer fluid is the heat pipe receiver, whose working principle is shown in figure 25. A heat pipe exploits the latent heat of a fluid. The concentrated solar radiation is used to make the working fluid evaporate. The vapor is sent to the reactor, where it condenses, releasing the latent heat to the reactants. Heat pipes are considered one of the most efficient heat transfer technologies available, and are used both for cryogenic and high temperature applications.

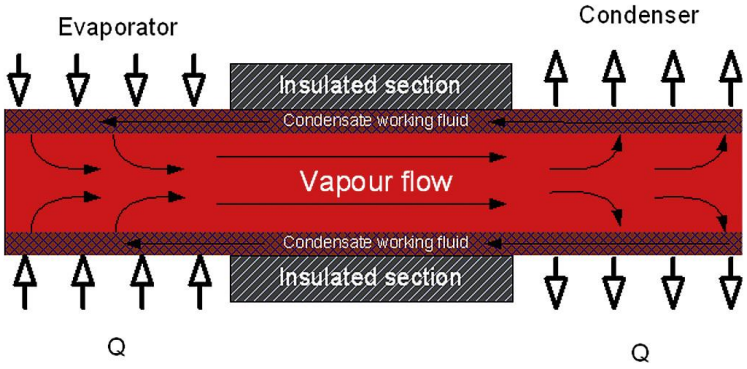

Figure 25: Working principle of a heat pipe [39].

In solar applications, an example of working fluid is sodium. At ambient pressure, sodium becomes liquid at 371 K and gaseous at 1151 K. Therefore, it can be used in a range between 873 K and 1473 K (600-1200 °C) [39]. Liao and Faghri [40] examined a heat pipe receiver with sodium as working fluid, calculating its thermal efficiency through numerical simulations. The receiver, placed on top of a tower, captures the solar radiation reflected by the heliostats and concentrates it on the heat pipe, making the sodium evaporate. The sodium vapor condenses in a tube, releasing heat to a secondary heat transfer fluid, a molten salt consisting in a mixture of 60% of $NaNO_3$ and 40% of KNO_3. The mixture is known as solar salt, and it is commonly used as thermal energy storage fluid in CSP plants. Its main advantages are the relatively low cost, the chemical safety, as it is neither toxic nor flammable, and the reasonable compatibility with stainless steel [41]. The receiver's thermal efficiency η was obtained as:

$$\eta = \frac{Q_{in} - Q_{loss}}{Q_{in}} \qquad (2.37)$$

In the equation, Q_{in} is the heat captured by the aperture of the parabolic receiver, while Q_{loss} is the sum of various energy losses, like convective, emissive, reflective and conductive losses. The efficiency that was obtained through the simulations was as high as 92.2%. Considering also an additional loss due to the spillage of solar radiation between the heliostats and the receiver, the efficiency was 88.5%. Figure 26 shows schematics of the receiver panel and the basic element containing the heat pipe.

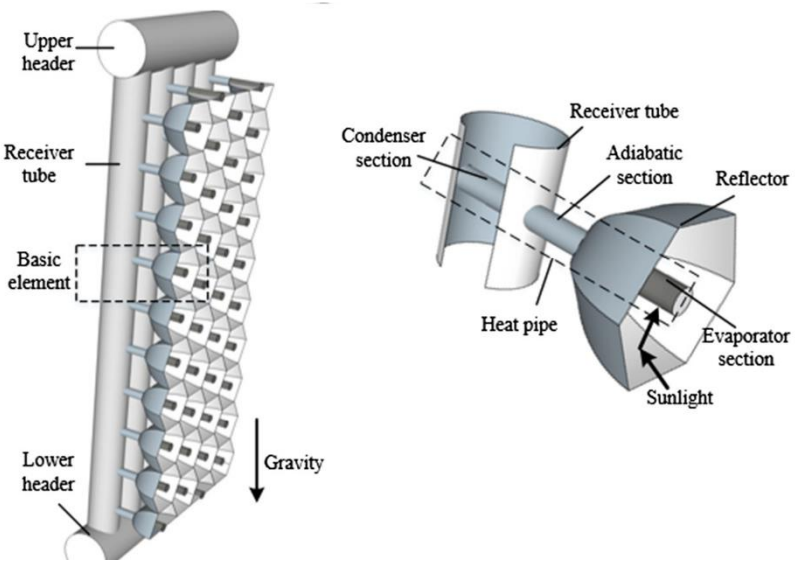

Figure 26: Schematics of a heat pipe receiver [40].

Directly irradiated receivers (DIR) use fluid streams which are exposed to solar radiation. In order to separate the fluid and the external ambient, a transparent window is used. These receivers are also known as volumetric receivers, as the solar radiation is captured by the absorber's volume. The absorber's surface has two functions, heat absorber and reaction surface. The absorber can consist in either moving particles or a stationary matrix. Stationary matrices can be crossed by the fluid stream, containing the gaseous reactants. Some of the possible designs of a stationary matrix are wire meshes, foams, honeycomb structures or pin-finned structures. Regarding the receiver design, there are two main possibilities: the external receiver, which has usually a cylindrical shape, and the cavity receiver. An example of a porous ceramic absorber, with a scheme of the cavity receiver, is shown in figure 27.

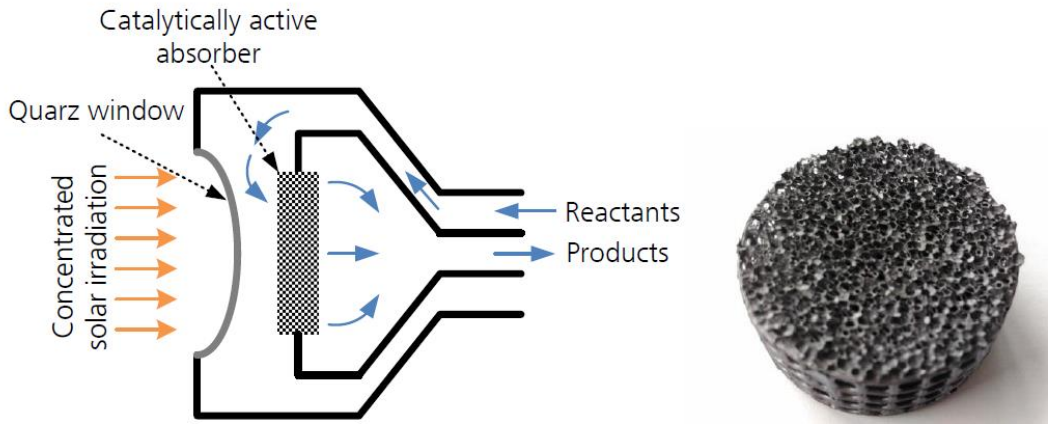

Figure 27: Directly irradiated, cavity type receiver, with ceramic absorber [42].

As the number of heat transfers is lower with respect to the indirect receivers, the DIR is potentially more efficient, and could allow higher operating temperatures in the reactor. It is therefore preferred to use a directly irradiated receiver for high levels of temperature, for example in the 1000-1500 °C range. The main drawback of using of a DIR instead of an IIR is the impossibility to employ thermal storage. Without storage, the plant's operation is limited by the intermittence of the solar radiation, while with the addition of storage, continuous and night-time operation are possible. Another disadvantage of the directly irradiated receiver, especially in the case of a cavity receiver, is the size limitation due to the quartz window. The use of a window also leads to a decrease of efficiency over time, caused by the deposition of particles.

2.4.4 Solar reactors for water and carbon dioxide splitting

After the solar radiation is concentrated and absorbed by the receiver, the heat is transferred to the reactor where the syngas production takes place. The design of the reactor has to take into account the type of receiver (directly or indirectly irradiated) and the type of oxygen carrier (volatile or non-volatile). Reactors for volatile oxygen carriers are characterized by the recombination issue: the products of the reduction, oxygen and reduced carrier, are both in gaseous phase, and could recombine to form the oxidized carrier in the reactor. Therefore, the system needs two separate reactors, one for the reduction and one for the oxidation. As the oxidation occurs at a lower temperature, it does not need to be solar-aided. So, the cycle could be decoupled, with a diurnal reduction and a nocturnal oxidation.

A rotating kiln reactor inside a cavity receiver was proposed by the ETH/PSI group. The reactor performs the thermal reduction of zinc oxide ZnO to metallic zinc, which is volatile. The reactor's configuration is shown in figure 28. A screw feeder introduces ZnO particles in the rotating reactor. The centripetal acceleration created by the kiln's rotation forces the particles against the cavity walls. The ZnO layer is exposed to the solar radiation coming from the quartz window of the cavity. A 10 kW prototype was exposed to a concentrated solar radiation, with an average concentration ratio C > 3000 and a peak level of C = 5880 [43]. All reactor's components performed well at temperatures in the range 1807-1907 K.

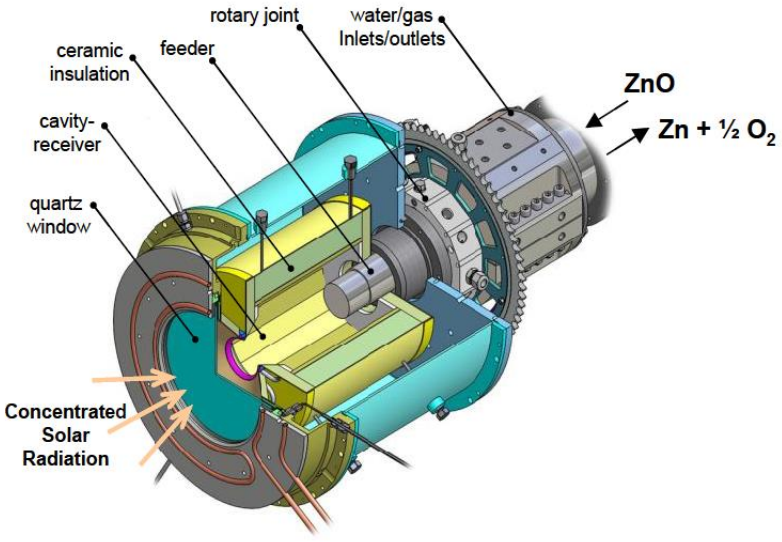

Figure 28: Schematics of a rotating kiln reactor [43].

In order to avoid recombination of gaseous Zn and oxygen, a quenching section is incorporated at the outlet of the reactor. Argon is injected into this water-cooled annular section, with the aim of making Zn condense. Figure 29 shows the quenching section, where three distinct zones can be identified. In the hot zone, the stream coming from the reactor (RF) is still at high temperature, above the ZnO decomposition temperature. In this zone, the recombination is not thermodynamically favored. In the transition zone, the temperature is lower than the ZnO decomposition temperature but still higher than the Zn saturation temperature. Therefore, Zn starts recombining with O_2, and ZnO can form on surfaces. In the cold zone, where the quenching flow (QF) of argon is introduced, the temperature decreases below the Zn saturation temperature. Zinc condenses first, and later solidifies.

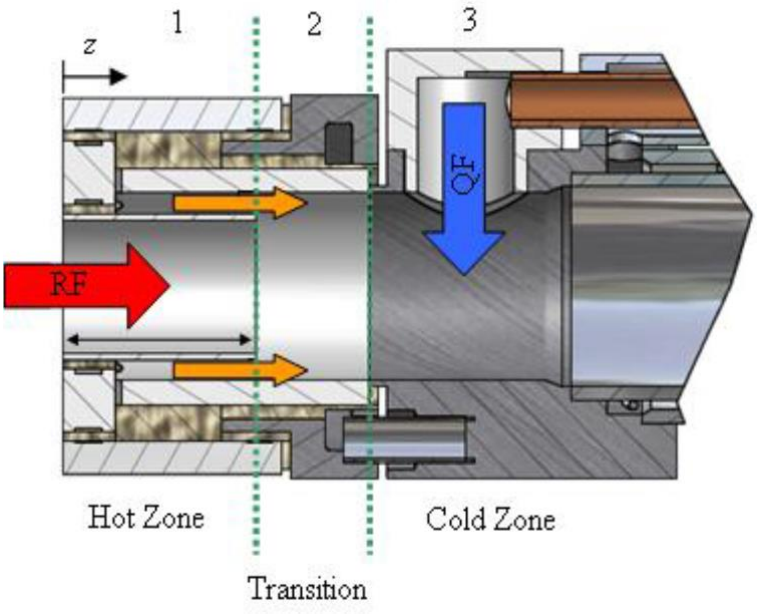

Figure 29: Quenching section of the Zn/ZnO reactor [43].

By increasing the Ar/Zn(g) dilution ratio, the zinc content in the downstream particles stream, which consists of Zn and ZnO, increases. With dilutions in the range 170-1500, the purity of the zinc obtained increased from 40% to 94% [44].
The concept of a rotating kiln was also tested by a pilot scale 100 kW_{th} plant built by PROMES in Odeillo, France. During the testing runs, the mean concentration ratios obtained were in the range 3600-4400, and the mean cavity temperatures were in the range 1770-1920 K [45]. The zinc concentration in the Zn/ZnO mixture was

once again dependent on the argon dilution during the quenching phase, increasing from 12% to 49%.

An example of indirectly irradiated aerosol reactor for ZnO dissociation was designed by the University of Colorado [46]. The reactor is cylindrical and consists in an irradiated graphite tube, which reaches high temperatures and releases heat by re-radiation. The re-radiated heat is absorbed by the alumina tubular reactor, where ZnO particles, entrained in an argon stream, are introduced. Their reactor was electrically heated, but the concept of a tubular reactor inside a cavity can be extended to a solar heated reactor. A possible configuration is shown in figure 30.

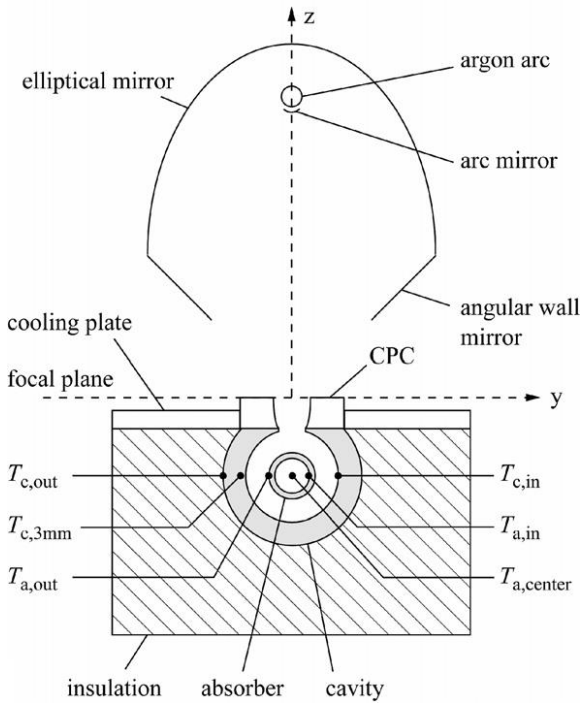

Figure 30: Indirectly irradiated, cavity-type reactor [47].

The cavity and the absorber are both ceramic. The cavity is a cylinder made of yttria-stabilized zirconia (10% yttria YO_2 in zirconia ZrO_2) covered in alumina Al_2O_3 for insulation. The tubular absorber is also made of alumina. ZnO plates are placed inside the absorber tube, and the products, Zn(g) and O_2, are transferred to the quenching section by an argon flow. The University of Colorado, in collaboration with ETH/PSI, made numerical simulations and validated them with a 5 kW prototype. The experiments confirmed the reaction rates obtained through the simulations for the 1780-1975 K temperature range. The simulations also

identified a maximum solar to chemical efficiency equal to 28.5% at a reactor temperature of 2300 K [47].

If instead of ZnO, a non-volatile oxygen carrier is used, the reactor's design has to be changed, as the reduced form of the oxygen carrier is still solid. A consortium of U.S. researchers from SNL, Bucknell University and Arizona State University proposed a directly irradiated, moving packed bed reactor, shown in figure 31 below. The concentrated solar radiation comes from the window-covered aperture on the top. The solar heat is absorbed by the particles of oxygen carrier, in this case ceria CeO_2, which are transported to the top of the tower by a vertical screw elevator. The vertical screw is stationary, while the elevator casing rotates, making the CeO_2 particles move up as a result. The thermal reduction (TR) occurs, and oxygen is pumped away from the chamber. The reduced particles of ceria fall into the connecting tube, which also functions as a counterflow heat recuperator. In fact, the oxidized particles moving up through the screw elevator are pre-heated by the hot reduced particles moving down inside the connecting pipe. The reduced ceria particles are then transferred to the fuel production (FP) chamber, where they react with H_2O and CO_2, producing syngas.

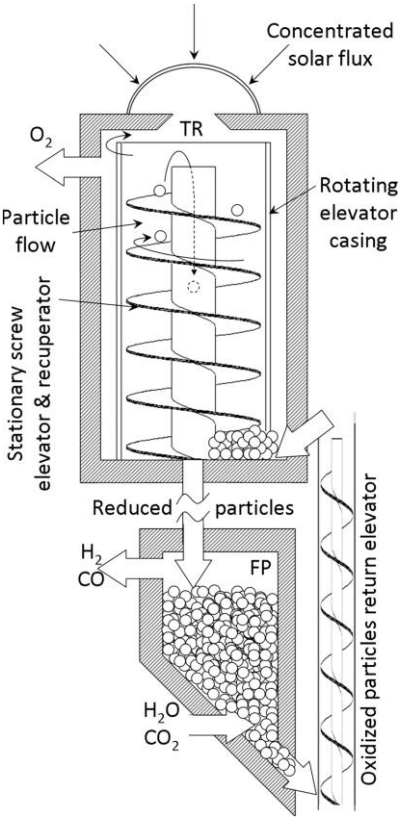

Figure 31: Directly irradiated, moving packed bed reactor [48].

The reported efficiencies of the solar energy to H_2 and CO conversion, calculated through simulations, are above 30% [48]. This efficiency is widely dependent on two factors: the effectiveness of the heat recuperator and the partial pressure of O_2 inside the thermal reduction chamber. The lower the partial pressure of oxygen pO_2, the higher the non-stoichiometry δ will be, and the efficiency will be higher as a result. The value of pO_2 can be decreased by either using a vacuum pump or an inert sweep gas like nitrogen or argon.

A second possible design of directly irradiated reactor include the cavity receiver with ceramic absorber made in a honeycomb or foam shape. The HYDROSOL research group studied the honeycomb reactor concept at large scales, up to a 100 kW pilot plant [49] and a 1 MW plant concept [50]. In order to ensure a continuous operation, the 100 kW plant employs two reaction chambers. When one chamber operates at 1200°C performing the thermal reduction of the iron oxides inside, in the other one the temperature is kept at 800°C to oxidize the iron oxides and produce hydrogen from water. Every 20-30 min, the temperatures of the two chambers are changed by shifting the focus of the heliostats, and at the same time the feed gas changes accordingly: inert N_2 for the reduction, H_2O for the oxidation. A schematic of the two chambers and the gas ducts for the feed and outlet gases is shown below.

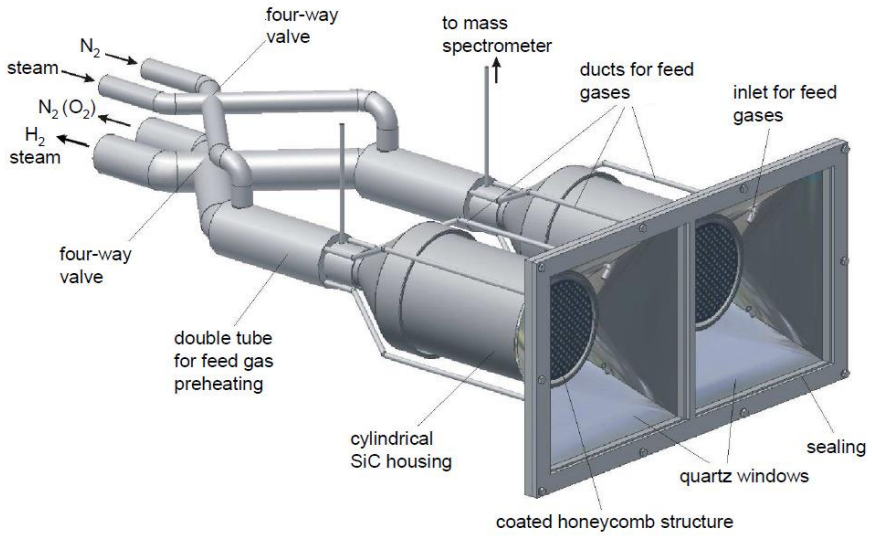

Figure 32: Directly irradiated cavity reactor with honeycomb shape [51].

Finally, a directly irradiated reactor for a non-volatile material can be realized with two chambers and a cylindrical rotor which transfers the solid particles between them. Unlike the honeycomb reactor described above, this rotary-type reactor concept contains moving parts. This design was first introduced in 2006 by a research group from the University of Tokyo [52]. In their design, the rotor is covered by reactive ceramics, like ceria (CeO_2) and ferrites ($Ni_{0.5}Mn_{0.5}Fe_2O_4$). During the movement of the rotor, these reactive ceramics are exposed alternatively to the concentrated radiation in the O_2 release cell, and to the steam flow in the H_2 generation cell. The tests showed that H_2 could be produced with a reduction temperature of 1623 K and an oxidation temperature of 1273 K for ceria. With the ferrites, the water splitting was obtained at lower temperatures, 1473 K for the reduction and 1173 K for the oxidation.

A possible improvement of the concept was studied by the University of Minnesota [53]. In order to increase the efficiency of the process, a heat recovery system is introduced. Figure 33 shows a schematic of the reactor. The heat recovery is obtained by using a secondary cylindrical rotor inside the one which transports the reactant. The second cylinder is concentric and counter-rotating with respect to the first. While the outer cylinder is made of porous reactive ceria, the inner one is made of an inert ceramic material, like zirconia or alumina. Firstly, CeO_2 reaches the reduction zone, where it is exposed to the concentrated solar radiation inside the receiver cavity. The thermal reduction happens here, producing O_2 which is swept away by the inert gas. When the reduced ceria, $CeO_{2-\delta}$, leaves the reduction zone, it moves inside the pre-cooling zone, where it releases heat through radiative transfer to the inner cylinder, which is colder due to the counterflow movement. Then, the reduced ceria arrives in the oxidation zone, where it reacts with H_2O and/or CO_2 and produces fuel. Finally, the now oxidized ceria enters the pre-heating zone, where it receives heat from the inner cylinder which is rotating out of the hot reduction zone.

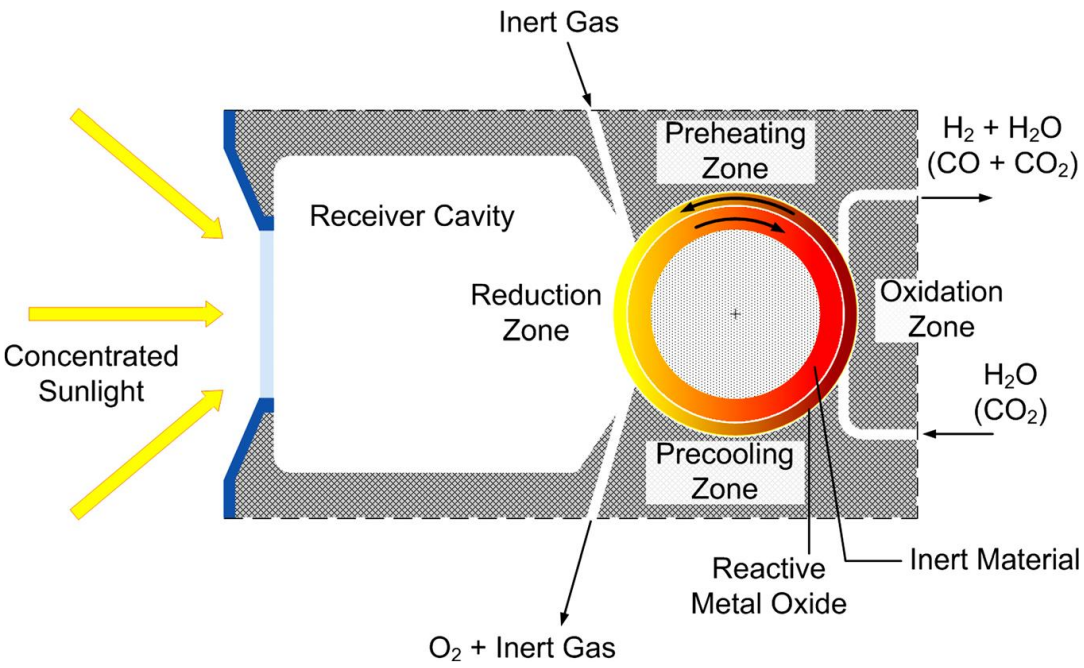

Figure 33: Directly irradiated, rotary-type reactor [53].

The numerical simulations show that the heat recovery effectiveness of this system can be higher than 50%, when using thin cylinders and long rotation periods.

The following section illustrates a variety of tests performed at the CO_2 Circle Laboratory (CCL), inside the Environment Park in Turin. The tests aim at estimating the carbon monoxide yield of the SFNM material, and the influence of various different parameters on this yield.

3. Experimental tests

3.1 Microreactor setup

The CO_2 Circle Lab in the Environment Park is equipped with a microreactor test bench. Most of the tests carried out on possible oxygen carrier materials which can be found in literature are thermogravimetric analyses (TGA). With respect to TGA, the reactor at the CCL is closer, in terms of structure, to a large-scale system, and higher values of sample masses and gas flow rates can be tested. The experimental system consists of three main components: a group of mass flow controllers and valves that are used to control the mass flow rates of different gases and set a specific atmosphere inside the reactor, a furnace that contains the reactor and keeps it at the desired temperature, and a gas analyzer system which is used to obtain the results. A major difference between the experimental tests described below and the TGA tests from other authors presented in the previous sections is that the reduction phase in the reactor is obtained by making the sample material react with hydrogen. The presence of H_2 aids the reduction, making it possible at lower temperatures with respect to a thermal reduction with an inert sweep gas.

3.1.1 Reactor and furnace

The reactor used for the tests is shown in figure 34. It consists in a horizontal alumina tube, with an internal diameter of 32 mm, placed inside an electrically heated furnace. The reaction zone, in which a uniform temperature distribution can be ensured, and where the sample is positioned, is 1 m long. The heating elements, made in molybdenum disilicate $MoSi_2$, can raise the temperature of the reaction zone up to about 1800°C [54]. These heating elements are hanging vertically around the work tube. A ceramic fiber insulation, with its low thermal conductivity, minimizes the heat losses and ensures high possible heating rates.

Figure 34: High temperature horizontal tube furnace.

The furnace is controlled by an external power conditioning unit, shown in figure 35, which supplies electricity to the $MoSi_2$ resistances. The power conditioning unit is also connected to a computer, through which the furnace can be controlled, either manually or by setting a program. A program is composed of multiple successive steps, which can be at constant temperature (isothermal) or temperature ramps (either heating ramps or cooling ramps), that are performed automatically.

Figure 35: Power conditioning unit for the furnace.

3.1.2 Mass flow controllers (MFC)

The function of a mass flow controller is to send a specific flow rate of a certain gas into the reactor. Seven different gases, coming from the laboratory's gas lines, can be mixed and sent to the work tube. There is one MFC for each of these seven gases. The first two MFCs are used for two different argon mixtures, while the other five are for hydrogen H_2, methane CH_4, nitrogen N_2, carbon monoxide CO, and carbon dioxide CO_2. During the tests described in the following sections, three of these gases are used: H_2 for the SFNM reduction, CO_2 for the SFNM oxidation and N_2 as inert gas and diluent. The laboratory's gas lines provide pressurized gases, but as the reactor is used at ambient pressure, the MFCs reduce the pressure down to a value slightly higher than the atmospheric level, in order to compensate the losses downstream.

Between the MFCs and the reactor, two valves are present. The first one allows to add water vapor to the stream, by setting it on "WET". The experimental tests presented here did not use water, so this valve was always set on "DRY". With the second valve it is possible to bypass the reactor and sent the gas stream directly into the exhaust pipe under the hood. It can be useful to set the valve on "BYPASS" when making preliminary calibrations on the instruments. For the duration of the tests on the sample, this valve has to be set on "FURNACE".

Similarly to the furnace, both the valves and the mass flow controllers are operated through a software. The software makes manual and automatic operations available. Like the furnace's software, the automatic mode can follow a sequence of steps implemented by the user. For each step, the flow rates in Nml/min of the seven gases, the positions of the two valves and the duration in seconds have to be specified. The software's interface is shown in figure 36. The mass flow controllers, each one with its own set point and measured flow, can be seen on the interface, as well as the position of the two valves.

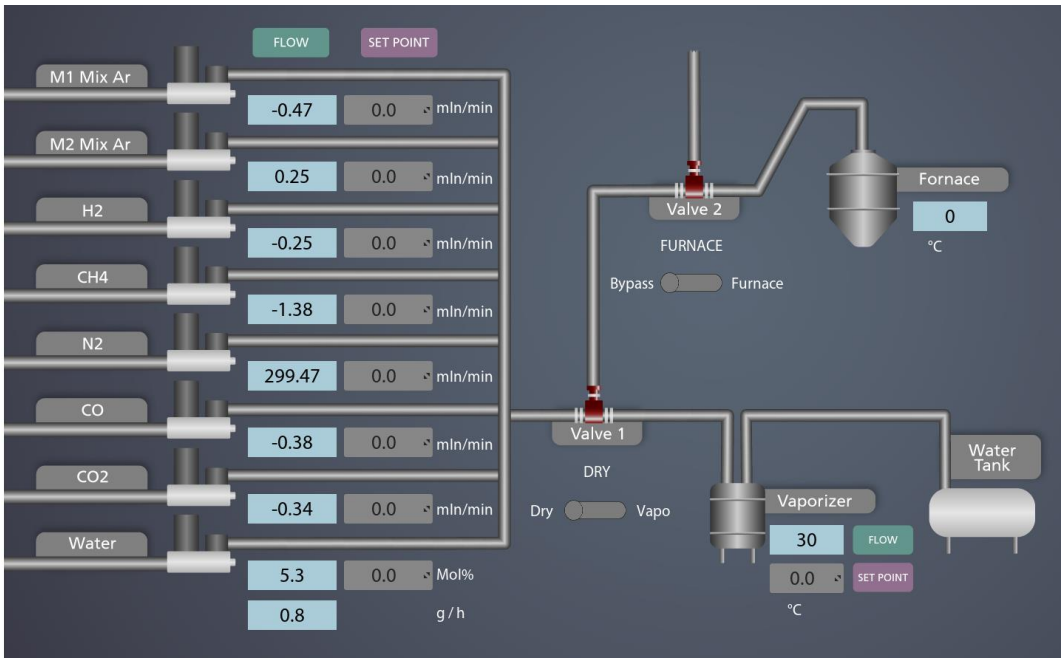

Figure 36: Software interface to control the valves and MFCs of the test bench.

3.1.3 Gas analyzer

The results of the reactions occurring inside the furnace are investigated by using a gas analyzer (Emerson X-Stream Enhanced XEGP) placed downstream of the reactor. The analyzer continuously measures the concentration of various gases in a stream and stores the concentration values obtained each second. The gas analyzer needs a dry stream to work properly, so the moisture present in the flow must be separated by condensation before entering the instrument. Other gases, like hydrogen, carbon monoxide or carbon dioxide, can be detected by the instrument, using different gas analyzing principles for every specific gas. CO and CO_2 concentrations are obtained through infrared (IR) analysis, while H_2 is measured by a thermal conductivity detector (TCD).

IR gas analysis measures the amount of infrared radiation absorbed by the gas flow. As different gases absorb different frequencies, it is possible to identify a specific gas in the stream. In addition, the amount of absorbed light, the absorbance, is proportional to the gas concentration, according to the Beer-Lambert law [55].

$$A = log_{10}\left(\frac{I_0}{I}\right) = \epsilon \cdot l \cdot c \qquad (3.1)$$

In the formula, A is the absorbance, which is equal to the base-10 logarithm of the ratio between the initial intensity of the radiation emitted by the instrument, I_0, and the intensity of the radiation collected after it passed through the gas, I. The other parameters are ϵ, the molar absorptivity, which is characteristic of a specific gas, and can be measured in $L/(mol \cdot cm)$, l, the length of the ligth path in cm, and the concentration c in mol/L. By measuring the absorbance, the concentration can be calculated and displayed by the instrument. A schematic of the IR gas analyzer is shown in figure 37 below.

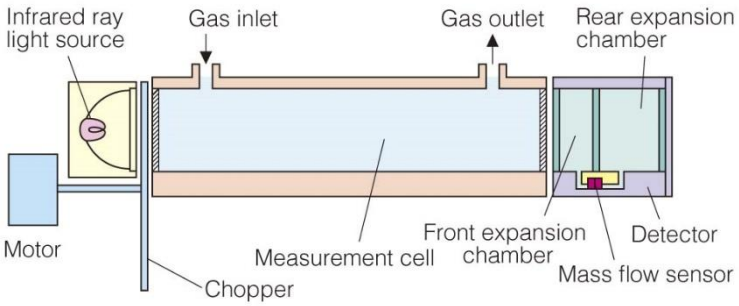

Figure 37: Schematic of an IR gas analyzer [56].

The infrared light emitted by the source is partially absorbed by the gas flow in the measurement cell. The temperature of the gas increases due to the absorption, and this leads to an increase of volume. The gas expands and occupies the expansion chamber. The chopper is used to stop the radiation from reaching the gas, reducing the temperature and creating a temperature difference between the two sides of the mass flow sensor in the expansion chamber. The absolute flow measured by the sensor is proportional to the amount of light that was absorbed when the chopper was open. So, the measured value is proportional to the gas concentration [57].

The thermal conductivity detector (TCD) used to measure the hydrogen concentration exploits the significant difference in thermal conductivity between hydrogen and most other gases. Table 1 shows the values of thermal conductivity in $mW/(cm \cdot K)$ for various different gases, including H_2, at 50°C.

Gas	Thermal conductivity [mW/(cm K)]
Hydrogen (H_2)	1910
Oxygen (O_2)	283
Nitrogen (N_2)	277
Carbon monoxide (CO)	267
Carbon dioxide (CO_2)	184

Table 1: Thermal conductivity of different gases at 50°C [57].

As the conductivity of hydrogen is one order of magnitude higher than that of the other gases, it is possible to identify H_2 in a gas flow easily. The gas analyzer uses a Wheatstone bridge with four temperature sensitive resistors, shown in figure 38. One of the R_S resistors is located in the sample gas flow, while one of the R_R resistors is surrounded by a reference gas. U_{Br}, the output signal of the bridge, is adjusted to zero when there is no gas flowing in the instrument. When the bridge is exposed to a stream, the gas absorbs heat from the resistors. The amount of heat that is exchanged depends on the conductivity of the gas. A gas with high conductivity will absorb more heat, resulting in a lower temperature of the resistor.

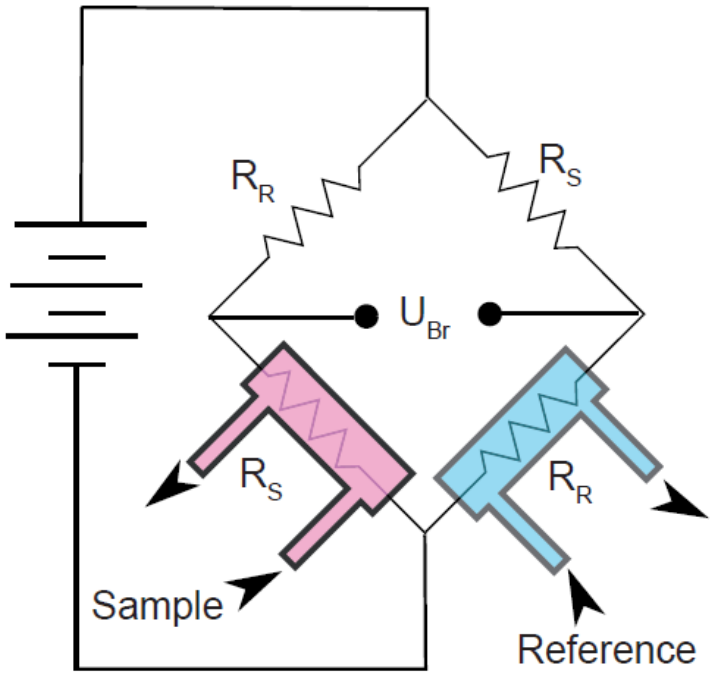

Figure 38: Wheatstone bridge for TCD measurement [57].

As already mentioned, the resistors are temperature sensitive, so a variation of temperature causes a variation of resistance, and this in turn causes a variation of the output signal U_{Br}. If a reference gas is supplied on the other side of the bridge, the output signal will be proportional to the difference in conductivities between the sample and the reference gases. From this conductivity difference, the concentration of hydrogen in the stream can be calculated.

3.2 Description of the experimental tests

3.2.1 Definition of constant parameters

A first group of seven tests on SFNM was carried out on the reactor setup previously described. The aim of these tests is to determine the effect of different parameters on the carbon monoxide production rate and on the carbon monoxide yield of the sample. These parameters are the total flow rate of the reacting gas, the mass of the sample and the reactor configuration. All of the other parameters, like temperature, reacting gas concentrations and duration of the reduction and oxidation phases were kept constant among the various tests. The values of these common parameters are shown in table 2 below.

Reduction temperature [°C]	850
H_2 concentration during reduction [%]	10
Reduction phase duration [min]	30
Reduction total flow rate [Nml/min]	200
Oxidation Temperature [°C]	850
CO_2 concentration during oxidation [%]	20
Oxidation phase duration [min]	15

Table 2: Common parameters in all tests.

The flow rate in Nml/min during the reduction phase is kept constant, while the flow rate during the oxidation phase is changed between different cycles. During each test, a certain mass of the sample is placed inside the reactor. Then, a program of reduction and oxidation cycles is implemented in the software that controls the

MFCs, with different oxidation flow rates. The furnace is also programmed to raise the temperature up to 850°C and keep the temperature constant for the whole duration of the test. When the MFCs and furnace programs are started, the gas analyzer is also activated, so that it continuously stores the concentrations of H_2, CO and CO_2. After the tests, the concentration data are collected and elaborated.

3.2.2 Data processing

The objective of the elaboration in to calculate the CO production rate peak in $\mu mol/(g \cdot s)$ and the the CO yield in $\mu mol/g$. An example of the data before the post-processing, relative to the first test, is shown in the diagram below.

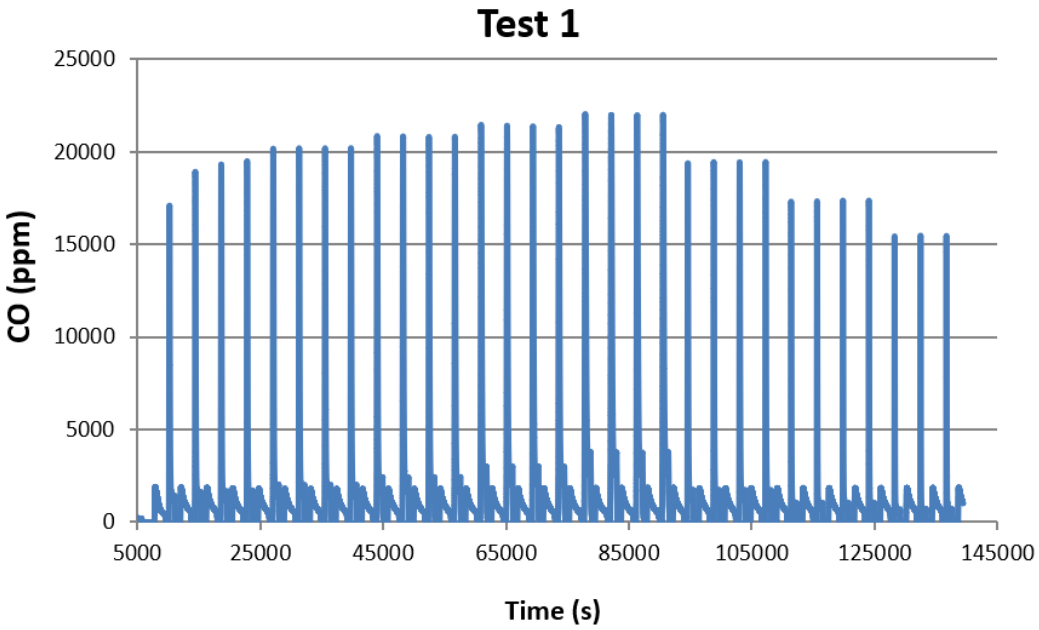

Figure 39: CO concentration plot for the first test.

The carbon monoxide content is expressed in parts per million (ppm). The range 0-25000 corresponds to 0-2.5 %. CO appears in peaks, one for each oxidation phase. In the processing phase, each peak is isolated and converted through the following steps. Firstly, the volume flow rate of CO in Nml/s is calculated.

$$\dot{V}_{CO}\left[\frac{Nml}{s}\right] = \frac{CO\ [ppm] \cdot 10^{-6}\ [1/ppm]\ \cdot\ \dot{V}_{ox}\ [Nml/min]}{60\ [s/min]} \qquad (3.2)$$

$\dot{V}_{ox}$ corresponds to the total flow rate during oxidation, set by the mass flow controllers according to the program. Now $\dot{V}_{CO}$ can be converted into the specific production rate.

$$CO\ rate\ \left[\frac{\mu mol_{CO}}{g_{SFNM}}\right] = \frac{\dot{V}_{CO}\ [Nml/s] \cdot 10^{-3}\ [Nl/Nml] \cdot 10^{6}\ [\mu mol/mol]}{22.414\ [Nl/mol] \cdot m_{SFNM}\ [g]} \quad (3.3)$$

In the formula, m_{SFNM} is the initial sample mass inside the reactor. It is constant during a single test, but it varies among different tests. Figure 40 shows the plot of the first peak among those of figure 39, converted in specific production rate.

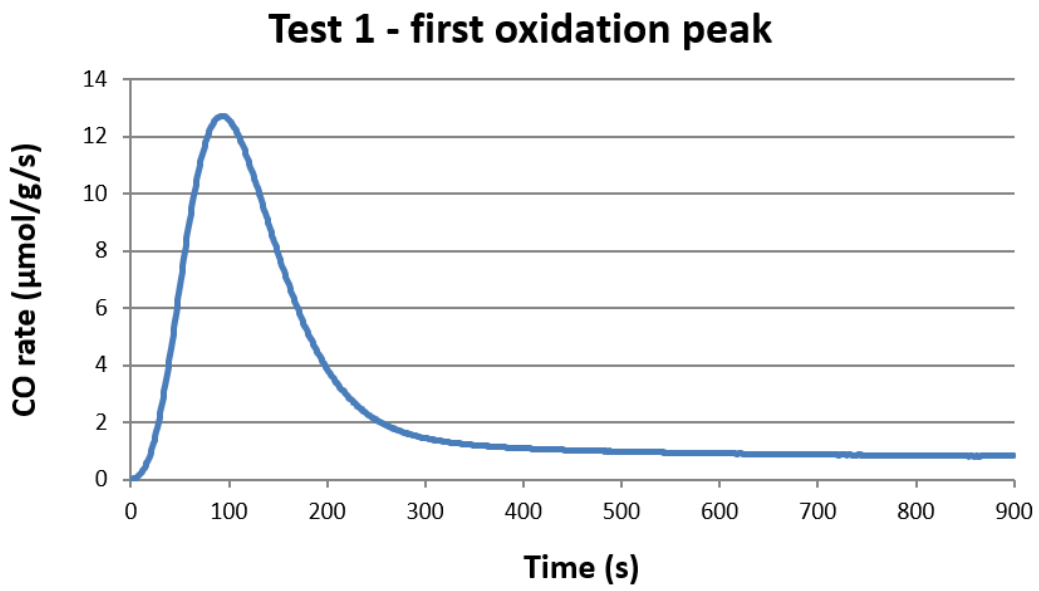

Figure 40: Specific production rate of CO during the first oxidation of the first test.

As shown in the plot, the oxidation phase lasts 15 minutes (900 seconds). The amount of carbon monoxide detected by the gas analyzer starts from zero, then increases as the oxygen carrier material absorbs O from CO_2. As the oxygen vacancies of the material are occupied, the production of CO decreases, finally stabilizing at a constant value different from zero. In order to estimate the total amount of CO produced during the oxidation, this tail has to be cut off, as it causes an overestimation of the yield. An instant of time considered to be the end of the peak has to be chosen. In this work, the peak is deemed as ended when the relative change $\Delta y(t)/y(t)$, with y being the production rate, is below an arbitrary tolerance value fixed here at 0.005 (0.05%). After the instant t_{end} that fulfills the condition

is identified, a straight line between the origin and y(t_{end}) is plotted. The difference between the measured production rate curve and the straight line is the final corrected peak used to estimate the CO yield.

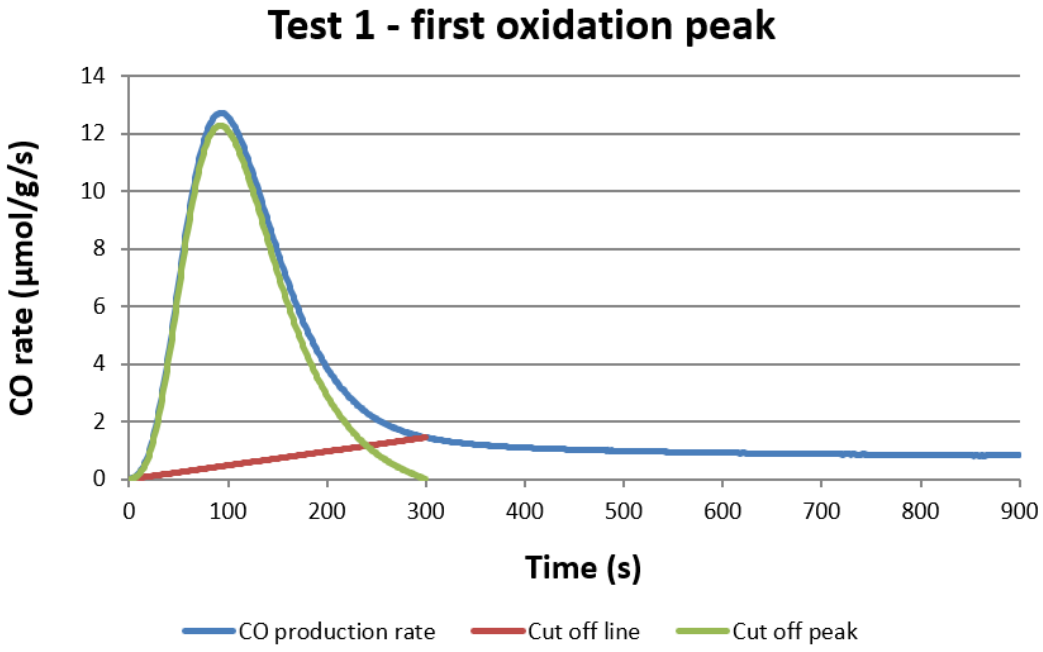

Figure 41: Specific CO production rate peak, before and after the cut off.

The green line, corresponding to the corrected peak, approximates the real peak, but it goes to zero after about 300 s. The CO yield can finally be calculated as the integral area below this green line, which is approximated as follows.

$$CO\ yield\ \left[\frac{\mu mol_{CO}}{g_{SFNM}}\right] = \int_0^{t_{end}} y_{peak,cut}(t)\ dt \approx \sum_{i=0}^{n_{end}} \left(y_{peak,cut}(t_i) \cdot \Delta t\right) \qquad (3.4)$$

In the approximation, the time period between 0 and t_{end} is represented by a number n_{end} of equally spaced intervals. The gas analyzer provides one value of concentration per second, therefore Δt is the same for every interval and equal to 1 s. So, the yield is finally calculated as the summation of the values of the peak curve after the cut off.

$$CO\ yield\ \left[\frac{\mu mol_{CO}}{g_{SFNM}}\right] \approx \sum_{i=0}^{n_{end}} y_{peak,cut}(t_i) \qquad (3.5)$$

3.2.3 Reactor configurations

Two different configurations of the reactor are compared in the laboratory tests. The simplest one is the alumina crucible configuration. The sample material is laid on a small alumina container, which is then positioned inside the reactor zone. This reactor setup allows to use higher sample masses, with respect to a thermogravimetric analysis. The connection between the reactor and the gas analyzer is realized with a flange that is tightened around the alumina pipe with screws to avoid gas leaks. Figure 42 below shows the main elements of this configuration, with the crucible filled with the perovskite material on the left and the flange on the right.

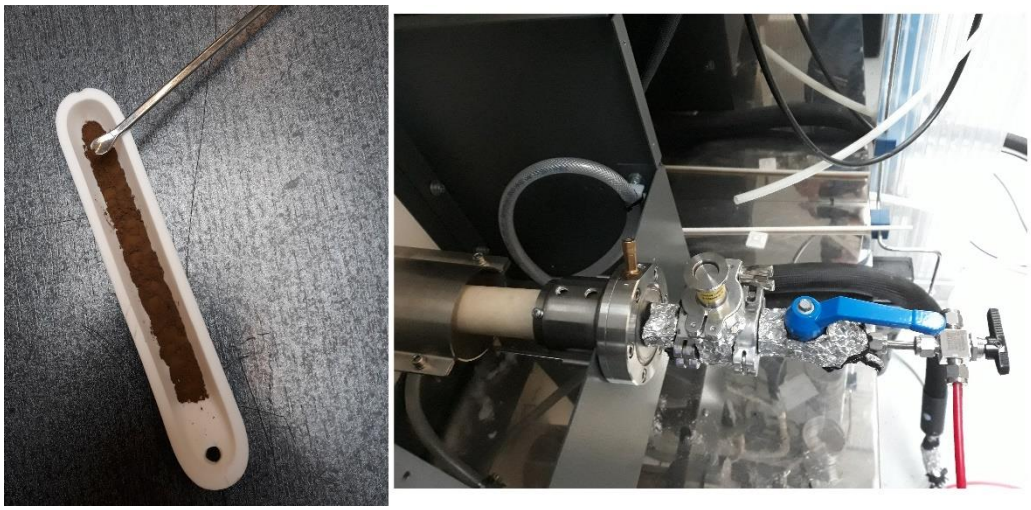

Figure 42: Reactor configuration with alumina crucible.

The second reactor configuration is the tube in tube. In this case, inside the bigger alumina tube with a 32 mm internal diameter, a smaller tube, also made in alumina and with a diameter of 8 mm, is placed. The sample is positioned in the inner tube, dispersed in a quartz wool matrix. The gas can flow through the matrix and react with the particles of sample material. More quartz wool is used to keep the inner tube in place. The tube in tube configuration does not need the flange for the connection with the gas analyzer, because the inner tube can be joined with gas tight threaded connectors to the pipe that leads to the analyzer, which is the red pipe in figures 42 and 43.

Figure 43: Reactor setup with tube in tube.

The tube-in-tube configuration cannot be used for high values of sample mass. On the other hand, it ensures that the whole sample, dispersed in the quartz wool matrix, is continuously exposed to the gas flow, unlike the alumina crucible, where only the upper surface is exposed to the stream. The higher surface-to-volume ratio of the sample particles in the tube-in-tube should result in higher CO yields for the second configuration.

3.2.4 Definition of the test-specific parameters

In this section, the seven experimental tests carried out on SFNM in the reactor are presented. The first tests, from Test 1 to Test 5, were performed in the alumina crucible configuration, while the others were realized with the tube-in-tube setup. Each test exposes the sample to 9 different values of oxidation flow rate in the range between 100 and 625 Nml/min, and each of these flow rate values is used in 4 consecutive identical cycles, for a total of 36 reduction-oxidation cycles. The cycles are reiterated four times identically in order to have a validation of the measurement

and ensure the repeatability of the results. Table 4 below is a summary of the reactor tests.

Test number	Setup	Sample mass (mg)
1	Crucible	200
2	Crucible	50.0
3	Crucible	20.7
4	Crucible	10.0
5	Crucible	5.0
6	Tube-in-tube	4.6
7	Tube-in-tube	1.3

Table 3: Summary of the reactor tests.

4. Discussion of the experimental results

4.1 Influence of flow rate on CO production

In this section, the results of a single test, with different oxidation mass flow rates between cycles, are presented. Figure 44 below is a plot relative to Test 2. In particular, the plot shows the average CO production peaks for each flow rate value, after the correction. Each peak is the average of the four cycles carried out with the same oxidation flow rate. The nine oxidation flow rate values in Nml/min used in test 2 are: 100, 125, 156, 175, 200, 300, 400, 500 and 625.

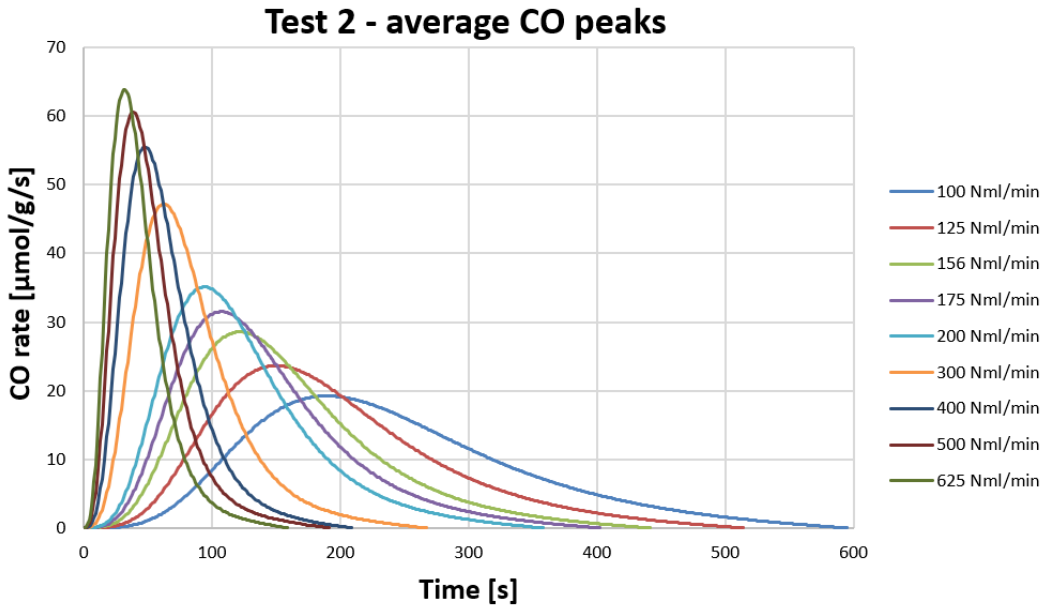

Figure 44: Average CO production peaks of test 2.

The production rate peaks become taller and narrower with increasing flow rate, meaning that at higher flow rates the reaction tends to become faster and goes to completion after a shorter period of time. The gap between one flow rate and the next in the plot is smaller for the lower flow rates. For example, the difference between the first and the second flow rates is 25 Nml/min, while the difference between the last and the penultimate values is 125 Nml/min. Therefore, it can be said that the peaks tend to become more similar at high flow rates, possibly tending towards a constant shape.

The average specific yields as a function of the flow rate for Test 2 are shown in the plot below.

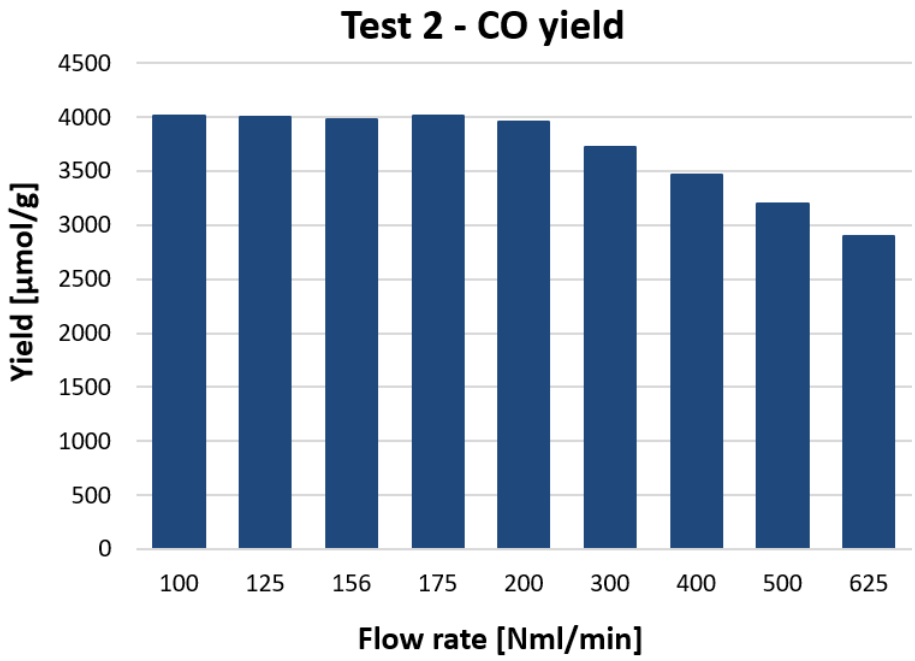

Figure 45: CO yield results from test 2.

Even though the peaks at higher flow rates are taller, their subtended area is smaller, leading to a yield that decreases with increasing flow rate. The yields are between a minimum of about 2800 µmol/g at 625 Nml/min and a maximum of about 4000 µmol/g at 100 Nml/min. These values are one or two orders of magnitude higher than those found in literature for other materials. For instance, the study by Haeussler et al. [27] obtained a yield of 55 µmol/g for pure ceria, a range of 116-176 µmol/g for doped ceria, and 215-217 µmol/g for another perovskite material, LSMMg. There are three possible reasons for the differing yields. The first one is that SFNM has possibly superior CO-splitting properties with respect to other materials. The other reasons are related with different experimental setups. Firstly, the study by Haeussler et al. is based on thermogravimetric analysis, while the yields of figure 45 were obtained with a bigger reactor. Moreover, the TGA study tested the material with thermal reductions at 1400°C, with the sample exposed to an inert sweep gas (argon), whereas the test described here performed the reductions at 800°C with the aid of hydrogen. Despite the lower temperature, the fuel-aided reduction is more effective than the purely thermal reduction.

4.2 Influence of sample mass on CO production

In this section, the results given by the first 5 tests, all performed with the same reactor configuration but with different sample masses, are compared and discussed. Starting with a comparison of the peaks, the plot in figure 46 below shows the average peaks at the same flow rate value of 500 Nml/min for the 5 tests. From Test 1 to Test 5, the mass decreases from 200 mg to 5 mg.

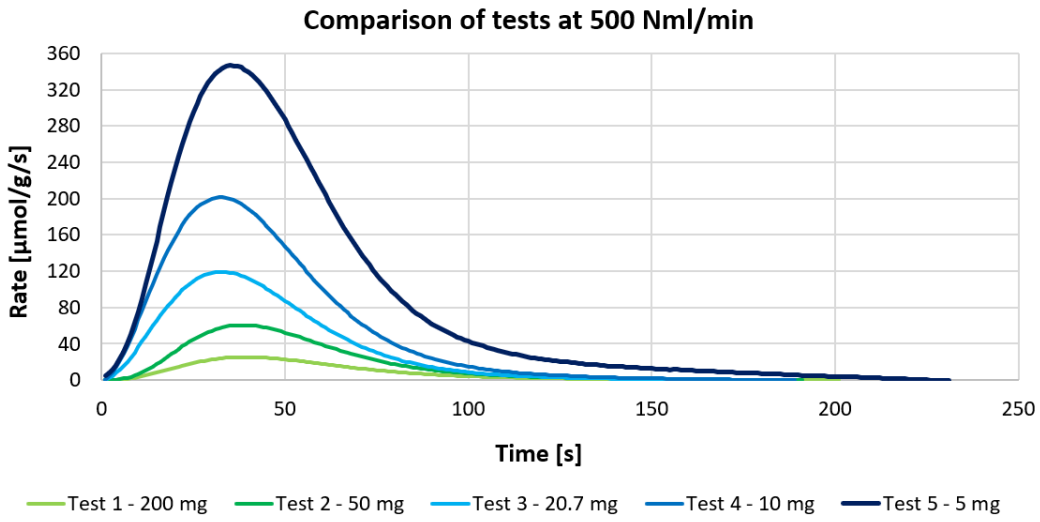

Figure 46: CO production peaks for the same flow rate of 500 Nml/min and different sample masses.

The peaks become bigger in terms of height and width with a decreasing sample mass. This means that a smaller sample, while producing a lower absolute amount of carbon monoxide, releases more CO per unit of mass. A possible explanation is that for the bigger samples the material does not react completely. The lower masses, instead, due to the higher surface-to-volume ratio and the larger excess of reactant gas (hydrogen for the reduction, carbon dioxide for the oxidation), have the opportunity to participate more in the reaction.

From the plot of figure 46, it can also be noticed that for the same flow rate value, the curves reach their maximum point roughly at the same instant of time. In addition, their t_{end}, the instant corresponding to the corrected peak going to zero, is also similar. The sample mass decrease does not move the curve left or right on the time scale, but just causes it to become taller and wider. A taller and wider curve

also results in a higher specific yield. Figure 47 is a plot of the global CO yield as a function of the oxidation flow rate in Nml/min, for the 5 tests with the crucible.

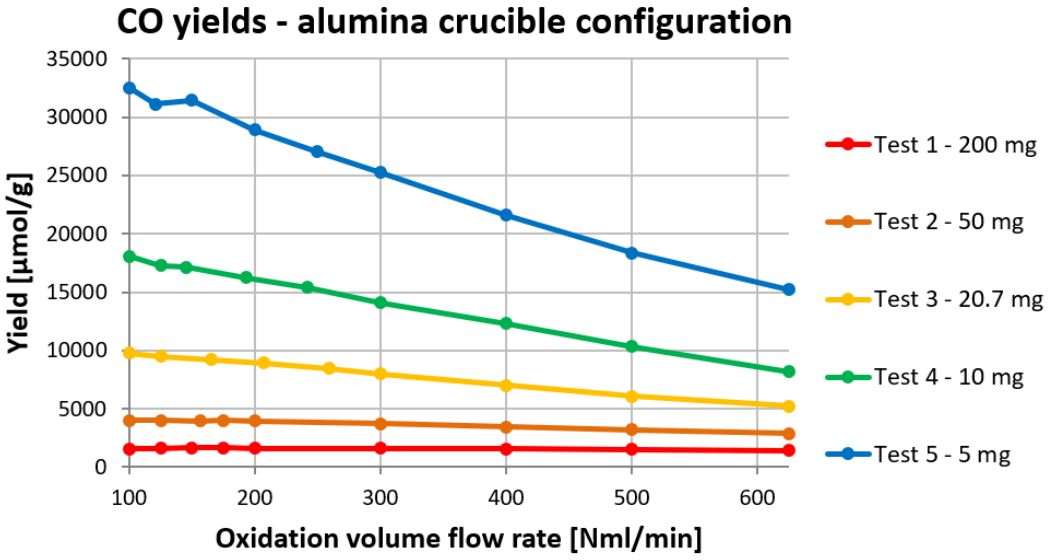

Figure 47: CO yields for Tests 1-5.

As mentioned before, the yield tends to decrease with increasing flow rate. This trend is emphasized with the lower sample masses (Tests 4 and 5). Lower masses also result in higher specific yields. In particular, the numbers obtained with the lowest values of flow rate and sample mass, like those of tests 4 and 5 in the 100÷200 Nml/min range, were deemed as unreasonably high. In fact, a yield of 30'000 µmol of CO is much bigger than the maximum amount of carbon monoxide that can be produced even considering all the oxygen atoms in the SFNM sample. Given the formula $Sr_2FeNi_{0.4}Mo_{0.6}O_6$ of the completely oxidized material, the molecular weight can be calculated. Table 4 displays the atomic weights of the various elements and the molecular weight of SFNM [58].

Formula: $Sr_2FeNi_{0.4}Mo_{0.6}O_6$

Element/Compound	Weight [g/mol]
Sr	87.62
Fe	55.85
Ni	58.69
Mo	95.95
O	16.00
SFNM	408.14

Table 4: Atomic weights of the elements that compose SFNM.

Considering that 1 mole of SFNM contains 6 moles of O, and that for each mole of oxygen released 1 mole of CO is produced, the maximum amount of CO that can be produced with 1 g of SFNM is obtained as:

$$CO_{max} = \frac{1\ [g_{SFNM}] \cdot 6\ [mol_O/mol_{SFNM}] \cdot 1\ [mol_{CO}/mol_O]}{408.14\ [g_{SFNM}/mol_{SFNM}]} \approx 0.0147\ mol$$
$$= 14700\ \mu mol \qquad (4.1)$$

Even considering a possible catalyzing effect of the SFNM, directly splitting CO_2 and producing additional CO by remaining unaltered, a yield higher than 15'000 µmol/g seems unrealistic. It has been concluded that the gas analyzer overestimates the CO concentration for low values of flow rate, especially below 200 Nml/min, and this leads to an overestimation of the yield.

4.3 Influence of the reactor configuration

The results of Tests 6 and 7, performed on the tube-in-tube reactor setup, are in this section compared to those obtained with the alumina crucible. In particular, tests 5 and 6 have different configurations but comparable sample masses (5.0 mg for Test 5 and 4.6 mg for Test 6). Figure 48 shows the curves of the average peaks before correction at the same flow rate of 500 Nml/min for Tests 5 and 6.

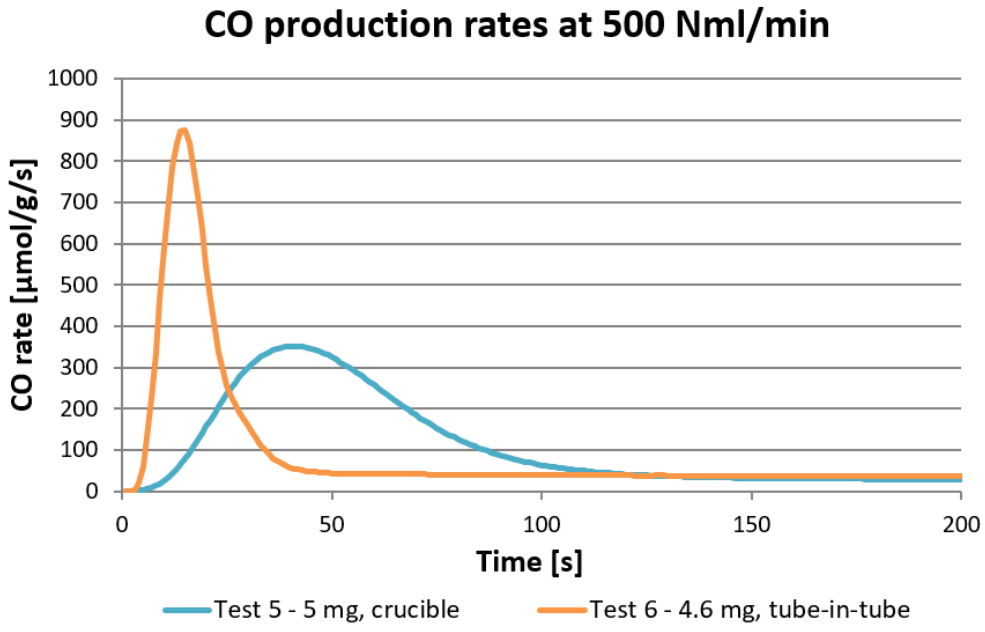

Figure 48: Comparison of peaks between Test 5 and Test 6 at the same flow rate.

The curve obtained in Test 6 with the tube-in-tube is taller and narrower than that of Test 5 relative to the alumina crucible. The reaction inside the tube-in-tube is faster due to the higher gas velocity inside the smaller tube. In terms of yield, the tube-in-tube is expected to give higher yields, as it better exposes the solid particles to the gas stream. Figure 49 below shows the yield values as a function of oxidation flow rate, in the 300÷625 Nml/min range, for Test 5 and Test 6.

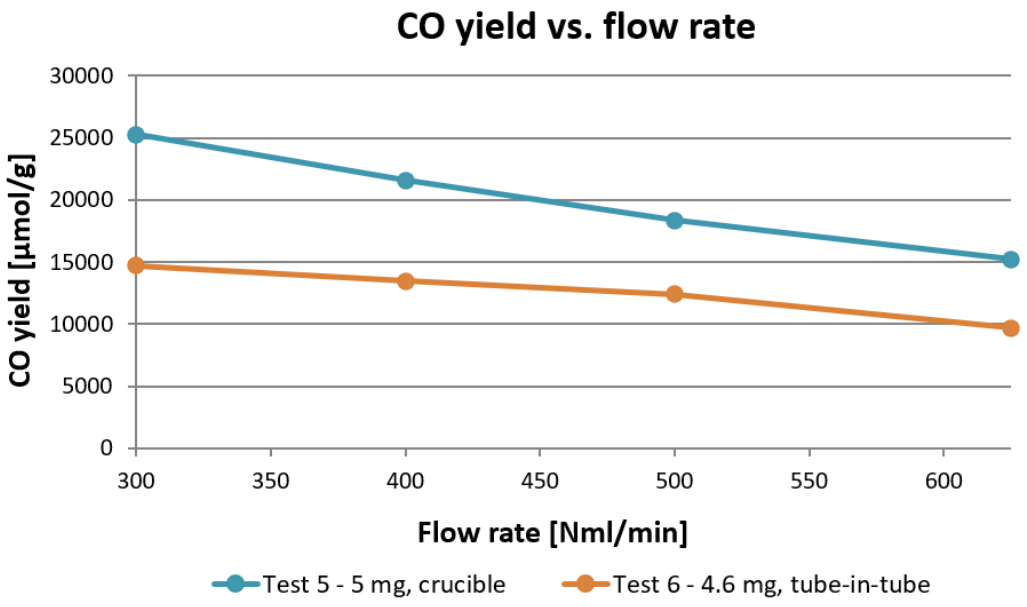

Figure 49: Comparison of yields between Test 5 and Test 6.

The plot shows that in both cases the yield decreases with increasing flow rate, but for the tube-in-tube setup the reduction is less steep. The relative difference between the yield at 300 Nml/min and the yield at 625 Nml/min is lower for the tube-in-tube, with respect to the crucible configuration. The test with the crucible unexpectedly resulted in a higher yield for the same value of flow rate. However, at the same flow rate, the material in the two reactor setups is exposed to different gas velocities, due to the different cross sections. In order to eliminate the effect of the cross section, the velocity of the gas for each flow rate value is estimated. Then, the diagram of figure 49 is changed by using the gas velocity as variable on the horizontal axis, instead of the flow rate. As the diameters of the inner and outer tubes are 8 mm (0.8 cm) and 32 mm (3.2 cm) respectively, the cross-section areas are:

$$A_{inner} = \pi \cdot \frac{D_{inner}^2}{4} = \pi \cdot \frac{0.8^2}{4} \approx 0.503\ cm^2 \qquad (4.2)$$

$$A_{outer} = \pi \cdot \frac{D_{outer}^2}{4} = \pi \cdot \frac{3.2^2}{4} \approx 8.04\ cm^2 \qquad (4.3)$$

In order to have the real flow rate in ml/min, instead of the standard one in Nml/min, the flow rate in Nml/min is multiplied by the ratio between the actual temperature inside the reactor during the oxidation phase and the normal temperature, with both temperatures expressed in K. The resulting flow rate is expressed in ml/min, which coincides with cm^3/min. Finally, by dividing the real flow rate by the area and by 60, the gas velocity in cm/s is calculated. The diagram of figure 50 is obtained.

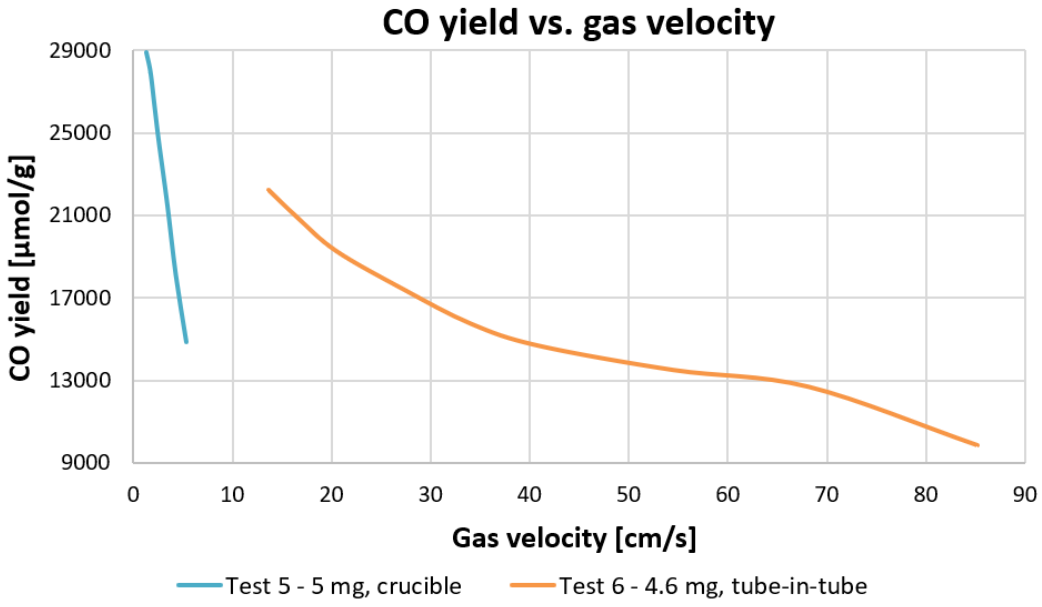

Figure 50: Comparison of yields of Test 5 and Test 6, with gas velocity on the horizontal axis.

The two reactor setups cover different ranges of gas velocity. By extrapolating the curve relative to the Test 5 for higher velocities, a lower yield with respect to the tube-in-tube would be obtained for the same velocity.

After the comparison of Tests 5 and 6 with similar masses and different setups, Tests 6 and 7 are now compared, in order to verify the relation between sample mass and CO production in the tube-in-tube configuration. Figure 51 shows the average CO rates at a fixed flow rate of 500 Nml/min for the two tests, with a plot similar to that of figure 36 for the crucible configuration.

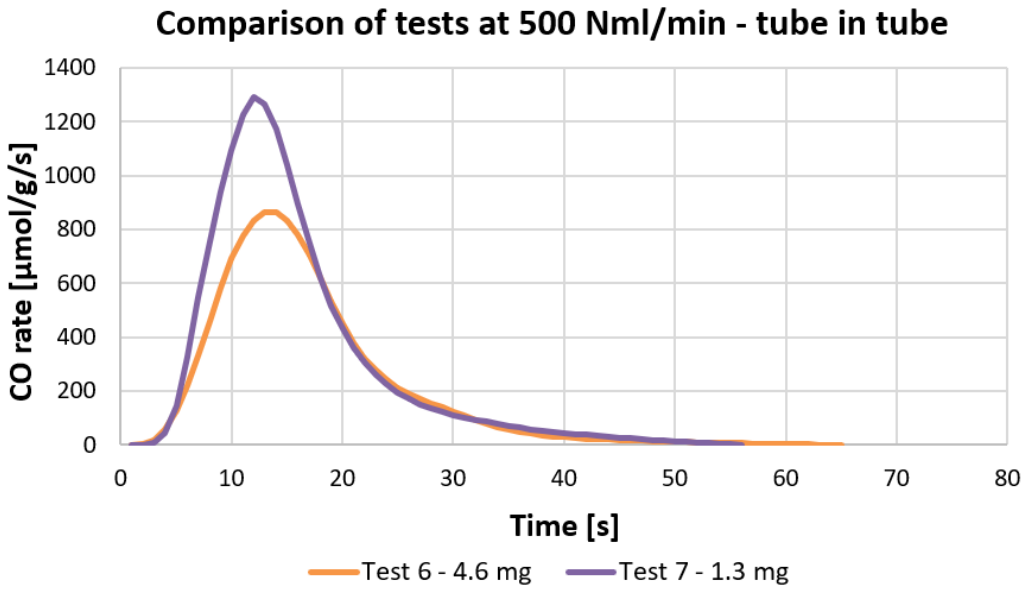

Figure 51: CO production peaks for the same flow rate of 500 Nml/min and different sample masses, in the tube-in-tube setup.

Similarly to the results obtained with the crucible, a decrease in sample mass led to a taller peak, but the width is almost the same. The time instant corresponding to the maximum value is also roughly the same for the two masses. From the shape of the peak, it can be assumed that the global CO yield increased with a smaller mass, again similarly to the crucible configuration. The plot of figure 52 confirms this assumption.

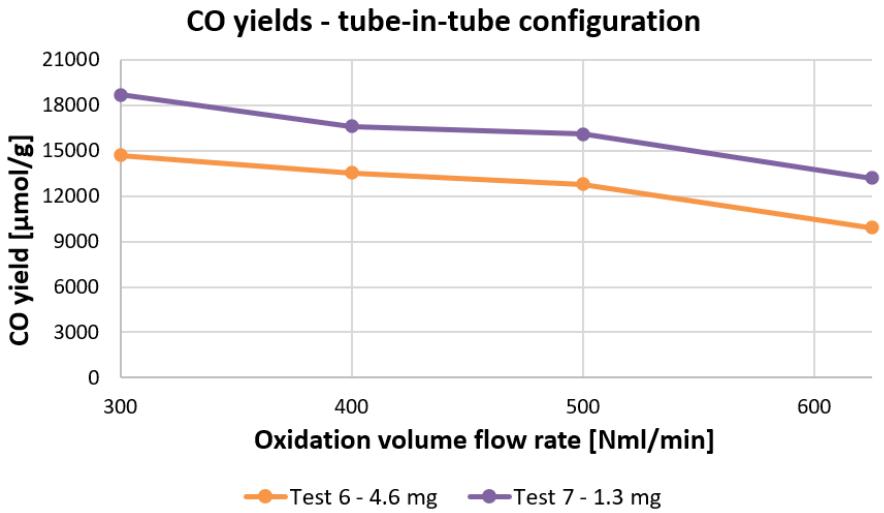

Figure 52: CO yields for Test 6 and Test 7.

As the two tests have been carried out on the same reactor setup, it is possible to compare the yield results as a function of the flow rate, as the cross section is the same (the one relative to the smaller tube) and the gas velocities are then proportional to the flow rates. The decrease of yield with increasing flow rate, already observed when comparing Test 5 and Test 6, is not particularly steep for Test 7 either. It seems that with high flow rates, which also means high gas velocities, a region where the yield is independent from the flow rate can be reached. As mentioned before, the global specific yield is higher for the test with a smaller sample mass. Unlike the plot relative to the crucible setup of figure 47, with the yield curves being more distant from each other, especially for the lowest sample masses, with the tube-in-tube the curves are relatively close to each other, meaning that in this case the yield did not vary as much with a change of sample mass. Once again, it seems possible to reach a region of independence of the yield at even lower values of sample masses. For this reason, additional tests using TGA, which can work with very low sample masses, may be useful in future. The TGA tests also make possible a direct comparison with the yields of other materials found in literature and mentioned in the previous sections, like the study by Haeussler et al. [27].

4.4 Additional test with 100% of H2 and CO

After Tests 1-7, an additional test, Test 8, was carried out on the reactor with conditions more similar to the simulated model presented in the following section. As the reactant gases used in the model are pure H_2 and pure CO_2, this test was carried out in the tube-in-tube configuration, with 100% of H_2 sent during the reduction phase and 100% of CO_2 sent during the oxidation phase. During the test, the total flow rate was kept constant at 300 Nml/min for both oxidation and reduction. In order to ensure repeatability of results, groups of three identical cycles were performed in the test. For each group of cycles, the temperature was changed in the range 550-850 °C. All the cycles are isothermal, which means that the temperature is constant during a cycle, i.e. the oxidation temperature is the same as the reduction temperature. A summary of the test is presented in Table 5 and Table 6. Table 5 is a list of the parameters that do not change between cycles, like the

sample mass and the flow rates. Table 6 is a list of the groups of cycles, each one with its temperature.

Sample mass [mg]	2.9
H_2 concentration during reduction [%]	100
Reduction flow rate [Nml/min]	300
Reduction phase duration [min]	30
CO_2 concentration during oxidation [%]	100
Oxidation flow rate [Nml/min]	300
Oxidation phase duration [min]	15

Table 5: Common parameters for all the cycles of Test 8.

Group of cycles	Temperature [°C]
1	550
2	650
3	750
4	850

Table 6: Temperatures used in Test 8.

As the reactors in the model work continuously, the total CO yield of the various cycles is not the useful parameter to enter in the simulation as input. The input for the model is a value of reaction rate, which is a constant of the simulation. The model works at a constant operative point on the rate-time curve. Figure 54 shows the average peaks of CO production rate for the four temperatures.

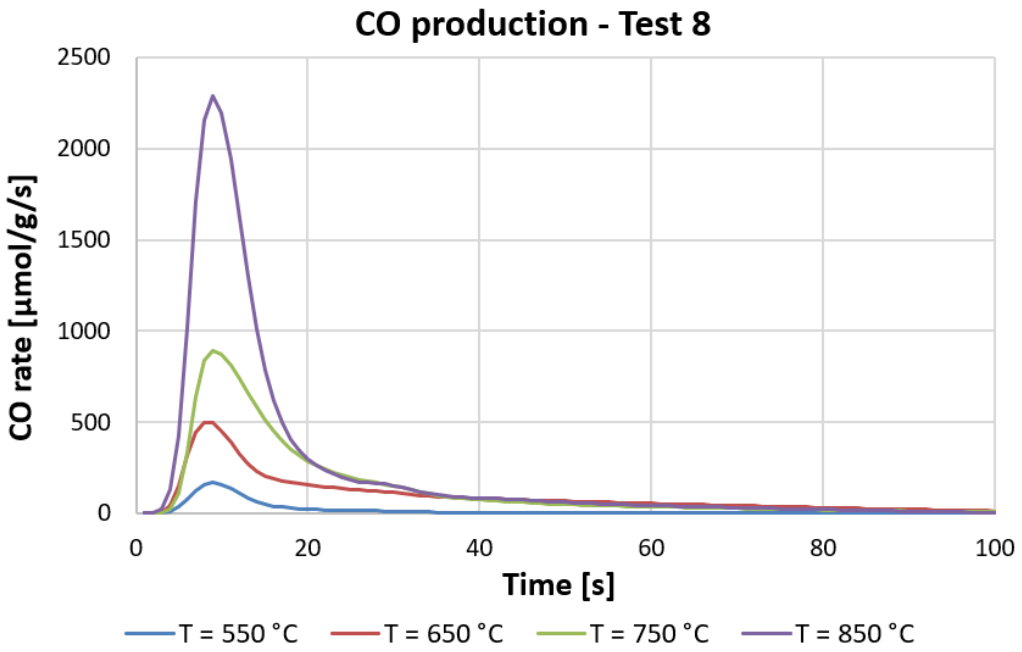

Figure 53: CO production rate peaks at 300 Nml/min for four temperatures in the range 550-850 °C.

The production rate curves have similar shapes, and reach their maximum value at the same time instant, which is consistent with the fact that the oxidation flow rate is the same. The peaks have roughly the same width, but their height increases with temperature, especially between 750 °C and 850 °C. Therefore, the yield is higher for higher temperatures. The CO_2 splitting is indeed favored by high temperatures. The peak values are summarized in Table 7.

Temperature [°C]	Maximum CO production rate [µmol/g/s]
550	167.7
650	500.2
750	889.6
850	2288

Table 7: Maximum CO rate as a function of temperature.

From the CO production rate, the molar flows of CO_2 ($\dot{n}_{CO2}$) and H_2 ($\dot{n}_{H2}$) are calculated through the following passages. Firstly, the CO rate is divided by 10^6 and multiplied by the molar weight of SFNM in g/mol (408.14 g/mol), in order to convert it from µmol/g/s to $mol_{CO}/mol_{SFNM}/s$. In the model, the molar rate of SFNM

that is transported between reactors is supposed to be equal to 1 mol_{SFNM}/s. Therefore, the converted rate obtained coincides with the flow rate of carbon monoxide in mol_{CO}/s. As one mole of CO produced corresponds to one mole of CO_2 reacted in the oxidation phase and one mole of H_2 reacted in the reduction phase, the rate in mol_{CO}/s coincides with the mol_{CO2}/s sent to the oxidation reactor and the mol_{H2}/s sent to the reduction reactor in the simulations. Table 8 is a summary of the molar rates.

Temperature [°C]	$\dot{n}_{CO2} = \dot{n}_{H2}$ **[mol/s]**
550	0.058
650	0.204
750	0.363
850	0.934

Table 8: Molar rates of CO_2 and H_2 as functions of temperature.

The molar rates represent the input parameters for the simulations with the Aspen Plus ® software. The next section focuses on these simulations, firstly by describing the model and then by discussing the results.

5. Reactor model and simulations

In this section, the reactor setup used in the experimental tests is modeled with a simulation software in order to calculate an efficiency of the process. The software used for the simulations is Aspen Plus®, a chemical process simulator widely used for chemical engineering applications. The simple model built with the software has a major difference from the experiments carried out in laboratory. While the reactor used in the tests worked in batch operation, with the material being stationary inside the reactor and cyclically exposed to different gases, the model uses stationary conditions and a constant production rate. In order to make this possible, the system is modeled with two reactors, one for the reduction phase and one for the oxidation phase, and the oxygen carrier material is transported between the two. So, the reactors are modeled as moving bed reactors. A schematic of the system is shown in Figure 54 below.

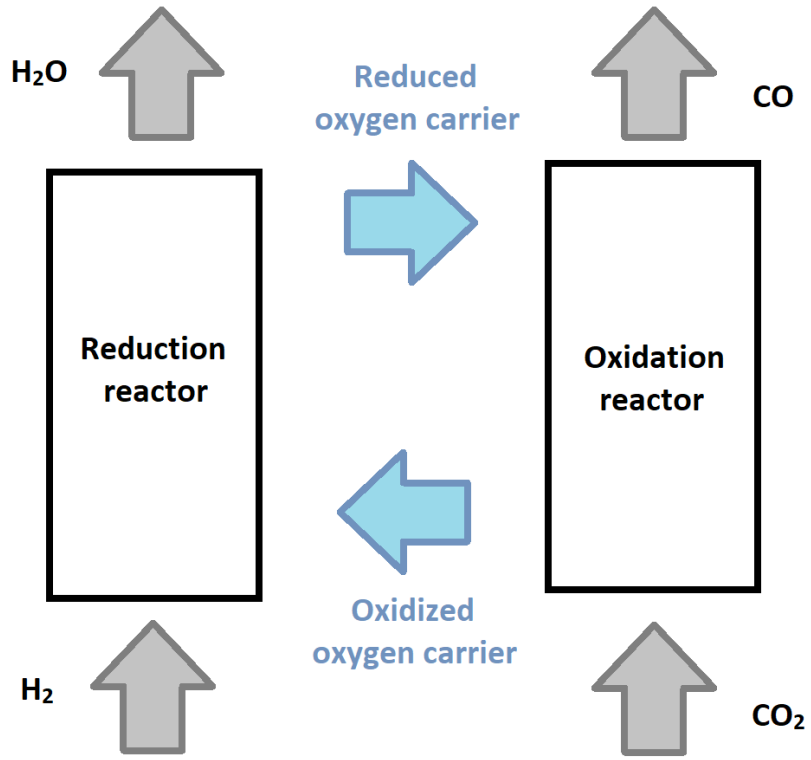

Figure 54: Schematic of the modeled redox reactors system.

The system is similar to that used in the experimental tests in the use of H_2 as fuel to aid the reduction. The gas used to reduce the SFNM oxygen carrier is pure

hydrogen, which is supposed to come from an electrolyzer, with the input electricity coming from a renewable source like a photovoltaic system. Even if the reduction is not purely thermal, a certain amount of thermal energy is necessary to preheat the reactants up to the reactor's temperature and to sustain the endothermic reaction occurring in the reduction reactor. This thermal energy is then supposed to come from a solar thermal concentrator system. The carbon monoxide produced is then mixed to additional hydrogen coming from the electrolyzer to form a syngas with a certain H_2/CO ratio.

5.1 Model description

As previously mentioned, the model splits a single reactor into two reactors for the reduction and oxidation phases. In the Aspen Plus® software, the reactors are considered as stoichiometric, with a defined conversion of the reactants. In particular, as the molar rates of CO_2 and H_2 that effectively participated in the reaction are used as inputs, CO_2 and H_2 are set to be completely converted into CO and H_2O. A schematic of the Aspen Plus® model is shown in figure 55 below.

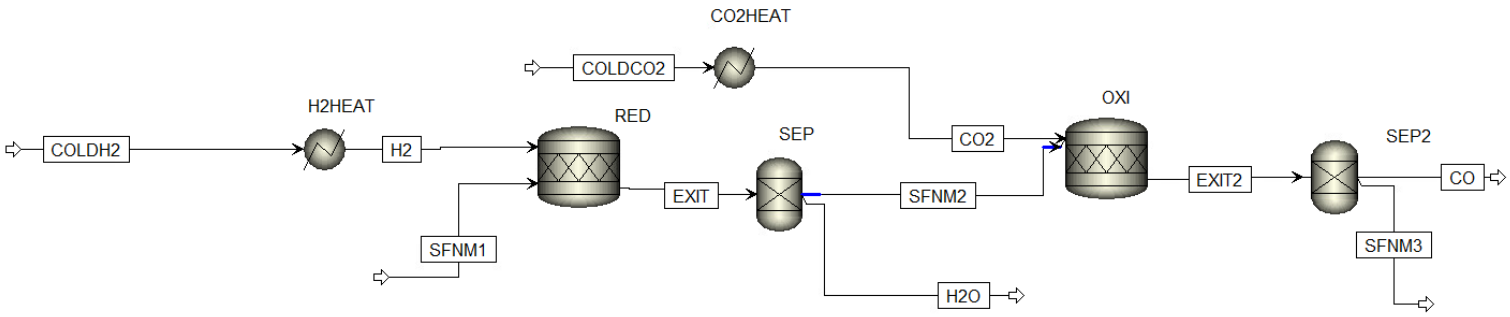

Figure 55: Schematic of the redox reactors system, as shown in the software.

The system consists of the following six components.

- A heat exchanger to warm up the hydrogen, H2HEAT. It increases the temperature from the starting level up to the level of the reaction, which is varied between simulations. The starting level depends on the origin of the hydrogen. If a solid oxide electrolyzer cell (SOEC) is close to the system, H_2 can be produced at high temperature, up to 800-900°C [59], and quickly delivered to the reactor. If a PEM (Polymer Electrolyte Membrane)

electrolyzer is chosen, or if the hydrogen production facility is far from the syngas production one, the hydrogen is available only at low temperature. In this model, the initial temperature is assumed to be equal to the lowest temperature used in the simulations, 550°C.

- The stoichiometric reduction reactor, RED. It receives the preheated hydrogen stream and the fully oxidized SFNM stream as inputs. The reducer converts completely the H_2 into H_2O and partially reduces the oxygen carrier.
- A separator (SEP) is used to split the solid SFNM from the water vapor. This separator is added to the model because the component "RStoic" that models a stoichiometric reactor in Aspen Plus® only allows for one outlet stream. A real moving bed reactor would have two different outlets, one for the solid and one for the gas.
- Another heat exchanger to warm up the carbon dioxide, CO2HEAT. The starting level of temperature for CO_2 is equal to 20°C, and the final level is equal to the temperature level of the oxidation reactor, which varies between simulations.
- The stoichiometric oxidation reactor, OXI. The inlet streams for this component are the carbon dioxide stream and the reduced SFNM. The oxidizer converts completely the CO_2 into CO and re-oxidizes the oxygen carrier.
- The second separator (SEP2) splits the solid SFNM and the carbon monoxide gas. As the molar flow rates of H_2 and CO_2 are the same, the stream SFNM3 flowing out of this separator will be identical to the inlet stream SFNM1 for the reduction reactor, closing the oxygen carrier cycle.

The simulations compute the thermal powers exchanged by the heaters and the reactors for the given conditions of temperature and flow rates. The thermal powers of the reactors only consider the heat of reaction, and do not include thermal losses. In addition, the pressure losses are not included, with all the components working at 1 bar. Before starting the simulations, the software requires an equation of state for the gases. Here, the Peng-Robinson equation of state [60] is used. Unlike the ideal gas law, the Peng-Robinson equation is cubic (as it can be written as a cubic function of the gas volume) and has additional parameters related to the critical

properties and the acentric factor of a specific gas. The critical temperature (T_c) and critical pressure (p_c) are the temperature and pressure of the critical point, where the properties of the liquid form and the gaseous form of a substance become identical [61]. Beyond the critical point, liquid and gas cannot coexist. The acentric factor (ω) is a conceptual measure of the non-sphericity of a molecule [62].

Now that the structure of the model has been described, the issue of representing the new material in the simulations needs to be addressed. As SFNM is not present in the software's libraries, it was modeled as a mixture of metal oxides. Given the formula, $Sr_2FeNi_{0.4}Mo_{0.6}O_6$, a mole of SFNM is considered in the simulations as a mixture composed of 2 mol of SrO, 0.5 mol of Fe_2O_3, 0.4 mol of NiO and 0.6 mol of MoO_3. The hydrogen will react with these oxides in the reduction phase, with iron and nickel oxides being prioritized due to the exsolution phenomenon, which moves iron and nickel particles to the surface of the material, making those particles more likely to react.

5.2 Simulation results

An example of the results obtained from the simulations, relative to the simulation number 4 at 850°C, is shown in figure 56 below. The temperature of each stream in °C and the thermal power in W exchanged by each component are displayed.

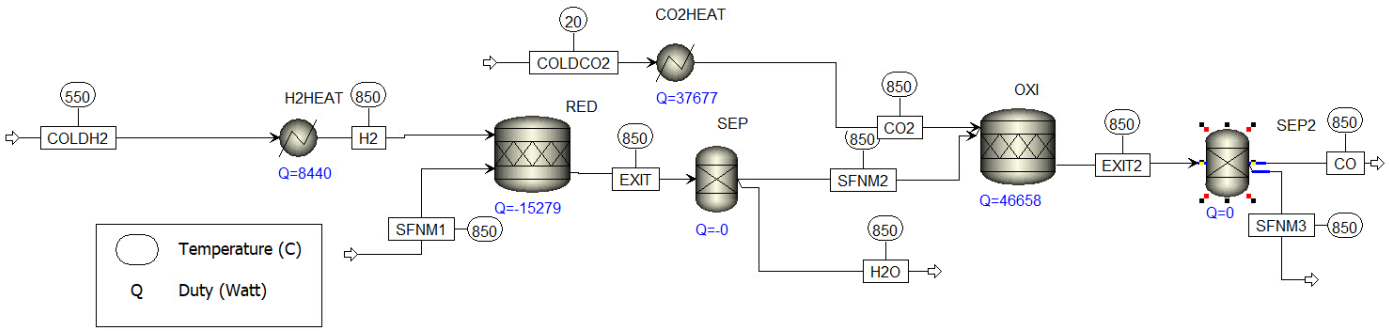

Figure 56: Results of the simulation at 850°C.

The useful output of the simulations, used for the calculations of the following sections, consists in the thermal powers displayed above, also known as the heat duties of the components. Their values in kW are summarized in the table below.

Simulation	1	2	3	4
Temperature [°C]	550	650	750	850
Q_{H2HEAT} [kW]	0	0.608	2.174	8.440
$Q_{CO2HEAT}$ [kW]	1.657	6.013	12.649	37.677
Q_{RED} [kW]	0.166	1.785	5.371	-15.279
Q_{OXI} [kW]	2.338	5.479	7.185	46.658

Table 9: Heat duties of the heaters and reactors from the simulations.

In the software, the heat duties represent heat flows absorbed by the components when positive, and released to the external environment when negative. Only one value in Table 9 is negative, and it corresponds to the reducer's heat duty at 850°C. As the perovskite material's reduction is endothermic, the heat flow was expected to be higher than zero. However, the oxidation of H_2 to H_2O is exothermic, and the heat duty of the reactor is therefore the balance between the two sides of the reaction, the solid and the gaseous one. For the lower temperatures, the endothermic behavior is more significant, while at 850°C the amount of reacted hydrogen is so high that the exothermic behavior prevails. In the oxidation reactor, the endothermic conversion of CO_2 to CO prevails over the exothermic oxidation of the perovskite. In general, the oxidizer and the carbon dioxide heater are the components that require most of the external solar heat. The next sections focus on the system efficiency calculations, for which the heat duty values of Table 9 will be used.

5.2.1 Efficiency of CO production

The efficiency of the system shown in figure 56 is defined as the ratio between the useful energy that can be extracted from the fuel and the energy spent to carry out the fuel production process. The useful energy Q_{CO} is the energy content of the produced carbon monoxide flow, and is obtained as:

$$Q_{CO} = \dot{n}_{CO} \cdot HV_{CO} \qquad (5.1)$$

In the formula, $\dot{n}_{CO}$ is the molar flow rate of CO in mol/s, which is the equal to the molar flow rate of CO_2, and HV_{CO} is the CO molar heating value, roughly equal to 282.5 kJ/mol.

The spent energy is obtained by adding two contributions, corresponding to the thermal energy Q_{TH} and to the input energy of the hydrogen used in the reduction reactor, $Q_{H2,R}$. Q_{TH} is the sum of the heat duties of the various components in the Aspen Plus® model, i.e. the values Q_{H2HEAT}, $Q_{CO2HEAT}$, Q_{RED}, and Q_{OXI} in Table 9 above. Q_{TH} corresponds to the solar thermal power coming to the reactor from the concentration system, and represents the amount of solar energy that is stored in the produced CO. The heat duties of the reactors are included in the sum only if they are positive. $Q_{H2,R}$ is calculated as:

$$Q_{H2,R} = \dot{n}_{H2} \cdot LHV_{H2} \qquad (5.2)$$

The molar flow rate of hydrogen $\dot{n}_{H2}$ is equal to the molar flow rate of CO, while the molar lower heating value of hydrogen LHV_{H2} is equal to 240 kJ/mol. Finally, the thermal efficiency is obtained as the ratio of useful energy and the spent energy.

$$\eta_{TH} = \frac{Q_{CO}}{Q_{TH} + Q_{H2,R}} \qquad (5.3)$$

The values of η_{TH} obtained for the four simulations with different temperatures are shown in the plot of figure 57 below.

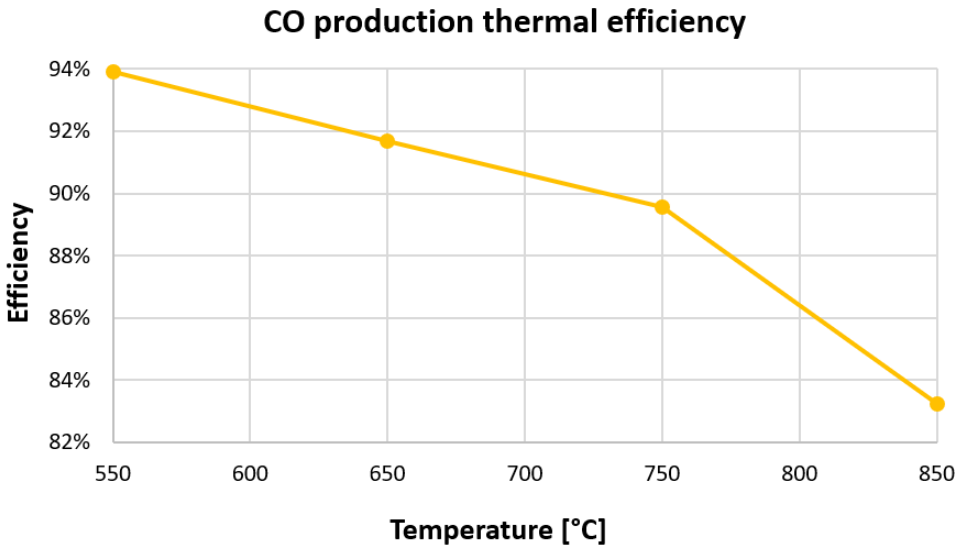

Figure 57: Thermal efficiency as function of the temperature of the reactors.

Perhaps surprisingly, the efficiency decreases with temperature. Even though the carbon monoxide yield is higher, the additional thermal demand given by the bigger flow rates of hydrogen and carbon dioxide required, and the higher level of

temperature they need to reach through preheating, lead to a lower efficiency. The efficiency could be increased by adding a thermal recovery system which uses hot streams, like the product CO, to preheat the cold streams, such as H_2 and CO_2. A pinch analysis would be needed in that case to optimize the heat transfer.

5.2.2 Efficiency of syngas production

In the previous section, the efficiency of CO production was estimated. However, CO is only a useful fuel when part of a syngas together with hydrogen. In this section, the efficiency of a system that contains both an electrolyzer (EL) for H_2 production and the chemical looping process (CL) is analyzed. This efficiency, η_{CL+EL}, is the ratio of the useful energy of the syngas and the input electric and thermal energy, and is calculated as:

$$\eta_{CL+EL} = \frac{Q_{CO} + Q_{H2,A}}{Q_{TH} + E_{H2,R} + E_{H2,A}} \qquad (5.4)$$

Q_{CO} and Q_{TH} are the same elements used for the production efficiency of pure CO. $E_{H2,R}$ is the electric power needed by the electrolyzer in order to produce the hydrogen that is used in the reduction reactor. It is equal to $Q_{H2,R}$, the energy content of the inlet H_2 stream in the reactor, divided by the electrolyzer's efficiency, η_{EL}.

$$E_{H2,R} = \frac{Q_{H2,R}}{\eta_{EL}} \qquad (5.5)$$

η_{EL} depends on the type of electrolyzer. For example, the Hylink SOEC by Sunfire has a system electrical efficiency of 84% [63], while Siemens reports a plant efficiency of 75.5% for its Silyzer 300 PEM electrolyzer [64].

$Q_{H2,A}$ is the energy content of the hydrogen that is added to CO to form a syngas. It is instead obtained as follows:

$$Q_{H2,A} = (H_2/CO) \cdot \dot{n}_{CO} \cdot LHV_{H2} \qquad (5.6)$$

H_2/CO is the hydrogen/carbon monoxide ratio which depends on the type of syngas produced. A syngas with H_2/CO ratio equal to 1 is suitable for DME synthesis, with DME being a diesel fuel substitute. Meanwhile, a syngas with a ratio of 2 can be

used to produce gasoline substitutes through Fischer-Tropsch processes. Finally, a ratio of 3 is suitable for methane production.

Dividing $Q_{H2,A}$ by the electrolyzer's efficiency, the electric power consumed by the electrolyzer to produce the additional hydrogen, $E_{H2,A}$, is obtained.

$$E_{H2,A} = \frac{Q_{H2,A}}{\eta_{EL}} \qquad (5.7)$$

Assuming an electrolyzer efficiency of 84% (corresponding to a SOEC system), the efficiency values, varying with temperature and H_2/CO ratio, are finally obtained.

H_2/CO ratio	Temperature [°C]			
	550	**650**	**750**	**850**
1	0.826	0.817	0.808	0.779
2	0.831	0.824	0.818	0.797
3	0.833	0.828	0.823	0.807

Table 10: Efficiency of the syngas production process, varying with temperature and H_2/CO ratio.

As mentioned in the previous section, the efficiency decreases with temperature. In addition, it increases with the H_2/CO ratio. This trend can be explained by looking at the plot of η_{CL+EL} in the case of H_2/CO ratio equal to zero (carbon monoxide is the only product), which means that $Q_{H2,A}$ and $E_{H2,A}$ are also null.

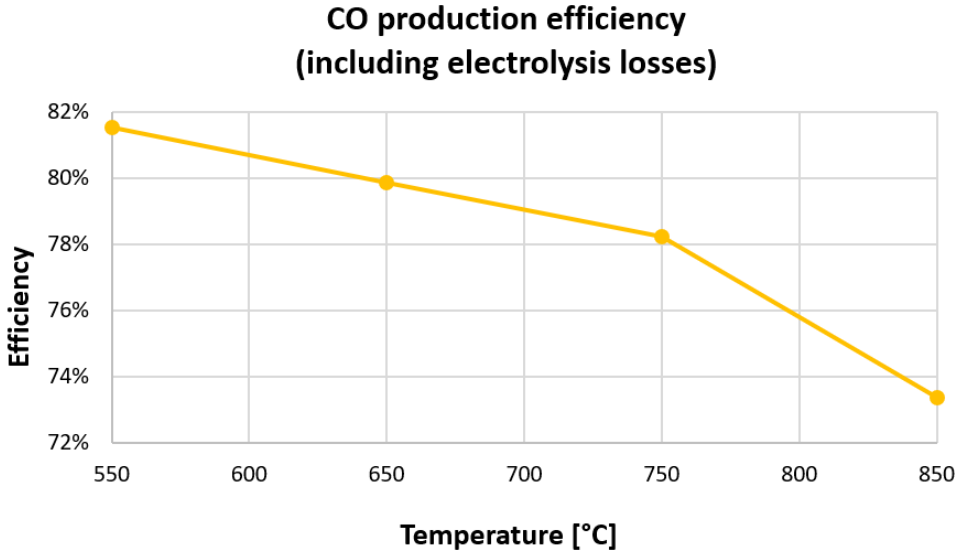

Figure 58: Efficiency of the CO production including electrolysis efficiency, with H_2/CO = 0.

The highest efficiency value, corresponding to the simulation at 550°C, is lower than the electrolysis efficiency of 84%. It is more efficient to produce a mole of H_2 with respect to a mole of CO. Thus, the more moles of H_2 are produced (increasing the H_2/CO ratio), the higher the system efficiency will be.

As an alternative to the chemical looping system described here, syngas could also be produced directly with an electrolyzer in co-electrolysis mode. In this case, CO_2 and H_2O are fed to the cell simultaneously and a CO and H_2 mixture is obtained as a result. This process is possible only with a SOEC. An example of commercial SOEC system is the Sunfire SynLink [65], which can produce a syngas with a H_2/CO ratio ranging from 1.5 to 3.5 with a system efficiency of 0.82. The plot below compares the values of η_{CL+EL} with the co-electrolysis efficiency.

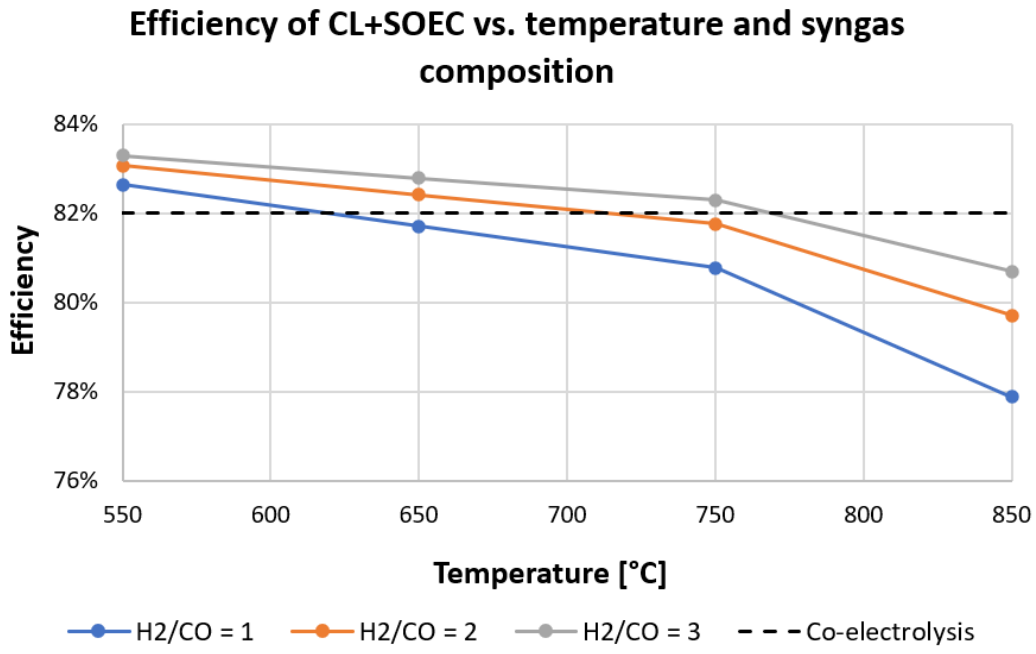

Figure 59: Efficiency comparison of the simulated system and co-electrolysis.

The simulated CL+SOEC system at 550°C is more efficient than the SOEC co-electrolysis mode, for all the H_2/CO ratios. However, as the temperature increases, together with the thermal demand of the chemical looping, the co-electrolysis becomes more efficient. Because of this, it seems that the co-electrolysis is a more convenient route to produce syngas, as it produces both H_2 and CO with a single system and high efficiency. The next step of the calculations is to estimate the solar

to fuel efficiency, assuming that the electrolysis and chemical looping processes are both driven by solar energy.

5.2.3 Solar to fuel efficiency

The solar to fuel efficiency of the CL+SOEC system is defined as:

$$\eta_{solar} = \frac{Q_{CO} + Q_{H2,A}}{Q_{sol,TH} + Q_{sol,H2,R} + Q_{sol,H2,A}} \qquad (5.8)$$

Q_{CO} and $Q_{H2,A}$ are the useful energy streams already used in the previous section. $Q_{sol,TH}$ is the solar power used to satisfy the thermal demand Q_{TH}.

$$Q_{sol,TH} = \frac{Q_{TH}}{\eta_{coll}} \qquad (5.9)$$

η_{coll} is the efficiency of the solar collection process, which depends on the type of receiver. A study by Siegel et al. [66] estimated a collection efficiency of 59% for a parabolic dish system on a yearly basis. This value is the product of four efficiencies, including the optical efficiency of the concentrator (79%), the efficiency of the receiver/reactor (83%), the efficiency of the solar resource (95%) and the operational efficiency (94%). The optical efficiency η_{opt} considers the concentrator's reflectivity (which is lower than 1, causing an energy loss), soiling of the concentrator, reflection by the quartz window of the cavity receiver, losses due to imperfect interception of the receiver, and losses due to imperfect tracking of the sun. The receiver's efficiency η_{rec} considers thermal losses due to radiation, with convection and conduction assumed as negligible. The solar resource efficiency η_{res} represents the energy losses due to insufficient solar irradiation during the day. A threshold in terms of direct normal irradiation (DNI) of 300 W/m^2 was assumed to be equal to the minimum insolation needed to reach the desired reactor temperature. Then, the data of a Typical Meteorological Year (TMY) was analyzed for the spring equinox, and the amount of energy available at irradiation higher than the threshold was calculated. The resource efficiency is the ratio between this available energy and the total energy. Finally, the operational efficiency η_{oper} takes into account the yearly average energy losses due to

maintenance, blocking between concentrators, and periods of deactivation due to excessive wind speeds.

Another study, by Pitz-Paal et al. [67], estimates the collection efficiency of a central receiver system, with a set of heliostats and a central tower. This type of system includes additional losses with respect to the parabolic dish, including cosine losses and atmospheric attenuation. The cosine loss is caused by the positioning of the heliostats, which differently from a parabolic dish pointing directly at the sun, point towards the tower. Or, more precisely, at a position between the sun and the receiver tower [66]. The atmospheric attenuation losses are caused by the scattering of the reflected beam between the heliostats and the tower, and depend on the distance between them [68]. In addition, the heliostats' shape is different than a paraboloid, which is the ideal shape, and this nonideal shape further reduces the collection efficiency of the central tower system with respect to the parabolic dish. Ultimately, the collection efficiency estimated by Pitz-Paal et al. [67] is equal to 30%. Both this value and the 59% obtained by Siegel et al. [66] refer to thermochemical cycles operating at temperatures higher than the 550-850°C range used in the simulations, and equal to 1500°C and 1700°C, respectively. The receiver's thermal losses depend on temperature. If convection and conduction losses are neglected, and the cavity's emissivity is assumed to be equal to 1 (the receiver is modeled as a perfectly insulated black body), the receiver's efficiency can be obtained as [21]:

$$\eta_{rec} = 1 - \frac{\sigma \cdot T^4}{I \cdot C} \qquad (5.10)$$

In the formula, σ is the Stefan-Boltzmann constant, equal to $5.67 \cdot 10^{-8}\ W/(m^2 \cdot K^4)$, T is the receiver's temperature in K, I is the normal irradiation in W/m^2, and C is the concentration ratio. As the receiver radiation losses depend on the fourth power of T, a lower temperature leads to much lower losses, and higher η_{rec}. Therefore, the simulated system would have a higher collection efficiency that the values presented in the studies. In order to make a conservative estimation, a η_{coll} of 30% is used in the following calculations.

The last new terms in the solar efficiency formula are $Q_{sol,H2,R}$ and $Q_{sol,H2,A}$. They represent the solar power used to generate the electricity that drives the electrolyzer,

and are calculated by dividing the electric powers consumed by the SOEC by a solar to electricity efficiency value.

$$Q_{sol,H2,R} = \frac{E_{H2,R}}{\eta_{solar\ to\ electricity}} \quad (5.11), \quad Q_{sol,H2,A} = \frac{E_{H2,A}}{\eta_{solar\ to\ electricity}} \quad (5.12)$$

The solar to electricity value is taken from the study of Siegel et al. [66] and equal to 15%. It is an estimation of the yearly average efficiency of a photovoltaic (PV) system. Finally, the solar to fuel efficiency can be computed for all the simulations, and the values are displayed in Table 11.

H_2/CO ratio	Temperature [°C]			
	550	**650**	**750**	**850**
1	0.130	0.129	0.129	0.126
2	0.129	0.128	0.128	0.126
3	0.128	0.128	0.127	0.126

Table 11: Solar to fuel efficiency, varying with temperature and H_2/CO ratio.

Differently from $\eta_{CL+SOEC}$, η_{solar} tends to decrease with increasing H_2/CO ratio. Once again, the trend can be explained by comparing the efficiency of CO production (H_2/CO equal to zero) with the solar electrolysis efficiency, which is the product of the photovoltaic system efficiency (15%) and the SOEC efficiency (84%).

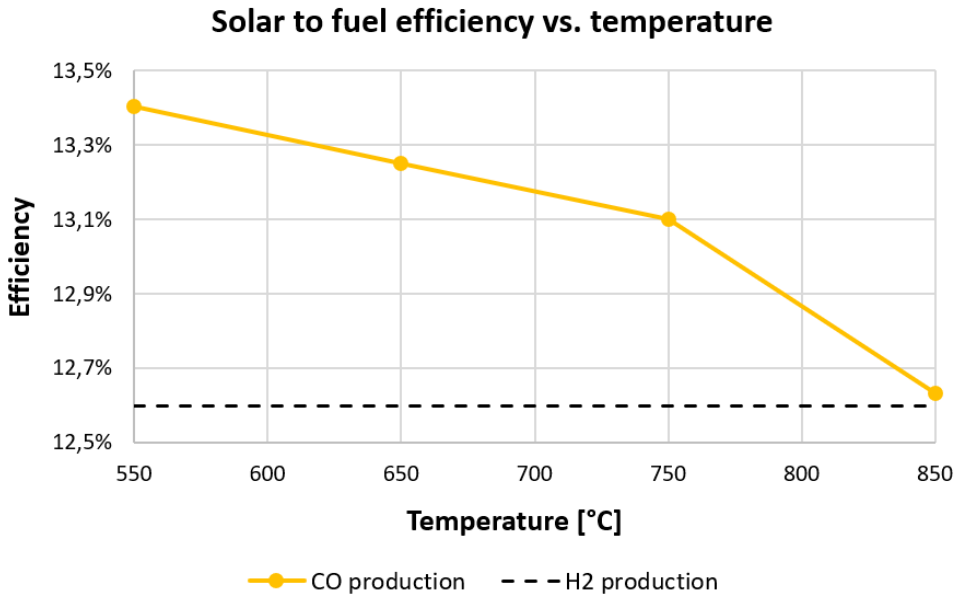

Figure 60: Solar to fuel efficiency. Comparison between CO production with chemical looping and H2 production with electrolysis.

In this case, it is more efficient to produce 1 mole of CO with respect to 1 mole of hydrogen, especially for low temperatures. Thus, every additional mole of hydrogen (increasing H_2/CO) reduces the average efficiency. At 850°C, the CO from chemical looping and the H_2 from electrolysis are produced with the same efficiency of 0.126, meaning that the overall efficiency does not depend on the H_2/CO ratio. Finally, the solar to fuel efficiencies of Table 10 can be compared with the solar co-electrolysis efficiency, product of the photovoltaic (15%) and co-electrolysis (82%) efficiencies. The plot of figure 61 is obtained.

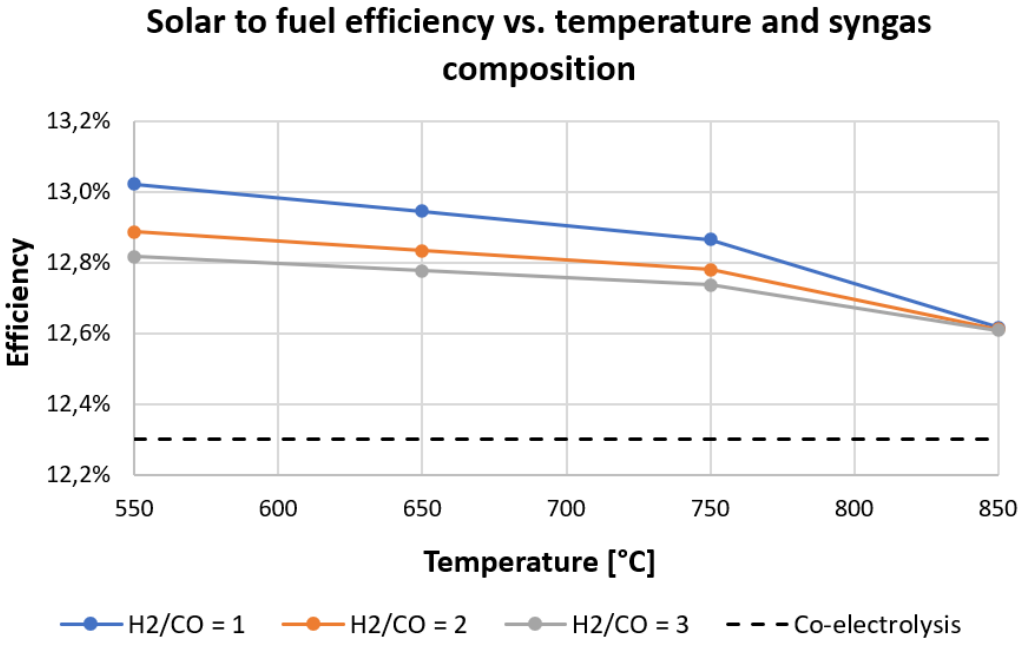

Figure 61: Solar to fuel efficiency comparison of the simulated system and co-electrolysis.

For all the temperature and H_2/CO ratio values, the chemical looping system is more efficient than the electrolysis. The reason is that it is more efficient to convert the solar radiation in thermal power (30% of solar collection efficiency) through a concentration system, than generating electricity through a PV system (15% of yearly estimated efficiency). The difference between the two systems is small, however. A cost analysis would be needed to estimate if the addition of a chemical looping system is worth due to the better efficiency, or if the co-electrolysis is cheaper. Nevertheless, these results show that a chemical looping system is in general more efficient than electrolysis. So, a pure CL that produces both H_2 and

CO, without the need of external hydrogen, would be definitely better than the PV+SOEC process. More experimental and modeling tests will be needed in the future to assess the hydrogen production rate of the SFNM oxygen carrier.

6. Conclusions

The aim of this work is to present experimental and simulation studies on a new perovskite material, $Sr_2FeNi_{0.4}Mo_{0.6}O_6$ (SFNM), which can operate in a two-step chemical looping process to produce fuels from carbon dioxide. The experimental tests run in laboratory using a small tubular reactor showed promising results in terms of carbon monoxide production rate and global yield. The obtained yield changed with temperature, sample mass, total flow rate during oxidation and also reactor configuration, but the results showed good repeatability for fixed conditions. The highest specific yields were obtained at 850°C, the highest temperature used in the tests, and for low flow rates and sample masses. The influence of flow rate on the results was mainly attributed to the gas analysis instrument, while temperature and sample mass actually affect the CO production. The yields were higher than those of other materials found in literature, and these higher values are attributed to various different causes. Firstly, the reactor setup could result in conditions more favorable for the reaction between the gas and the solid material, with respect to the TGA tests commonly used for other materials. Then, the tests were carried out with a reduction phase in reducing atmosphere, instead of using a purely thermal reduction in inert gas. Finally, SFNM could indeed have better CO_2-splitting properties than other materials, due to its crystalline structure and the fact that it contains iron and nickel, which are common catalyst materials. Iron and nickel also participate in the exsolution phenomenon, which causes Fe and Ni particles to move to the perovskite material's surface at high temperatures. The exsolution could cause a catalytic process which increases the CO production without oxygen intake by the material.

The carbon monoxide production process was then simulated in order to estimate the thermal efficiency in the best scenario, which means keeping the reactor at the conditions of maximum CO production rate and using the minimum flow rates of reactant gases, H_2 for the reduction phase and CO_2 for the oxidation phase, in a continuous cycle. The obtained efficiencies are around 80% considering only the thermochemical cycle coupled to an electrolysis system, and around 13% in terms of solar to fuel efficiency. The solar to fuel efficiency was found to be higher than that of a pure electrolysis, but the need for hydrogen from an external source for the

reduction can make the additional step of adding the chemical looping process not worth in economic terms.

Because of this, more tests are needed in the future with the aim to estimate the hydrogen productivity of the SFNM material. In this way, the same chemical looping process can produce H_2 and CO simultaneously. Other tests with a thermogravimetric analysis device are also needed, so that the carbon monoxide yield can be directly compared to that of other perovskite materials. The following phase would be to test the material with a completely thermal reduction phase, without the need for hydrogen as input for the reactor. The hydrogen demand would be substituted with the use of solar thermal energy through solar concentrators. Thus, the solar radiation would be directly used for the fuel production.

The product of a system that splits both water and carbon dioxide would be syngas, that represents a versatile platform from which various useful fuels can be obtained. Methane, gasoline substitute fuels (Fischer-Tropsch fuels) and diesel substitute fuels (DME), can all be produced starting from syngas. If those fuels are manufactured through processes driven by renewable energy, and if carbon capture technologies are employed, the energy consumption route would be decarbonized, in the sense that the produced carbon dioxide is not emitted. Instead, CO_2 becomes a raw material. Furthermore, the user devices that need fuel to work would not be completely replaced by a different technology, but can just continue to utilize fuel.

In general, the chemical looping technologies involving solid metal oxides to produce hydrogen or syngas are not yet at a high stage of development. As the concept is being validated in laboratory scale experiments, the Technology Readiness Level (TRL) is around 4. The TRL is however lower for a system that actually combines the chemical looping process with solar concentrators to extract the needed thermal energy. Such a system would have significant additional challenges, like the variability of the solar radiation, which would make the reactors operate with lower yields, or even not operate at all, during certain periods of time. For example during the night, if the process is driven by direct sunlight and no storage system is present. In conclusion, chemical looping processes for hydrogen and syngas production are promising alternatives to other technologies for a decarbonization pathway, especially as an intermediate point between the current global situation, where fossil fuels are still prevailing over renewables in terms of

primary energy consumption, and a future situation where the renewable energies are directly employed to a greater extent. In the near future, research on the chemical looping production of fuels will have to study its feasibility at large scale and select the best materials in terms of costs and yields, between the traditional metal oxides and the more recent perovskites.

Bibliography

[1] IPCC, 2014: *Climate Change 2014: Synthesis Report. Contribution of Working Groups I, II and III to the Fifth Assessment Report of the Intergovernmental Panel on Climate Change* [Core Writing Team, R.K. Pachauri and L.A. Meyer (eds.)]. IPCC, Geneva, Switzerland, 151 pp.

[2] United Nations, United Nations Sustainable Development Goals, Available online: https://www.un.org/sustainabledevelopment/climate-change/

[3] Hannah Ritchie and Max Roser (2020) - "CO_2 and Greenhouse Gas Emissions". *Published online at OurWorldInData.org.* Retrieved from: 'https://ourworldindata.org/co2-and-other-greenhouse-gas-emissions' [Online Resource]

[4] BP Statistical Review of World Energy 2020. Available online: https://www.bp.com/content/dam/bp/business-sites/en/global/corporate/pdfs/energy-economics/statistical-review/bp-stats-review-2020-full-report.pdf

[5] IEA (2020), *Global CO2 emissions in 2019*, IEA, Paris. Available online: https://www.iea.org/articles/global-co2-emissions-in-2019

[6] IEA, Global Energy Review 2020. Available online: https://www.iea.org/reports/global-energy-review-2020

[7] United Nations, *Fall in COVID-linked carbon emissions won't halt climate change - UN weather agency chief*, 22 April 2020. Available online: https://news.un.org/en/story/2020/04/1062332

[8] IEA, *Monthly evolution of global CO2 emissions, 2020 relative to 2019, IEA, Paris*, https://www.iea.org/data-and-statistics/charts/monthly-evolution-of-global-co2-emissions-2020-relative-to-2019.

[9] World Energy Council, *World Energy Resources 2013 Survey*. Available online: https://www.worldenergy.org/publications/entry/world-energy-resources-2013-survey.

[10] Christos Agrafiotis, Martin Roeb, Christian Sattler, *A review on solar thermal syngas production via redox pair-based water/carbon dioxide splitting thermochemical cycles*, Renewable and Sustainable Energy Reviews, Volume 42, 2015, Pages 254-285, ISSN 1364-0321, https://doi.org/10.1016/j.rser.2014.09.039. (https://www.sciencedirect.com/science/article/pii/S1364032114008120).

[11] Simon Koumi Ngoh, Donatien Njomo, *An overview of hydrogen gas production from solar energy*, Renewable and Sustainable Energy Reviews, Volume 16, Issue 9, 2012, Pages 6782-6792, ISSN 1364-0321, https://doi.org/10.1016/j.rser.2012.07.027.
(https://www.sciencedirect.com/science/article/pii/S1364032112004698).

[12] S. Galli, M. Stefanoni, *Development of a solar-hydrogen cycle in Italy*, International Journal of Hydrogen Energy, Volume 22, Issue 5, 1997, Pages 453-458, ISSN 0360-3199, https://doi.org/10.1016/S0360-3199(96)00105-X. (https://www.sciencedirect.com/science/article/pii/S036031999600105X)

[13] A. Szyszka*, Ten years of solar hydrogen demonstration project at Neunburg vorm Wald, Germany*, International Journal of Hydrogen Energy, Volume 23, Issue 10, 1998, Pages 849-860, ISSN 0360-3199, https://doi.org/10.1016/S0360-3199(97)00172-9.
(https://www.sciencedirect.com/science/article/pii/S0360319997001729)

[14] C. Meurer, H. Barthels, W.A. Brocke, B. Emonts, H.G. Groehn*, PHOEBUS—an autonomous supply system with renewable energy: six years of operational experience and advanced concepts*, Solar Energy, Volume 67, Issues 1–3, 1999, Pages 131-138, ISSN 0038-092X, https://doi.org/10.1016/S0038-092X(00)00043-8. (https://www.sciencedirect.com/science/article/pii/S0038092X00000438)

[15] Tatsuya Kodama and Nobuyuki Gokon, *Thermochemical Cycles for High-Temperature Solar Hydrogen Production*, Chemical Reviews 2007 107 (10), 4048-4077, DOI: 10.1021/cr050188a

[16] Haldor Topsøe, *From solid fuels to substitute natural gas (SNG) using TREMP™*. Available online: https://www.netl.doe.gov/sites/default/files/netl-file/tremp-2009.pdf

[17] Emanuele Giglio, Andrea Lanzini, Massimo Santarelli, Pierluigi Leone, *Synthetic natural gas via integrated high-temperature electrolysis and methanation: Part I—Energy performance*, Journal of Energy Storage, Volume 1, 2015, Pages 22-37, ISSN 2352-152X, https://doi.org/10.1016/j.est.2015.04.002. (https://www.sciencedirect.com/science/article/pii/S2352152X15000067)

[18] Vincent Dieterich, Alexander Buttler, Andreas Hanel, Hartmut Spliethoffab and Sebastian Fendt, *Power-to-liquid via synthesis of methanol, DME or Fischer–Tropsch-fuels: a review*, Energy Environ. Sci., 2020, 13, 3207, DOI: 10.1039/d0ee01187h

[19] Thyssenkrupp, *Methanol* plants, https://www.swiss-liquid-future.ch/wp-content/uploads/2018/02/TK_17_0487_Methanol-Broschuere_13.pdf

[20] Reinhard Rauch, Alain Kiennemann, Anca Sauciuc, *Chapter 12 - Fischer-Tropsch Synthesis to Biofuels (BtL Process)*. The Role of Catalysis for the Sustainable Production of Bio-fuels and Bio-chemicals, Elsevier, 2013, Pages 397-443, ISBN 9780444563309, https://doi.org/10.1016/B978-0-444-56330-9.00012-7. (https://www.sciencedirect.com/science/article/pii/B9780444563309000127)

[21] A. Steinfeld, *Solar hydrogen production via a two-step water-splitting thermochemical cycle based on Zn/ZnO redox reactions*, International Journal of Hydrogen Energy, Volume 27, Issue 6, 2002, Pages 611-619, ISSN 0360-3199, https://doi.org/10.1016/S0360-3199(01)00177-X. (https://www.sciencedirect.com/science/article/pii/S036031990100177X)

[22] M. E. Gálvez, P. G. Loutzenhiser, I. Hischier, and A. Steinfeld, *CO2 Splitting via Two-Step Solar Thermochemical Cycles with Zn/ZnO and FeO/Fe3O4 Redox Reactions: Thermodynamic Analysis*, Energy Fuels 2008, 22, 5, 3544–3550. Publication Date: August 13, 2008. https://doi-org.ezproxy.biblio.polito.it/10.1021/ef800230b

[23] Kromer, M., Roth, K., Takata, R., Chin, P. *Support for cost analyses on solardriven high temperature thermochemical water-splitting cycles*. DEDT0000951, final report to Department of Energy, by TIAX, LLC. Lexington, MA, U.S.A.; 2011.

[24] Stéphane Abanades, *CO2 and H2O reduction by solar thermochemical looping using SnO2/SnO redox reactions: Thermogravimetric analysis*, International Journal of Hydrogen Energy, Volume 37, Issue 10, 2012, Pages 8223-8231, ISSN 0360-3199, https://doi.org/10.1016/j.ijhydene.2012.02.158. (https://www.sciencedirect.com/science/article/pii/S036031991200523X)

[25] Kyoung-Soo Kang, Chang-Hee Kim, Won-Chul Cho, Ki-Kwang Bae, Sung-Hyun Kim, Chu-Sik Park, *Novel two-step thermochemical cycle for hydrogen production from water using germanium oxide: KIER 4 thermochemical cycle*, International Journal of Hydrogen Energy, Volume 34, Issue 10, 2009, Pages 4283-4290, ISSN 0360-3199, https://doi.org/10.1016/j.ijhydene.2009.03.017. (https://www.sciencedirect.com/science/article/pii/S0360319909003681)

[26] Kiyoshi Otsuka, Masaharu Hatano, Akira Morikawa*, Hydrogen from water by reduced cerium oxide, Journal of Catalysis*, Volume 79, Issue 2, 1983, Pages 493-496, ISSN 0021-9517, https://doi.org/10.1016/0021-9517(83)90346-9. (https://www.sciencedirect.com/science/article/pii/0021951783903469)

[27] Anita Haeussler, Anne Julbe, Stéphane Abanades, *Investigation of reactive perovskite materials for solar fuel production via two-step redox cycles: Thermochemical activity, thermodynamic properties and reduction kinetics*, Materials Chemistry and Physics, Volume 276, 2022, 125358, ISSN 0254-0584, https://doi.org/10.1016/j.matchemphys.2021.125358. (https://www.sciencedirect.com/science/article/pii/S025405842101141X)

[28] Andrew Tong, Samuel Bayham, Mandar V. Kathe, Liang Zeng, Siwei Luo, Liang-Shih Fan, *Iron-based syngas chemical looping process and coal-direct chemical looping process development at Ohio State University*, Applied Energy vol. 113, January 2014, pages 1836-1845

[29] Haeussler A, Abanades S, Jouannaux J, Julbe A. *Non-Stoichiometric Redox Active Perovskite Materials for Solar Thermochemical Fuel Production: A Review*. Catalysts. 2018, 8, 611. https://doi.org/10.3390/catal8120611

[30] Martin Hoffmann, Victor N. Antonov, Lev V. Bekenov, Kalevi Kokko, Wolfram Hergert, and Arthur Ernst, *Variation of magnetic properties of Sr2FeMoO6 due to oxygen vacancies*

[31] Zhihong Du et al. «*High-Performance Anode Material Sr2FeMo0.65Ni0.35O6 - δ with in Situ Exsolved Nanoparticle Catalyst*». In: *ACS Nano* 10.9 (2016), pp. 8660–8669. issn: 1936086X. doi: 10.1021/acsnano.6b03979

[32] Wang Fuqiang, Cheng Ziming, Tan Jianyu, Yuan Yuan, Shuai Yong, Liu Linhua, *Progress in concentrated solar power technology with parabolic trough collector system: A comprehensive review*, Renewable and Sustainable Energy Reviews, Volume 79, 2017, Pages 1314-1328, ISSN 1364-0321, https://doi.org/10.1016/j.rser.2017.05.174. (https://www.sciencedirect.com/science/article/pii/S1364032117308122)

[33] SolarPACES, *How CSP Works: Tower, Trough, Fresnel or Dish*. Available online: https://www.solarpaces.org/how-csp-works/

[34] Warren Morningstar, Stanford University, *The Physics of Solar Concentration*, December 18, 2017

[35] R.Z. Wang, Z.Y. Xu, T.S. Ge, 1 - *Introduction to solar heating and cooling systems*. Editor(s): R.Z. Wang, T.S. Ge, Advances in Solar Heating and Cooling, Woodhead Publishing, 2016, Pages 3-12, ISBN 9780081003015, https://doi.org/10.1016/B978-0-08-100301-5.00001-1. (https://www.sciencedirect.com/science/article/pii/B9780081003015000011)

[36] A. Yogev, A. Kribus, M. Epstein, A. Kogan, *Solar "tower reflector" systems: A new approach for high-temperature solar plants*, International Journal of Hydrogen Energy, Volume 23, Issue 4, 1998, Pages 239-245, ISSN 0360-3199, https://doi.org/10.1016/S0360-3199(97)00059-1. (https://www.sciencedirect.com/science/article/pii/S0360319997000591)

[37] Murmura Maria Anna, Annesini Maria. (2020). *Methodologies for the Design of Solar Receiver/Reactors for Thermochemical Hydrogen Production*. Processes, 8. DOI: 10.3390/pr8030308.

[38] Storch Henrik, Roeb Martin, Stadler Hannes, Hoffschmidt Bernhard. (2015). *Methanol production via solar reforming of methane*.

[39] H. Jouhara, A. Chauhan, T. Nannou, S. Almahmoud, B. Delpech, L.C. Wrobel, *Heat pipe based systems - Advances and applications*, Energy, Volume 128, 2017, Pages 729-754, ISSN 0360-5442, https://doi.org/10.1016/j.energy.2017.04.028. (https://www.sciencedirect.com/science/article/pii/S0360544217305935)

[40] Zhirong Liao, Amir Faghri, *Thermal analysis of a heat pipe solar central receiver for concentrated solar power tower*, Applied Thermal Engineering, Volume 102, 2016, Pages 952-960, ISSN 1359-4311, https://doi.org/10.1016/j.applthermaleng.2016.04.043. (https://www.sciencedirect.com/science/article/pii/S1359431116305294)

[41] Caraballo A., Galán-Casado S., Caballero Á., Serena S., *Molten Salts for Sensible Thermal Energy Storage: A Review and an Energy Performance Analysis*. Energies 2021, 14, 1197. https://doi.org/10.3390/en14041197

[42] Storch, Henrik & Roeb, Martin & Stadler, Hannes & Hoffschmidt, Bernhard. (2015). *Methanol production via solar reforming of methane*.

[43] Loutzenhiser P.G., Meier A., Steinfeld A., *Review of the Two-Step H2O/CO2-Splitting Solar Thermochemical Cycle Based on Zn/ZnO Redox Reactions*. Materials 2010, 3, 4922-4938. https://doi.org/10.3390/ma3114922

[44] Gstoehl, D., Brambilla, A., Schunk, L.O. et al. *A quenching apparatus for the gaseous products of the solar thermal dissociation of ZnO*. J Mater Sci 43, 4729–4736 (2008). https://doi.org/10.1007/s10853-007-2351-x

[45] Villasmil W., Brkic M., Wuillemin D., Meier A. and Steinfeld A. (November 8, 2013). *Pilot Scale Demonstration of a 100-kWth Solar Thermochemical Plant for the Thermal Dissociation of ZnO*. ASME. J. Sol. Energy Eng. February 2014; 136(1): 011016. https://doi-org.ezproxy.biblio.polito.it/10.1115/1.4025512

[46] Christopher Perkins, Paul R. Lichty, Alan W. Weimer, *Thermal ZnO dissociation in a rapid aerosol reactor as part of a solar hydrogen production cycle*, International Journal of Hydrogen Energy, Volume 33, Issue 2, 2008, Pages 499-

510, ISSN 0360-3199, https://doi.org/10.1016/j.ijhydene.2007.10.021. (https://www.sciencedirect.com/science/article/pii/S0360319907005873)

[47] Tom Melchior, Christopher Perkins, Alan W. Weimer, Aldo Steinfeld, *A cavity-receiver containing a tubular absorber for high-temperature thermochemical processing using concentrated solar energy*, International Journal of Thermal Sciences, Volume 47, Issue 11, 2008, Pages 1496-1503, ISSN 1290-0729, https://doi.org/10.1016/j.ijthermalsci.2007.12.003. (https://www.sciencedirect.com/science/article/pii/S129007290700258X)

[48] Ermanoski I., Siegel N. P., and Stechel E. B. (February 8, 2013). *A New Reactor Concept for Efficient Solar-Thermochemical Fuel Production*. ASME. J. Sol. Energy Eng. August 2013; 135(3): 031002. https://doi-org.ezproxy.biblio.polito.it/10.1115/1.4023356

[49] M. Roeb, J.-P. Säck, P. Rietbrock, C. Prahl, H. Schreiber, M. Neises, L. de Oliveira, D. Graf, M. Ebert, W. Reinalter, M. Meyer-Grünefeldt, C. Sattler, A. Lopez, A. Vidal, A. Elsberg, P. Stobbe, D. Jones, A. Steele, S. Lorentzou, C. Pagkoura, A. Zygogianni, C. Agrafiotis, A.G. Konstandopoulos*, Test operation of a 100kW pilot plant for solar hydrogen production from water on a solar tower*, Solar Energy, Volume 85, Issue 4, 2011, Pages 634-644, ISSN 0038-092X, https://doi.org/10.1016/j.solener.2010.04.014. (https://www.sciencedirect.com/science/article/pii/S0038092X10001623)

[50] Anis Houaijia, Christian Sattler, Martin Roeb, Matthias Lange, Stefan Breuer, Jan Peter Säck, *Analysis and improvement of a high-efficiency solar cavity reactor design for a two-step thermochemical cycle for solar hydrogen production from water*, Solar Energy, Volume 97, 2013, Pages 26-38, ISSN 0038-092X, https://doi.org/10.1016/j.solener.2013.07.032. (https://www.sciencedirect.com/science/article/pii/S0038092X13003071)

[51] Djamal, Darfilal. *of Recent advanced in solar thermochemical reactors for hydrogen production from water*. (2015).

[52] Hiroshi Kaneko, Takao Miura, Akinori Fuse, Hideyuki Ishihara, Shunpei Taku, Hiroaki Fukuzumi, Yuuki Naganuma, and Yutaka Tamaura, *Rotary-Type Solar Reactor for Solar Hydrogen Production with Two-step Water Splitting Process*. Energy & Fuels 2007 21 (4), 2287-2293. DOI: 10.1021/ef060581z

[53] Lapp J., Davidson J. H., and Lipiński W. (March 22, 2013). *Heat Transfer Analysis of a Solid-Solid Heat Recuperation System for Solar-Driven Nonstoichiometric Redox Cycles*. ASME. J. Sol. Energy Eng. August 2013; 135(3): 031004. https://doi-org.ezproxy.biblio.polito.it/10.1115/1.4023357

[54] Carbolite Gero, *Vacuum, Inert and Reactive Gas Furnaces up to 3000 °C* brochure. https://www.carbolite-gero.it/dltmp/www/56936fa3-87a8-42ee-acd2-5dcabc282b86-05ec0b8722b1/brochure_catalogue_vacuum_en.pdf

[55] Chemistry LibreTexts, *The Beer-Lambert law*. Available online: https://chem.libretexts.org/Bookshelves/Physical_and_Theoretical_Chemistry_Textbook_Maps/Supplemental_Modules_(Physical_and_Theoretical_Chemistry)/Spectroscopy/Electronic_Spectroscopy/Electronic_Spectroscopy_Basics/The_Beer-Lambert_Law

[56] Fuji Electric Global. Gas analyzers, operating principles. https://www.fujielectric.com/products/instruments/products/anlz_gas/genri.html

[57] Emerson, X-STREAM Enhanced Series instruction manual. https://www.emerson.com/documents/automation/manual-x-stream-enhanced-gas-analyzer-series-rosemount-en-71966.pdf

[58] IUPAC. CIAWW, Commission on Isotopic Abundances and Atomic Weights. https://www.ciaaw.org/index.htm

[59] Annabelle Brisse, Josef Schefold, Mohsine Zahid, *High temperature water electrolysis in solid oxide cells*, International Journal of Hydrogen Energy, Volume 33, Issue 20, 2008, Pages 5375-5382, ISSN 0360-3199, https://doi.org/10.1016/j.ijhydene.2008.07.120. (https://www.sciencedirect.com/science/article/pii/S0360319908008355)

[60] Ding-Yu Peng and Donald B. Robinson, *A New Two-Constant Equation of State*, Industrial & Engineering Chemistry Fundamentals 1976 15 (1), 59-64 DOI: 10.1021/i160057a011

[61] Ahmed El-Banbi, Ahmed Alzahabi, Ahmed El-Maraghi, *Chapter 3 - Dry Gases, PVT Property Correlations*, Gulf Professional Publishing, 2018, Pages 29-63, ISBN 9780128125724, https://doi.org/10.1016/B978-0-12-812572-4.00003-5. (https://www.sciencedirect.com/science/article/pii/B9780128125724000035)

[62] Saville, G. (2006), *ACENTRIC FACTOR*. *A-to-Z Guide to Thermodynamics, Heat and Mass Transfer, and Fluids Engineering*. doi:10.1615/AtoZ.a.acentric_factor.

[63] Sunfire-Hylink SOEC factsheet. https://www.sunfire.de/files/sunfire/images/content/Sunfire.de%20(neu)/Sunfire-Factsheet-HyLink-SOEC-20210303.pdf

[64] Siemens, Silyzer 300 datasheet. https://assets.siemens-energy.com/siemens/assets/api/uuid:a193b68f-7ab4-4536-abe2-c23e01d0b526/datasheet-silyzer300.pdf

[65] Sunfire-Synlink SOEC factsheet. https://www.sunfire.de/files/sunfire/images/content/Sunfire.de%20(neu)/Sunfire-Factsheet-SynLink-SOEC-20210303.pdf.

[66] Nathan P. Siegel, James E. Miller, Ivan Ermanoski, Richard B. Diver, and Ellen B. Stechel, *Factors Affecting the Efficiency of Solar Driven Metal Oxide Thermochemical Cycles*, Industrial & Engineering Chemistry Research 2013 52 (9), 3276-3286 DOI: 10.1021/ie400193q

[67] Robert Pitz-Paal, Nicolas Bayer Botero, Aldo Steinfeld, *Heliostat field layout optimization for high-temperature solar thermochemical processing*, Solar Energy, Volume 85, Issue 2, 2011, Pages 334-343, ISSN 0038-092X, https://doi.org/10.1016/j.solener.2010.11.018. (https://www.sciencedirect.com/science/article/pii/S0038092X10003580)

[68] Saeb M. Besarati, D. Yogi Goswami, *A computationally efficient method for the design of the heliostat field for solar power tower plant*, Renewable Energy, Volume 69, 2014, Pages 226-232, ISSN 0960-1481, https://doi.org/10.1016/j.renene.2014.03.043. (https://www.sciencedirect.com/science/article/pii/S0960148114002079)